The Pennsylvania State University
The J. Jeffrey and Ann Marie Fox Graduate School

FAST IMPLEMENTATION OF NONLINEAR PERTURBATION THEORY STATISTICS INCLUDING GALAXY BIAS AND REDSHIFT-SPACE DISTORTION

A Dissertation in
Astronomy and Astrophysics
by
Joseph Tomlinson

© 2024 Joseph Tomlinson

Submitted in Partial Fulfillment
of the Requirements
for the Degree of

Doctor of Philosophy

December 2024

The dissertation of Joseph Tomlinson was reviewed and approved by the following:

Donghui Jeong
Professor of Astronomy & Astrophysics
Dissertation Advisor
Chair of Committee

Michael Eracleous
Professor of Astronomy & Astrophysics

Kohta Murase
Professor of Physics and Astronomy & Astrophysics

Sarah Shandera
Professor of Physics

Randy McEntaffer
Professor of Physics and Astronomy & Astrophysics
Professor in Charge

Abstract

One of the most powerful probes of cosmology in the current era are galaxy redshift surveys. While less precise than Cosmic Microwave Background (CMB) measurements, these surveys allow us to probe redshifts that are not simply accessible from the CMB. Fully grasping the data from these surveys is essential to gaining a deeper understanding of the Hubble tension, the evolution of dark energy, and other cosmological unknowns.

Unlike the CMB, galaxies are formed at much later times, when the underlying matter density field is significantly nonlinear. These nonlinear features are both expensive to calculate and how much extra domain is gained is heavily dependent on redshift. We will first summarize the current state of Next-to-leading Order (NLO) power spectrum models and then describe how to extend these methods to the NLO bispectrum (a higher-order statistic compared to the power spectrum.)

In addition to traditional nonlinear effects, the standard cosmological models only deal with modelling the underlying matter density field which is subtly different from what is actually observed in galaxy surveys, the galaxy density field. This difference between the galaxy and matter density, named galaxy bias, must be taken into account for more accurate modelling of past and future galaxy surveys. We will summarize a general method for determining all relevant biasing factors at a given order in perturbation theory and then develop how to apply these biasing factors to the fast model for the NLO power spectrum.

Table of Contents

List of Figures

List of Tables

Acknowledgments

I would like to thank my advisor, Donghui Jeong, without whom I would never have been able to make it this far. His guidance has been invaluable to developing the most difficult parts of this dissertation and he is truly someone I look up to. I am also indebted to my colleague Zhenyuan Wang who I have had countless productive conversations with. He has given much assistance and inspiration throughout the course of this work. I am grateful to Dave Goldberg, Steve McMillan, and Michael Vogeley for teaching me how to be a scientist and for encouraging me to follow this path.

This material is based upon work supported by NSF grant AST-1517363, NASA ATP program 80NSSC18K1103, and NASA FINESST 80NSSC22K1751. The findings and conclusions do not necessarily reflect the view of the funding agency.

Chapter 1
Introduction

Large-scale structure is one of the biggest areas of precision cosmology taking up the mantle from the CMB. One of the most power probes within Large-scale structure are galaxy surveys, where we observe the positions of galaxies in our sky. Though this tool is not as precise as the CMB it allows for a much wider exploration along the time domain, vital for constraining the evolution of parameters.

Upcoming large-scale structure (LSS) surveys [7–14] will allow us to probe the clustering of galaxies on ever larger scales while measuring them on existing scales with high precision. This increase in precision on small-scale galaxy clustering measurements calls for more accurate models that have well characterized systematics. There has been significant development of the theoretical models in recent years, from fast methods for computing next-to-leading and higher-order corrections [15–19], to developments of the galaxy bias models to bridge theory and observations [20–25].

Traditional LSS analysis focuses on the baryon acoustic oscillations (BAO) feature (e.g. [26; 27]), but the constraints on cosmological parameters can be improved with a full shape (FS) analysis which is sensitive to all cosmological parameters [28–30]. This allows for galaxy clustering analysis to measure more than just geometrical quantities such as angular diameter distance and the Hubble expansion rate from BAO, but also probe the linear growth rate through redshift-space distortions (RSD) [31], the shape of the primordial power spectrum [32], primordial non-Gaussianity [33], the equation of state of dark energy [34], and neutrino mass [35].

To unlock the full potential of the galaxy power spectrum, that is, to use the FS analysis, accurate modeling of the nonlinearities in the galaxy power spectrum is essential. For the high redshift Universe which these surveys are targeting, there are ample quasi-linear regimes in which nonlinear perturbation theory (PT, see [36] for a review) accurately models the matter clustering beyond the linear theory [37; 38]. We can, therefore, extend

the cosmological analysis using the power spectrum on these quasi-linear scales, and hence improve the cosmological constraints from the surveys. The recent studies [30; 32; 39] have successfully applied the PT-based analysis for the BOSS DR12 data, and it will only be more powerful with high-redshift galaxy surveys.

The exact scale at which NLO perturbation theory is required is extremely important not only for accurately estimating the information gained by including NLO corrections, but also for properly keeping theoretical systematics under control. This has been studied to some extent for the power spectrum [2; 40–42] and bispectrum [43–46], but extensive measurements for a variety of redshifts are required, since the range of validity is sensitive to the redshift. This is especially true for the bispectrum. With accurate knowledge of the difference between the applicable scales of the LO and NLO models, along with knowledge of covariance matrices (e.g. [47]) to measure mode coupling at small scales which erases some of the information gained from the extra modes at those scales, one could then accurately predict the constraining power gained from using a NLO model over a LO model.

Modeling the observed galaxy power spectrum must include two more nonlinearities besides the evolution of the matter density on quasi-linear scales: nonlinear galaxy bias and nonlinear redshift-space distortion. First, what we observe in galaxy surveys is some sampling of the galaxy distribution, which is a biased tracer of the underlying matter density field [48–50]. Thanks to the complex gastrophysical nature of the formation and evolution of galaxies, predicting the galaxy distribution from first principles is beyond our reach at present. Instead, on quasi-linear scales, we have created an effective description of galaxy statistics by means of the perturbative bias expansion that includes all possible physical quantities that the galaxy distribution can depend upon. A recent review [3] has presented a complete description of bias by including *all* observables that a local observer in the galaxy can measure, at any given order in PT.

In galaxy redshift surveys we infer the distance to the galaxies by their observed spectral shift, assuming that it is solely due to the Hubble flow. The term "redshift space" refers to the galaxies position measured in this way. The issue is that peculiar velocities also contribute to the spectral shift and distort the galaxy distribution in redshift space. Because the peculiar velocity is strongly correlated with density field, this effect leads to a systematic change in clustering statistics, so called redshift-space distortions (RSD). Ref. [51] has established the linear RSD model, and Refs. [52–54], for example, have presented a perturbative description of modeling nonlinear RSD effect.

In addition to the nonlinear galaxy bias and nonlinear RSD, the line-of-sight directional

selection effects can further distort the observed galaxy power spectrum. As the name suggests, the selection effect arises because the way that we select the sample of galaxies [55; 56]. For example, because of the intrinsic alignment [57–63], galaxies orientation with respect to the line-of-sight direction can be correlated to the large-scale tidal field. If the survey preferentially selects a particular orientation (face-on or edge-on) of galaxies, then the observed galaxy power spectrum can also depend on the line-of-sight directional projection of the large-scale tidal field [56]. Another example is for the emission-line selected galaxy samples, where the radiative transfer effects generate a strong-dependence on the line-of-sight directional velocity flow [55]. The bias review [3] has also described a general bias expansion that can be used to take all of the above effects into account at any given order in perturbation theory, resulting in a description of the next-to-leading order (NLO) or 1-loop power spectrum and the leading order (LO) or tree-level bispectrum in a complete bias expansion in Ref. [4].

The typical expressions for the observed galaxy power spectrum in NLO involves the integrals over the three-dimensional Fourier space, so called one-loop contribution. The naive implementation of these multi-dimensional integrals, however, does not meet the requirements for the data analysis. For example, for the cosmological analysis, the computation of NLO terms needs to be paired with Markov-Chain-Monte-Carlo (MCMC) analysis pipeline that calls the NLO calculation for each set of cosmological parameters. To get robust constraints on cosmological parameters, we typically need parameter chains as long as a few million realizations; that means we need to compute the NLO power spectra millions of times.

This requirement for the data analysis has motivated the development of fast calculation algorithms. For example, the FAST-PT methods developed by Ref. [64] and Ref. [65] pre-calculates the angular parts of the loop integrals analytically, leaving the radial parts in terms of spherical Bessel transformations (SBTs). The SBTs can be computed efficiently by using what is commonly known as FFTLog based methods [66–69]. This analysis was extended to higher-order (two-loop) corrections to the matter power spectrum in Ref. [70] and Ref. [71], and to more complicated integration kernels in Ref. [72]. Ref. [30] used a similar technique but for a biased tracer model similar to the one in this work but without the selection effects. Ref. [73] took a different approach by parametrizing the power spectrum as a sum of power laws and factoring out the cosmological dependence so all integrals could be done only once for all sets of parameters.

While most of this work has been done on the power spectrum, this increase in

precision will also allow for higher-order statistics to be used, typically the three-point function or it's Fourier transform the bispectrum. Some significant progress has been made in modelling the bispectrum in a similar way to the power spectrum [25; 43; 74–80]. Using the bispectrum is important for properly breaking degeneracies that are present in the power spectrum. The use of the bispectrum has been shown to increase constraints on various cosmological parameters of importance, dark energy [81–83], primordial non-Gaussianity [84–87], and neutrino mass [88–91].

One challenge in studying the bispectrum, and similarly other higher-order polyspectrum, in Fourier space is to find an efficient estimator; when estimating the n-th order polyspectrum, the complexity of the naive estimator grows as the number of all possible n-gons in the three-dimensional Fourier space that scales as $N_{\rm max}^{3(n-1)}$. Here, $N_{\rm max} \equiv k_{\rm max}/\delta k$ is the number of one-dimensional discrete grid points of interest, with $k_{\rm max}$ being the maximum wavenumber of the analysis, usually set by the smallest scale that we can reliably model the nonlinearities in galaxy density field, and δk being the size of the binning in Fourier space.

One can alleviate this computational cost by using the Fourier space representation of the Dirac-delta operator that dictates the statistical homogeneity. Originally done by Ref. [92] for estimating the bispectrum, in this way, we can estimate a polyspectrum by taking advantage of the Fast Fourier transformation algorithm. As we shall outline in Sec. 6, the calculation of the polyspectrum then boils down to a sum of products of the $N_{\rm max}$ distinct three-dimensional Fourier volumes derived from the original density field. This method avoids directly sampling all n-gons and is computationally much faster for all high-order polyspectra, with the only downside being loss of angular information for polyspectra higher order than the bispectrum.

The implementation of the Fourier based method, however, requires allocating a large amount of memory. To avoid the aliasing problem associated with the Fourier method, the three-dimensional Fourier grid must be at least $(sN_{\rm max})^3$ for the s-point polyspectrum; as we need a total of $N_{\rm max}$ such three-dimensional Fourier volumes, the memory requirement grows as $s^3 N_{\rm max}^4$. For example, the memory requirement to estimate the bispectrum ($s = 3$) with $N_{\rm max} = 128$, when using single precision, is already 27 Gigabytes.

The outline of this dissertation is as follows. In Chapter 2 we review the fundamentals of Eulerian Perturbation Theory (SPT) as it relates to this dissertation. We then review both the general bias expansion and the FFTLog transformation, including a new extension to 2D, used extensively in this work.

In Chapter 3 we present our unique visualization method for the bispectrum, the spherical bispectrum. The need for this arises due to the bispectrum being a function of three different wavenumbers and becomes cumbersome to plot. We alleviate this by transforming the basis of the bispectrum to concentrate absolute scale information into a single variable. We then utilize this new visualization technique to examine a few important parts of how our SPT models compare with real data/simulations, including the estimator binning effect. Finally we discuss the range of validity of both LO and NLO power spectrum and bispectrum models.

In Chapter 4 we combine the general bias expansion with FFTLog type methods to derive a fast expression for the galaxy NLO power spectrum with RSD and selection effects. This allows us to fully model the NLO galaxy power spectrum in under one second, fast enough to be used for full shape MCMC analysis. We then test our code in a few known ways, then look for both formal and effective degeneracies in our bias parameters.

Chapter 5 is a technical chapter in which we present a framework for transforming the integrals for the NLO matter bispectrum into a form that is amenable to our 2D FFTLog formalism. The implementation of this framework is left for future work.

Finally in Chapter 6 we present an optimized parallel estimator for the bispectrum and other higher-order polyspectra. We begin by reviewing the existing optimized bispectrum estimator then go over how to extend it to higher-order polyspectra. Next we discuss how to optimally parallelize this estimator, then we perform some tests of our code including some basic benchmarks.

Throughout the work we use the following conventions and shorthand notations

$$f(x) \equiv \int \frac{d^3\boldsymbol{k}}{(2\pi)^3} f(k) e^{i\boldsymbol{k}\cdot\boldsymbol{x}} \equiv \int_{\boldsymbol{k}} f(k) e^{i\boldsymbol{k}\cdot\boldsymbol{x}}\,, \tag{1.1}$$

$$\int_r f(r) \equiv \int \frac{\mathrm{d}r}{2\pi^2} r^2 f(r) \tag{1.2}$$

$$\int_{\hat{\boldsymbol{r}}} f(r) \equiv \int \frac{\mathrm{d}\Omega_r}{4\pi} f(r) \tag{1.3}$$

$$\mu_{k,q} \equiv \hat{\boldsymbol{k}}\cdot\hat{\boldsymbol{q}}\,, \tag{1.4}$$

$$\langle \delta(\boldsymbol{k}_1)\delta(\boldsymbol{k}_2)\delta(\boldsymbol{k}_3)\rangle = (2\pi)^3 B(\boldsymbol{k}_1,\boldsymbol{k}_2,\boldsymbol{k}_3)\delta^D(\boldsymbol{k}_{123})\,. \tag{1.5}$$

$$\xi_n^l(r) = \int_q q^n j_l(qr) P_L(q) \tag{1.6}$$

$$\Xi^n_{l_1 l_2}(r,s) = \int_q q^n j_{l_1}(qr) j_{l_2}(qs) P_L(q) \tag{1.7}$$

$$\mathcal{P}^{l_1,l_2}_{n_1,n_2}(k) = \int_r r^{n_2} j_{l_2}(kr) \xi^{l_1}_{n_1}(r) \tag{1.8}$$

Here, δ^D is the Dirac-delta operator, and we use the shorthanded notation of $\boldsymbol{k}_{1\cdots n} \equiv \boldsymbol{k}_1 + \cdots \boldsymbol{k}_n$. We denote the amplitude of a vector $\boldsymbol{k}_i$ as k_i. Throughout this work we use the terms 1-loop and NLO interchangeably.

Chapter 2
Methods

2.1 Eulerian Perturbation Theory

As for the theory model, we use the standard Eulerian perturbation theory(SPT) model, see [93] for a review. In brief, SPT factors the full nonlinear matter density into different parts

$$\delta(\boldsymbol{k}) = \delta_L(\boldsymbol{k}) + \delta^{(2)}(\boldsymbol{k}) + \delta^{(3)}(\boldsymbol{k}) + \cdots \,, \tag{2.1}$$

where $\delta^{(n)}(\boldsymbol{k})$ stands for the n-th order density contrast proportional to the n linear quantities such as density field, velocity field, and tidal field. We can then use Wick's theorem to find the leading order (LO) and the next-to-leading order (NLO) contribution to the power spectrum straightforwardly

$$\langle \delta(\boldsymbol{k})\delta(\boldsymbol{k}')\rangle = \langle \delta_L(\boldsymbol{k})\delta_L(\boldsymbol{k}')\rangle + 2\left\langle \delta_L(\boldsymbol{k})\delta^{(3)}(\boldsymbol{k}')\right\rangle + \left\langle \delta^{(2)}(\boldsymbol{k})\delta^{(2)}(\boldsymbol{k}')\right\rangle \tag{2.2}$$

We write each term in the above equation as

$$P_{\rm LO+NLO}(k) = P_L(k) + 2P_{13}(k) + P_{22}(k)\,, \tag{2.3}$$

where the leading order power spectrum is simply the linear power spectrum $P_{\rm LO}(k) = P_L(k)$, and the NLO terms consist of

$$\begin{aligned} P_{22}(k) &= 2\int \frac{\mathrm{d}^3\boldsymbol{q}}{(2\pi)^3} F_2(\boldsymbol{q}, \boldsymbol{k}-\boldsymbol{q})^2 P_L(q) P_L(|\boldsymbol{k}-\boldsymbol{q}|) \\ P_{13}(k) &= 3P_L(k)\int \frac{\mathrm{d}^3\boldsymbol{q}}{(2\pi)^3} F_3(\boldsymbol{q}, -\boldsymbol{q}, \boldsymbol{k}) P_L(q)\,. \end{aligned} \tag{2.4}$$

Here, $F_n(\boldsymbol{q}_1, \cdots, \boldsymbol{q}_n)$ is the n-th order integration kernel, see [93]. For the form suitable for a faster implementation of these integrals using the FFTlog-based method, see [15; 16].

Since the initial density field is close to Gaussian [94; 95], we assume that the linear-order density field follows Gaussian statistics, and there is no linear expression for the bispectrum. The leading-order bispectrum expression is

$$B_{\rm LO}(k_1, k_2, k_3) = B_{211}(k_1, k_2, k_3) = 2F_2(\boldsymbol{k}_1, \boldsymbol{k}_2)P_L(k_1)P_L(k_2) + (2 \text{ cyclic}) \,. \tag{2.5}$$

Like the NLO power spectrum calculation, we can use Wick's theorem to find the NLO contribution to the bispectrum

$$\begin{aligned} B_{\rm LO+NLO}(k_1, k_2, k_3) &= B_{\rm LO}(k_1, k_2, k_3) + B_{222}(k_1, k_2, k_3) \\ &+ B_{411}(k_1, k_2, k_3) + B^I_{123}(k_1, k_2, k_3) + B^{II}_{123}(k_1, k_2, k_3) \,, \end{aligned} \tag{2.6}$$

where

$$\begin{aligned} B_{222}(k_1, k_2, k_3) = \; & 8 \int \frac{\mathrm{d}^3\boldsymbol{q}}{(2\pi)^3} F_2(\boldsymbol{q}, \boldsymbol{k}_1 - \boldsymbol{q}) F_2(-\boldsymbol{q}, \boldsymbol{k}_2 + \boldsymbol{q}) F_2(\boldsymbol{q} - \boldsymbol{k}_1, -\boldsymbol{k}_2 - \boldsymbol{q}) \\ & \times P_L(q) P_L(|\boldsymbol{k}_1 - \boldsymbol{q}|) P_L(|\boldsymbol{k}_2 + \boldsymbol{q}|) \,, \end{aligned} \tag{2.7}$$

$$B_{411}(k_1, k_2, k_3) = 12 P_L(k_1) P_L(k_2) \int \frac{\mathrm{d}^3\boldsymbol{q}}{(2\pi)^3} F_4(\boldsymbol{q}, -\boldsymbol{q}, -\boldsymbol{k}_1, -\boldsymbol{k}_2) P_L(q) + (2 \,\text{cyclic}) \,, \tag{2.8}$$

$$\begin{aligned} B^I_{123}(k_1, k_2, k_3) = \; & 6 P_L(k_1) \int \frac{\mathrm{d}^3\boldsymbol{q}}{(2\pi)^3} F_2(\boldsymbol{q}, \boldsymbol{k}_2 - \boldsymbol{q}) F_3(-\boldsymbol{q}, \boldsymbol{q} - \boldsymbol{k}_2, -\boldsymbol{k}_1) \\ & \times P_L(q) P_L(|\boldsymbol{k}_2 - \boldsymbol{q}|) + (5 \,\text{cyclic}) \,, \end{aligned} \tag{2.9}$$

$$B^{II}_{123}(k_1, k_2, k_3) = 6 P_L(k_1) P_L(k_2) F_2(\boldsymbol{k}_1, \boldsymbol{k}_2) \int \frac{\mathrm{d}^3\boldsymbol{q}}{(2\pi)^3} F_3(\boldsymbol{q}, -\boldsymbol{q}, \boldsymbol{k}_2) P_L(q) + (5 \,\text{cyclic}) \,. \tag{2.10}$$

A fast way to compute these integrals is discussed in Chapter 5

These perturbation theory expressions are what we use throughout this work. For the linear power spectrum we take the one provided with the Quijote simulations generated using CAMB [96]. To calculate the NLO power spectrum model we use an adaptation of the methods described in [15]. The LO bispectrum model is generated using the provided linear power spectrum and Eq. (2.5). We generate our NLO bispectrum model through direct integration.

2.2 General Bias Expansion

Beyond just modelling the matter clustering statistics as discussed in the previous section, we also extend our modelling to account for differences between the matter and observed galaxy distribution. We do this through using a first principles bias model that operates order-by-order in perturbation theory, known as the General Bias Expansion, or sometimes the perturbative bias expansion [3].

The expression for the 1-loop galaxy power spectrum in redshift space requires the perturbative bias expansion [3] up to third order. Here, we summarize the third-order expression for the observed (redshift-space) galaxy density contrast as derived in [4], including the line-of-sight directional selection effects caused by radiative-transfer effects [55] or tidal alignment [56].

Throughout, we work in comoving coordinates $\boldsymbol{x}$ and the conformal time variable τ. We denote the matter density contrast $\delta(\boldsymbol{x},\tau)$, galaxy density contrast (in real space) $\delta_g(\boldsymbol{x},\tau)$, and matter velocity $\boldsymbol{v}(\boldsymbol{x},\tau)$. We also define the scaled matter velocity $\boldsymbol{u}(\boldsymbol{x},\tau) = \frac{1}{\mathcal{H}(\tau)}\boldsymbol{v}(\boldsymbol{x},\tau)$, where $\mathcal{H} = aH$ is the Hubble expansion rate. We denote the unit vector along the line-of-sight direction as $\hat{\boldsymbol{n}}$, and the line-of-sight directional derivative $\partial_\parallel \equiv \hat{\boldsymbol{n}}^i\partial_i$. This gives the parallel derivative of the scaled line-of-sight velocity $\eta(\boldsymbol{x},\tau) = \partial_\parallel u_\parallel(\boldsymbol{x},\tau)$. We denote the matter power spectrum $P^{\delta\delta}(k,\tau)$ while we denote the galaxy power spectrum as $P^{gg}(k,\tau)$ in real space and $P^{gg,s}(k,\mu,\tau)$ in redshift space with the line-of-sight directional cosine $\mu = \hat{\boldsymbol{k}}\cdot\hat{\boldsymbol{n}}$.

The key for the general perturbative bias expansion [3] is to expand the galaxy density contrast $\delta_g(\boldsymbol{x},\tau)$ in the following form

$$\delta_g(\boldsymbol{x},\tau) = \sum_{\mathcal{O}}[b_{\mathcal{O}}(\tau) + \epsilon_{\mathcal{O}}(\boldsymbol{x},\tau)]\mathcal{O}(\boldsymbol{x},\tau) + \epsilon(\boldsymbol{x},\tau), \tag{2.11}$$

where $\mathcal{O}$ stands for any operator that contributes to the formation and evolution of the galaxies, $b_{\mathcal{O}}$ is the bias parameter associated with that operator. Both $\epsilon_{\mathcal{O}}$ and ϵ stand for stochastic parameters encoding the stochastic processes on *sub-grid* scales that are uncorrelated with the operators $\mathcal{O}(\boldsymbol{x},\tau)$ defined on the large scales where PT is valid. Note that, although only operators at equal time explicitly appear in Eq. (2.11), the expression also includes the effects of all operators along the galaxies' world line, that is, operators at all past times. This is because we can trace the time evolution of operators at each order on large scales where the PT-based models operate.

The central idea behind the perturbative bias expansion in Eq. (2.11) is to include all

local observables. Following Ref. [3], we construct the local gravitational observables in PT starting from the quantity combining the matter density contrast δ and the tidal field K_{ij} as

$$\Pi^{[1]}_{ij} = K_{ij} + \frac{1}{3}\delta_{ij}\delta = \partial_i\partial_j\Phi\,, \tag{2.12}$$

where Φ is proportional to the gravitational potential ϕ: $\phi(\boldsymbol{x},\tau) = 4\pi G a^2(\tau)\bar{\rho}_m(\tau)\Phi(\boldsymbol{x},\tau)$. The superscript [1] here means that the leading order term in $\Pi^{[1]}$ is linear order in PT. Ref. [3] have demonstrated that one can define the higher-order quantities

$$\Pi^{[n]}_{ij} = \frac{1}{(n-1)!}\left[(\mathcal{H}f)^{-1}\frac{D}{D\tau}\Pi^{[n-1]}_{ij} - (n-1)\Pi^{[n-1]}_{ij}\right]\,, \tag{2.13}$$

which, as n-th order convective derivatives of $\Pi^{[1]}_{ij} = \partial_i\partial_j\Phi$, capture all local gravitational observables at higher orders. Here, $D/D\tau = \partial_\tau + v^i\partial_{x,i}$ is the convective derivative following the peculiar velocity field. The n-th order rank-2 tensors $\Pi^{[n]}_{ij}$, therefore, form our building blocks for the perturbative bias expansion. Taking every combination up to 3rd order, we find the following set of operators

$$\left\{\delta,\ \delta^2,\ \delta^3,\ \mathrm{tr}[KK] = K^2,\ \delta K^2,\ K^3, O_{\mathrm{td}}\right\}\,, \tag{2.14}$$

suffices the description of galaxy clustering to third order, or NLO in galaxy power spectrum. Here,

$$O_{\mathrm{td}} = \frac{8}{21}K_{ij}\left(\frac{\partial_i\partial_j}{\nabla^2} - \frac{1}{3}\delta_{ij}\right)\left(\delta^2 - \frac{3}{2}K^2\right)\,, \tag{2.15}$$

that appears in third order is the lowest order non-trivial quantity, which cannot be formed by algebraic combination of δ and K_{ij}, of galaxy bias expansion. It is, however, clearly a local observable, as O_{td} is proportional to the convective derivative of the tidal field.

In addition to the deterministic bias expansion above, we also include the stochastic contribution to the galaxy power spectrum given as

$$P_\epsilon(k) = P^{\{0\}}_\epsilon + k^2 P^{\{2\}}_\epsilon + \mathcal{O}(k^4), \tag{2.16}$$

where the superscript $\{\}$ denotes the order, or power of k, of the stochastic terms, and the higher derivative bias terms that incorporate the feedback from the small-scale dynamics, which is simply $b_{\nabla^2\delta}\nabla^2\delta$ at third order.

Transferring to redshift space, we need to model the peculiar velocity field of galaxies.

In linear order, the peculiar velocity field $\boldsymbol{v}_g$ of galaxies coincides with the cosmic matter flow velocity, $\boldsymbol{v}$, but $\boldsymbol{v}_g$ in general can be different from $\boldsymbol{v}$ because of the dynamical friction or non-gravitational momentum exchange due to feedback, for example. We include these effect as the velocity bias, deviation of galaxy velocity field from the matter velocity field, with additional higher derivative bias parameters $\beta_{\nabla^2\boldsymbol{v}}$ and $\beta_{\partial_\parallel^2\boldsymbol{v}}$, as

$$\boldsymbol{v}_g = \boldsymbol{v} + \beta_{\nabla^2\boldsymbol{v}}\nabla^2\boldsymbol{v} + \beta_{\partial_\parallel^2\boldsymbol{v}}\partial_\parallel^2\boldsymbol{v} + \varepsilon_v\,. \tag{2.17}$$

In this notation, we write the line-of-sight directional velocity divergence as

$$\eta_g = \left(1 - \beta_{\nabla^2\boldsymbol{v}}k^2 - \beta_{\partial_\parallel^2\boldsymbol{v}}k^2\mu^2\right)\eta + \varepsilon_\eta, \tag{2.18}$$

where $\mu = \hat{\boldsymbol{k}}\cdot\hat{\boldsymbol{n}}$. The coordinate transformation between the real space and the redshift space is

$$\boldsymbol{x}_s = \boldsymbol{x} + u_\parallel\hat{\boldsymbol{n}}\,, \tag{2.19}$$

and the number of galaxies stays invariant under the coordinate transformation:

$$(1+\delta_{g,s}(\boldsymbol{x}_s))\,d^3x_s = (1+\delta_g(\boldsymbol{x}))\,d^3x\,. \tag{2.20}$$

Here, we neglect the terms proportional to $1/r$ in favor of $\partial_\parallel$ whose contribution dominates on the quasi-linear scales where NLO terms are important. By expressing Eq. (2.20) at the redshift-space coordinates, we find the expression for the galaxy density contrast to third order

$$\delta_{g,s} = \delta_g^{\rm Jac} + \delta_g^{\rm disp} \tag{2.21}$$

$$\delta_g^{\rm Jac} = (1+\delta_g)(1-\eta_g+\eta_g^2) - \eta_g^3 - 1 \tag{2.22}$$

$$\delta_g^{\rm disp} = -u_{g\parallel}\partial_\parallel\delta_g^{\rm Jac} + \frac{1}{2}u_{g\parallel}^2\partial_\parallel^2\delta_g^{\rm Jac} + (u_{g\parallel}\partial_\parallel u_{g\parallel})\partial_\parallel\delta_g^{\rm Jac}\,. \tag{2.23}$$

Note that the $\delta_g^{\rm Jac}$ terms corresponds to the Jacobian $(\partial\boldsymbol{x}/\partial\boldsymbol{x}_s)$ of the coordinate mapping to redshift-space, and the $\delta_g^{\rm disp}$ terms corresponds to the displacement of the fields from the real space coordinate $\boldsymbol{x}$ to the observed redshift coordinate $\boldsymbol{x}_s$.

In order to include the line-of-sight dependent selection effects, which treat the line of sight $\hat{\boldsymbol{n}}$ as a preferred direction, we need to employ additional bias terms constructed by combining the local gravitational observables $\Pi_{ij}^{[n]}$ with the line-of-sight directional unit vector $\hat{\boldsymbol{n}}$, allowing for combinations such as $\Pi_\parallel = \Pi_{ij}\hat{\boldsymbol{n}}^i\hat{\boldsymbol{n}}^j$. To third order in PT,

the additional terms are:

$$\left\{\eta,\ \delta\eta,\ (KK)_{\parallel},\ \eta^2,\ \Pi^{[2]}_{\parallel},\ \delta\Pi^{[2]}_{\parallel},\ (K\Pi^{[2]})_{\parallel},\ \eta\Pi^{[2]}_{\parallel},\ \Pi^{[3]}_{\parallel},\ \partial^2_{\parallel}\delta,\ \nabla^2\eta,\ \partial^2_{\parallel}\eta\right\}\,. \tag{2.24}$$

Note that we count the last three higher-derivative terms as third order as they are suppressed by a factor of $(k/k_\star)^2$ compared to the respective linear order quantities [3]. Here, $k_\star \simeq 1/R_\star$ is the wavenumber corresponding to the relevant length scale $R_\star$ where the high-derivative effect, or non-locality, starts to be important. Assuming that the Lagrangian radius of typical halos $R_\star \sim 1$ Mpc$/h$ sets the relevant non-locality scale, we count each power of $k/k_\star$ as an extra order in perturbation theory.

2.3 FFT-Log Transformation

The FFTLog-based integration accelerates the computation speed of the spherical Bessel transformations, SBTs, sometimes known as Hankel transformations. For the implementation of the one-loop power spectrum expression, we only need the SBTs involving a single Bessel function:

$$\xi^{\ell}_{n}(r) = \int_0^\infty \frac{k^2\mathrm{d}k}{2\pi^2} k^n j_\ell(kr) P_L(k). \tag{2.25}$$

Due to the oscillatory nature of the integrand, mainly caused by the spherical Bessel functions, these integrals are often slow to compute with ordinary quadrature methods.

The key observation [66–69] for the fast integration of Eq. (2.25) is to perform the integration in the logarithmic space. That is, defining

$$k = k_0 e^{\kappa} \qquad r = r_0 e^{\rho}\,, \tag{2.26}$$

reduces Eq. (2.25) to a convolution integral in κ and ρ:

$$\xi^{\ell}_{n}(r) = \frac{k_0^3 e^{-\rho q}(k_0 r_0)^n}{2\pi^2} \int_{-\infty}^{\infty} \mathrm{d}\kappa\, e^{\kappa(3-q+n)} P_L(k_0 e^{\kappa}) e^{q(\kappa+\rho)} j_\ell(k_0 r_0 e^{\kappa+\rho})\,, \tag{2.27}$$

which can be instead performed as a multiplication in the Fourier-dual space of κ. Here, we introduce a power law factor, $(kr)^q$, to enhance the performance of the numerical implementation, more specifically, to reduce the aliasing effect. This is known as the FFTLog biasing parameter, q, distinct from the bias expansion discussed in this work. This factor, which formally leaves the result unchanged, allows for the input function, $P_L(k)$ in this case, to be "biased" by k^{-q} to behave better numerically, while absorbing the

opposing factor k^q into the spherical Bessel function. Of course, the readers should not confuse this biasing factor with the galaxy bias. Explicitly, we define the one-dimensional Fourier transform of the biased power spectrum and the biased spherical Bessel function, respectively, as

$$\phi^q(t) = \int_{-\infty}^{\infty} \frac{\mathrm{d}\kappa}{2\pi} e^{i\kappa t} e^{\kappa(3-q)} P(k_0 e^{\kappa}) \,, \tag{2.28}$$

$$e^{q(\kappa+\rho)} j_\ell(k_0 r_0 e^{\kappa+\rho}) = \int_{-\infty}^{\infty} \frac{\mathrm{d}t}{2\pi} e^{i(\kappa+\rho)t} M_\ell^q(t) \,, \tag{2.29}$$

where inverting Eq. (2.29) serves as the definition of M_ℓ^q. We use Eqs. (2.28)–(2.29) to re-write Eq. (2.25) as the integration in the dual (t) space as

$$\xi_n^\ell(r) = \frac{k_0^3 e^{-\rho q} (k_0 r_0)^n}{2\pi^2} \int_{-\infty}^{\infty} \frac{\mathrm{d}t}{2\pi} e^{i\rho t} \phi^{q-n}(t) M_\ell^q(t) \,. \tag{2.30}$$

The Fourier transform of the biased spherical Bessel function, $M_\ell^q(t)$, can be defined analytically in terms of Gamma functions [69]:

$$M_\ell^q(t) = 2^{n-1} \sqrt{\pi} (k_0 r_0)^{it-q} \frac{\Gamma[\frac{1}{2}(\ell + q - it)]}{\Gamma[\frac{1}{2}(3 + \ell - q + it)]} \,. \tag{2.31}$$

So calculating $\xi_n^\ell(r)$ amounts to just another Fourier transform of $\phi^{q-n}(t) M_\ell^q(t)$ using FFT.

In order to implement the FFTlog-based method, we need to set three parameters: k_0, r_0 and q. Following the discussion in [68], we set k_0 and r_0 so that $k_0 r_0 \approx 1$. The choice of the biasing parameter q is more subtle. While Ref. [69] have systematically studied the choice of the biasing parameter, their prescription of *choosing a q value to make the slopes at the end of the input equal* is well suited for our case, but only when zero padding on both ends of the input to each FFT by a factor ≥ 2, as suggested in [16]. Besides the zero padding, all of our 1D-FFTLog computations use the implementation of [69].

2.3.1 Extension to 2D

Later in this work when considering the NLO Bispectrum we will need to deal with 2D-SBTs not covered by either case in [69]. To compute these integrals efficiently we will

need to extend the FFTLog transformation to the general 2D case.

To extend the FFTLog transformation to multiple dimensions is straightforward. Considering the generic integral

$$\xi_{\ell_1,\ell_2}(r,g) = \int_0^\infty \frac{\mathrm{d}k_1}{2\pi^2} \int_0^\infty \frac{\mathrm{d}k_2}{2\pi^2} k_1^2 k_2^2 P(k_1,k_2) j_{\ell_1}(k_1 r) j_{\ell_2}(k_2 g) \tag{2.32}$$

This integral has identical properties as the previously considered 1D case. We use the power law biased input function

$$\left(\frac{k_1}{k_{1,0}}\right)^{3-q_1} \left(\frac{k_2}{k_{2,0}}\right)^{3-q_2} P(k_1,k_2) = e^{(3-q_1)\kappa_1} e^{(3-q_2)\kappa_2} P(k_{1,0}e^{\kappa_1}, k_{2,0}e^{\kappa_2}) \tag{2.33}$$

Then in exact analogy we define the 2D fourier transform of the biased input function

$$\phi^{q_1,q_2}(x_1,x_2) = \int \frac{\mathrm{d}\kappa_1}{2\pi} e^{i\kappa_1 x_1} \int \frac{\mathrm{d}\kappa_2}{2\pi} e^{i\kappa_2 x_2} \left(e^{(3-q_1)\kappa_1} e^{(3-q_2)\kappa_2} P(k_{1,0}e^{\kappa_1}, k_{2,0}e^{\kappa_2})\right) \tag{2.34}$$

We can then transform the original integral into the form

$$\begin{aligned}\xi_{\ell_1,\ell_2}(r,g) = \frac{k_{1,0}^3 k_{2,0}^3 e^{-q_1\rho_1} e^{-q_2\rho_2}}{(2\pi^2)^2} \int_{-\infty}^\infty \mathrm{d}\kappa_1 \int_{-\infty}^\infty \mathrm{d}\kappa_2 \left(e^{(3-q_1)\kappa_1} e^{(3-q_2)\kappa_2} P(k_{1,0}e^{\kappa_1}, k_{2,0}e^{\kappa_2})\right) \\ \times \left(e^{q_1(\kappa_1+\rho_1)} j_{\ell_1}(k_{1,0} r_{1,0} e^{\kappa_1+\rho_1})\right) \left(e^{q_2(\kappa_2+\rho_2)} j_{\ell_2}(k_{2,0} r_{2,0} e^{\kappa_2+\rho_2})\right)\end{aligned} \tag{2.35}$$

which like the 1D case is simply a 2D convolution integral. We can therefore write this as the 2D fourier transform of the multiplication of the terms in parenthesis (this is not generally true but since the last two terms are independent of each other the 2D fourier transform of their product is just the outer product of their 1D fourier transforms, so this statement holds in this case) given by

$$\xi_{\ell_1,\ell_2}(r,g) = \frac{k_{1,0}^3 k_{2,0}^3 e^{-q_1\rho_1} e^{-q_2\rho_2}}{\pi^2} \int_{-\infty}^\infty \frac{\mathrm{d}t_1}{2\pi} e^{i\rho_1 t_1} \int_{-\infty}^\infty \frac{\mathrm{d}t_2}{2\pi} e^{i\rho_2 t_2} \phi^{q_1,q_2}(t_1,t_2) M_{\ell_1}^{q_1}(t_1) M_{\ell_2}^{q_2}(t_2) \tag{2.36}$$

which in the case of a separable ϕ reduces exactly to the outer product of two 1D SB FFTLog transformations.

Chapter 3
Visualization, Range of Validity, and Binning

In this chapter we look at our unique method for visualizaing the bispectrum through a practical example. Here we look at comparing our SPT theory models at both LO and NLO to see how they compare with an N-body simulation (effectively the ground truth for the scales we are interested in.) We also briefly touch on another issue that arises when comparing continuous theory to an estimated measurement from data.

3.1 Data Source

For our N-body data set we use a subset of the Quijote simulations [47], a set of 43,100 N-body simulations with a wide variety of cosmological parameters and results available at five different redshifts ($z = 0$, 0.5, 1, 2, and 3). For this study, we use the high-resolution, fiducial-cosmology sample, a set of 100 simulations run with 8 times as many dark matter particles. In detail, this sample of 100 simulations each has 1024^3 dark matter particles distributed over a volume of 1 Gpc^3/h^3, giving a fundamental wavenumber $k_f \approx 0.0063$ h/Mpc, with a cosmology in agreement with [97]. For more details about the simulations themselves, see [47].

We choose the high resolution simulations in particular because the higher resolution gives better accuracy at small scales, where we need it to determine the range of validity, at the cost of large scale error bars due to only having 100 simulations. We find this tradeoff to be worthwhile since it is already well known that LO and NLO perturbation theory are consistent with the nonlinear density field on large scales, so large error bars there do not impact the results of our analysis. In this work, we have devised a criteria for defining k_{NL} without being affected by the deviation due to large-scale cosmic variance.

From these simulations we use the precomputed power spectra [47] and then use the full dark-matter particle distribution to measure the bispectrum, all of which exists for five redshifts. The reason we remeasure the bispectrum is because the precomputed bispectra are not minimally binned, with $\Delta k = 2k_f$, so we remeasure them with minimal binning, $\Delta k = k_f$ to ensure the most accurate representation of the underlying data we can get and to minimize binning effects.

An important part of measuring the bispectrum is distributing the N-body particles onto a grid. For our grid decomposition we use *nbodykit*[98] with a custom **Julia** wrapper. We also follow the recommendations in [99] and use interlaced grids along with the third-order triangular-shaped clouds (TSC) method to dramatically reduce aliasing effects. For measuring the bispectrum from the decomposed grid we use the fast Scoccimarro estimator [99–101], specifically we use the code presented in [101] with some efficiency improvements. We measure the bispectrum up to $k_{\rm max} = 80k_f \approx 0.503\ h/\text{Mpc}$ to ensure we have sufficiently small enough scales to properly capture the deviation from perturbation theory at high redshift.

3.2 Theory Binning

Fourier-space clustering statistics measured from a density field defined at grid points are inherently binned with the fundamental frequency $k_F = 2\pi/L$. On the other hand, analytic theory models, like those in Sec. 2.1, can be calculated at each wavenumber without binning. This causes a discrepancy between the two even if the underlying statistic is identical, so a correction is essential when comparing analytic theory models and binned measurements. We refer to this as a binning correction. Note that theory models that are inherently gridded, such as the result from GridSPT [102], do not suffer from this problem but instead they are statistical and so require many realizations to reduce statistical errors.

To compute the binning correction we need to bin the analytic models the exact same way that we bin the statistical measures from simulations or real data. This is typically done by using *an estimator*, but, instead of taking data as input, the theory-model calculation is used as input. We then quantify the binning correction as the difference between the binned and unbinned theory relative to the unbinned theory. In this section, we shall measure the binning correction for the power spectrum and bispectrum.

For the power spectrum, the binning correction is typically very small except on scales near the fundamental wavenumber. To bin the theoretical power spectrum, we first

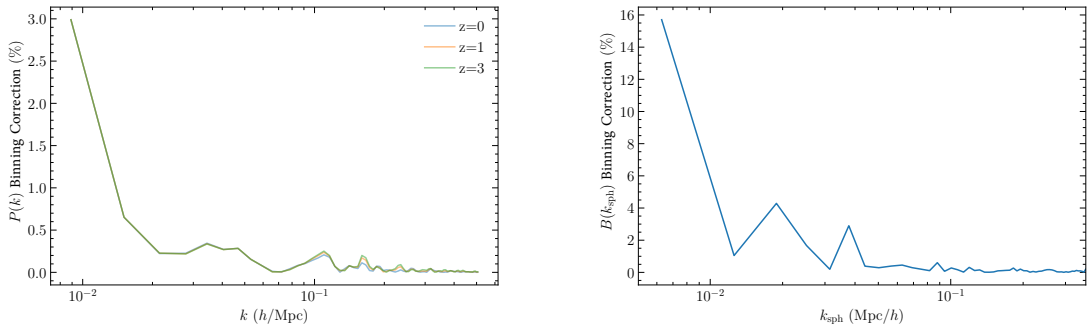

Figure 3.1. (*Left*): The binning correction on the LO + NLO power spectrum. The binning correction is plotted for three plotting redshifts ($z = 0$, 1, 3) to emphasize the contributions originating from the NLO part of the model, since only the NLO part has any redshift evolution. We see that binning correction matters only for very large scales, as it stays below 1% in all bins except the largest scale bin. (*Right*): The binning correction on the LO + NLO bispectrum, as a function of $k_{\rm sph}$ that we define later in Sec. 3.3. The visible binning correction is independent of redshift, signifying that the NLO contribution is much smaller than the LO contribution, so we only plot one redshift at $z = 0$. We see significantly larger errors than the case of the power spectrum with the largest bin reaching an error around 16 %. As a reminder, despite the noisy results, this is a purely analytic calculation involving no statistical variance. The binning correction depends only on the underlying analytic theory and the bin size.

generate a three-dimensional grid in Fourier space and assign the LO and NLO power spectrum calculated by using Eq. (2.3) to each grid point. We then measure the binned theory model for both LO and NLO power spectrum the same binning scheme as the direct measurement:

$$P_{\rm bin}(k_i) = \frac{1}{N_k} \sum_{|\boldsymbol{k}-k_i|\leq \frac{1}{2}k_F} P(\boldsymbol{k})\,. \tag{3.1}$$

Note that this is just the traditional direct power spectrum estimator but with $|\delta(\boldsymbol{k})|^2$ replaced with $P(\boldsymbol{k})$. We show the binning-correction error for the LO+NLO power spectrum in the left pane of Fig. 3.1. We have plotted the errors for our three plotting redshifts ($z = 0$, 1, 3) to emphasize the contributions coming from the NLO part, those that evolve with redshift, while the contributions that do not evolve with redshift are from the LO part, the linear power spectrum. We see that the binning effect contributes overwhelmingly more to the LO model, likely because it is only significant for the very largest scales. Our results are broadly consistent with the folklore that the binning correction only matters on very large scales, with only the very largest bin having an error larger than 1%. However, to use the large-scale bins for precision work, for example for measuring the local-type primordial non-Gaussianity [103–109], an accurate modeling of the binning correction is necessary.

For the bispectrum the binning effect is significantly more important than the power spectrum. [77] and more recently [79] have reported significant binning effects between a few and up to 10 percent and its triangular-configuration dependencies. The binning effect on the bispectrum is computationally expensive to study, because we must sum over all theory contribution on the grid:

$$B_{\rm bin}(k_1,k_2,k_3) = \frac{1}{N_{123}} \sum_{|\boldsymbol{k}_i-k_1|\le\frac{1}{2}k_F} \sum_{|\boldsymbol{k}_j-k_2|\le\frac{1}{2}k_F} \sum_{|\boldsymbol{k}_k-k_3|\le\frac{1}{2}k_F} B(\boldsymbol{k}_i,\boldsymbol{k}_j,\boldsymbol{k}_k)\,. \tag{3.2}$$

For example, for the bispectra considered in this work, it takes around a week for each of LO and NLO bispectrum models to get the binned form.

The right panel of Fig. 3.1 shows the binning correction for the NLO bispectrum, as a function of the $k_{\rm sph}$ that we define in Sec. 3.3. Unlike the power spectrum we do not plot this for multiple redshifts, since the contribution from the NLO part of the bispectrum, and hence the redshift evolution, is indistinguishably small on this plot. This means that nearly all of the binning effect, at least in $k_{\rm sph}$-space, is due to the LO part. When plotted in $k_{\rm sph}$-space, we see the bispectrum display similar behavior to the power spectrum, with significant binning errors on very large scale modes, reaching a maximum error of 16% in the largest bin.

Although we use the computationally slow exact binning in this work, as we only needed to compute it a few times, the long computation time of binning the bispectrum is a clear obstacle for precision bispectrum analysis given how significant the effect can be. A few alternative techniques have been developed. [110] have developed a method by averaging over the wavenumbers in a bin to generate an effective wavenumber

$$k_{{\rm eff},i}(k_1,k_2,k_3) = \frac{1}{N_{123}} \sum_{|\boldsymbol{k}_i-k_1|\le\frac{1}{2}k_F} \sum_{|\boldsymbol{k}_j-k_2|\le\frac{1}{2}k_F} \sum_{|\boldsymbol{k}_k-k_3|\le\frac{1}{2}k_F} \boldsymbol{k}_i\,, \tag{3.3}$$

and evaluating the theoretical-model bispectrum at that effective wavenumber. Following [111], [112] improves the method by sorting the wavenumbers, achieving a less than 5% binning error. Recently, [79] has introduced a scheme which uses Delaunay interpolation and constructs tetrahedra to reduce the computation time, achieving around 1% accuracy when using full Delaunay binning.

Finally, a comment is in order for the interpolation scheme that we use to compute the binned power spectrum and bispectrum. When computing the power spectrum and the NLO bispectrum at the grid points, we use cubic-spline interpolation to alleviate needing to compute the model at each grid point. For the power spectrum, which is a

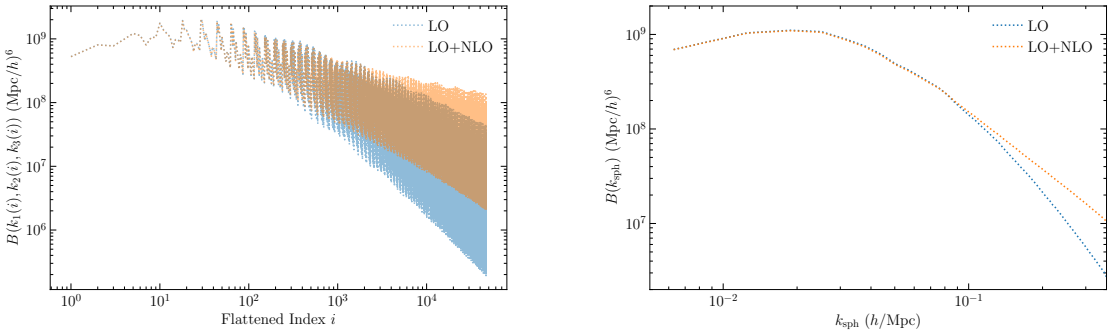

Figure 3.2. (*Left*): The LO and NLO bispectrum models plotted in the usual flattened index space. The flattened index is generated from creating an ordered set of tuples (k_1, k_2, k_3) with $k_1 \geq k_2 \geq k_3$ and incrementing in row-major order, that is incrementing k_3 first. Binned with bin size k_f (*Right*): The same two models plotted in spherical bispectrum space. It is both much easier to see the differences between the models and also more clear at exactly what scale they begin to diverge. Both plots are at $z = 0$.

very smooth function, this is unlikely to cause any significant effects. For the bispectrum, however, our testing shows this can have a significant effect. For example, we find $\sim$ 10% error on binning correction at the largest scales when computing Eq. (3.2) with the interpolated LO bispectrum instead of the exact LO bispectrum. Note, however, that we only use interpolation for the NLO-bispectrum binning correction, which is not very significant on any scales. Therefore, the interpolation should not affect our results.

3.3 The Spherical Bispectrum

The Bispectrum is a function of three semi-independent variables, k_1, k_2, and k_3, connected by the triangle condition: $k_a + k_b \leq k_c$ for all combination of $a \neq b \neq c$. While this does not hamper the bispectrum's ability as a cosmological probe, it is desirable to have a visualization tool showing the full scale- and configuration- dependence and facilitating the comparison among different models.

In literature, the most common method of visualizing the bispectrum is by flattening the three input wavenumbers into a contiguous one-dimensional flattened index each of which maps onto the triplet (k_1, k_2, k_3). The flattened index plot is not smooth when k_1 and k_2 values vary so the plot features are dominated by indexing effects rather than the nonlinearities. Also, it is non-trivial to assign a numeric scale to a specific bispectrum element, since there are three separate scales that contribute towards it. As a result, it is difficult to assign a single $k_{\rm NL}$ by examining the flattened index plot.

Other methods, such as heatmap triangle plots [80; 113], also exist although they can only be done by holding one of the wavenumbers constant. Thus, while highlighting the configuration-dependence of the bispectrum, the latter visualization methods are not convenient for direct comparison among different bispectra, for example, from theory calculation and simulation measurement.

To facilitate the comparison between different models with each other and against data visually, here we introduce the *spherical bispectrum*, which is essentially a coordinate transformation from the wavenumber triplet (k_1, k_2, k_3) to the spherical coordinate system ($k_{\rm sph}$, $\theta_{\rm sph}$, $\phi_{\rm sph}$). That is, by treating the wavenumbers of the bispectrum as equivalent to a Cartesian coordinate system (i.e. $k_1 = k_x$, $k_2 = k_y$, $k_3 = k_z$), we can then convert this three-dimensional coordinate system into spherical coordinates like so

$$\begin{aligned} k_{\rm sph} =& \sqrt{k_1^2 + k_2^2 + k_3^2}/\sqrt{3} \\ \phi_{\rm sph} =& \arctan\left(k_2/k_1\right) \\ \theta_{\rm sph} =& \arctan\left(\sqrt{k_1^2 + k_2^2}/k_3\right) . \end{aligned} \tag{3.4}$$

We then bin the bispectrum results $B(k_{\rm sph}, \phi_{\rm sph}, \theta_{\rm sph})$ based on $k_{\rm sph}$ and compute a weighted average off all the modes that fall into the same bin, weighted by the number of triangles that contribute to each mode. Formally, we may write the spherical bispectrum as

$$B_{\rm sph}(k_{\rm sph}) = \frac{\sum\limits_{|q_{\rm sph}-k_{\rm sph}|<\Delta/2} B(q_1,q_2,q_3) N_{\rm tri}(q_1,q_2,q_3)}{\sum\limits_{|q_{\rm sph}-k_{\rm sph}|<\Delta/2} N_{\rm tri}(q_1,q_2,q_3)} , \tag{3.5}$$

with the bin size Δ. The spherical bispectrum allows us to get a good measure of the bispectrum at a given scale, which is also easily plot-able in a standard form identical to the power spectrum. The $k_{\rm sph}$ can be thought of as a geometrically motivated way of defining a single *effective wavenumber* for each wavenumber triplet (k_1, k_2, k_3).

In Fig. 3.2, we plot two theory curves, the leading order (LO) and next-to-leading order (NLO) bispectrum in two different visualization schemes: the traditional flattened index style (Left) and the new spherical bispectrum style (Right). As shown in Fig. 3.2, we see significantly enhanced clarity with regards to where the two models deviate when looking at them in $k_{\rm sph}$-space compared to flattened-index space.

Note that if we only use the radial binning, the spherical bispectrum does lose some information compared to using the full bispectrum.

We can differentiate, however, the bispectrum's configuration dependence by taking

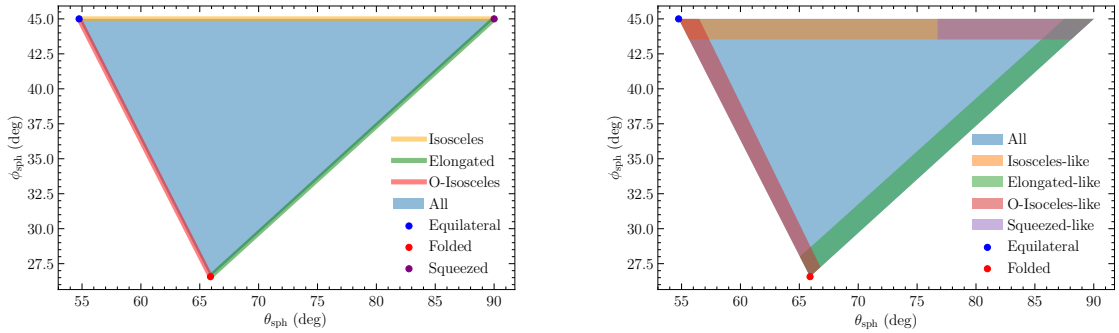

Figure 3.3. On the left is the formal definintions of each config in $\theta_{\rm sph} - \phi_{\rm sph}$ space. On the right is our expanded definitions for "-like" configs we use in this work. Here we have relaxed equality conditions by 5% and consider any mode with $k_1/k_3 > 3$ to be squeezed.

advantage of the angular information in the spherical coordinates. In Sec. 3.3.1, we use six triangular configurations (five used in the previous bispectrum analysis along with a new one), which are differentiated based on angular cuts in the spherical coordinates, giving us easy visual access to different parts of the angular domain.

3.3.1 Spherical Triangle Configuration

Probing specific range of angles in spherical coordinates allows us to look at the bispectrum's specific triangular configurations and to regain the information that is lost in the radial binning procedure. These configuration dependencies have been studied as ways to probe different physical mechanism of generating the bispectrum because the bispectrum at each configuration responds differently for different physical origins such as early Universe physics, non-linear growth of structure, and nonlinear bias [114].

There are six primary configurations we study here, and they are formally defined as follows:

- Equilateral: $k_1 = k_2 = k_3$
- Isosceles: $k_1 = k_2 > k_3$
- Folded: $k_1 = 2k_2 = 2k_3$
- Elongated: $k_1 = k_2 + k_3$
- Squeezed: $k_1 = k_2 \gg k_3$
- Obtuse-Isosceles (O-Isosceles): $k_1 > k_2 = k_3$

However, some of these configurations contain too few modes per bin and, even with reasonable bin sizes, using their strict definition makes them very stochastic. The problem is particularly severe for the Squeezed where the equality holds up for only limited number of configurations.

We alleviate this problem, and also include more information, by expanding their definitions while still only including modes that capture the same type of mode ratios. When used in this way we refer to them as "-like" configurations, for the remainder of this section, to differentiate from the formal definitions given above. In Fig. 3.3, we show the different configurations in $\theta_{\rm sph} - \phi_{\rm sph}$ space, both formally (*Left*) and with our expanded definitions (*Right*). For the rest of the work we drop the "-like" moniker and simply refer to the base name of the configuration.

Specifically, we do not expand the definition of Equilateral and Folded modes, as they are relatively smooth without the alteration. For every other mode, we relax the condition of equality in their formal definition to instead be a ratio lower limit. For example Isosceles modes formally impose $k_1 = k_2$ but for our isosceles-like modes we impose $k_2/k_1 > 0.95$. We impose this same relaxation on all "-like" modes. For the case of squeezed-like modes we introduce one further relaxation, the minimum ratio of $k_1/k_3 > 3$. These relaxations of the definitions not only smooth out the resulting functions but also allow for more angular information to be captured while still having a reasonable amount of overlap between different configurations.

3.3.2 Spherical Bispectrum Bin Completeness

An important consideration with the spherical bispectrum is that of bin completeness. Since the spherical bispectrum is a combination of various bispectrum elements with different (k_1, k_2, k_3) values, some elements may be put into a bin where other elements would in theory go but naively imposing a finite $k_{\rm max}$ could prevent those elements from being added into the bin.

We can calculate the largest, in terms of scale, bin where this occurs by finding the smallest bispectrum element which is not captured with a cut at $k_{\rm max}$ and then compute which bin it would fall into. If we characterize $k_{\rm max}$ with its integer form $n_{k,\rm max} = k_{\rm max}/k_F$ (k_F is the fundamental wavenumber) then depending on whether it is even or odd there are different forms for $n_{\rm sph,max}$, the integer form of the first incomplete bin, given by Tab. 3.1. There are a variety of different limits depending on the configuration.

To summarize, with the maximum wavenumber of $n_{k,\rm max}$, the spherical bispectrum is complete up to, but not including, $n_{\rm sph,max}$ indicated in Tab. 3.1.

	$n_{\rm sph,max}$ for even values of $n_{k,\rm max}$	$n_{\rm sph,max}$ for odd values of $n_{k,\rm max}$
General	$\sqrt{n_{k,\rm max}(n_{k,\rm max}+2)+4/3}/\sqrt{2}$	$(n_{k,\rm max}+1)/\sqrt{2}$
Folded	$(n_{k,\rm max}+2)/\sqrt{2}$	$(n_{k,\rm max}+1)/\sqrt{2}$
Elongated	$\sqrt{n_{k,\rm max}(n_{k,\rm max}+2)+4/3}/\sqrt{2}$	$(n_{k,\rm max}+1)/\sqrt{2}$
O-Isosceles	$\sqrt{n_{k,\rm max}(n_{k,\rm max}+8/3)+2}/\sqrt{2}$	$(n_{k,\rm max}+1)/\sqrt{2}$
Equilateral	$(n_{k,\rm max}+1)$	$(n_{k,\rm max}+1)$
Isosceles	$\sqrt{2n_{k,\rm max}(n_{k,\rm max}+2)+3}/\sqrt{3}$	$\sqrt{2n_{k,\rm max}(n_{k,\rm max}+2)+3}/\sqrt{3}$
Squeezed	$\sqrt{2n_{k,\rm max}(n_{k,\rm max}+2)+3}/\sqrt{3}$	$\sqrt{2n_{k,\rm max}(n_{k,\rm max}+2)+3}/\sqrt{3}$

Table 3.1. The value of $n_{\rm sph,max} = k_{\rm sph,max}/k_f$ for each configuration when $n_{k,\rm max}$ is even/odd. This is calculated by finding the smallest uncaptured mode for each configuration and then calculating its $k_{\rm sph}$.

3.4 Range of Validity

In this section, we present out results for the range of validity for both power and bispectrum at both LO and NLO. First, let us define the range of validity.

While the general consensus in literature is that the nonlinear scale, or range of validity for the linear model, is where the NLO correction is a sizable fraction of the LO contribution, the exact definition of the nonlinear scale can vary throughout the literature. In this work, we use a more data-driven approach and compute a χ^2-like statistic to determine $k_{\rm NL}$ where the simulation and theory models diverge beyond our accuracy threshold. Specifically, for a clustering statistic F, e.g. the power spectrum or bispectrum, we compute $n_{NL} = k_{NL}/k_f$ through

$$\frac{1}{n_{NL}}\sum_{i=1}^{n_{NL}}\frac{(F_{{\rm theory},i}-F_{{\rm sim},i})^2}{\sigma^2_{F_i,\rm sim}+\sigma^2_{F_i,\rm theory}} < (1.5)^2\,, \tag{3.6}$$

where $\sigma_{F_i,\rm sim}$ is the statistical error on the mean of the clustering statistic measured from the simulations at point i. The $\sigma_{F_i,\rm theory}$ in denominator is an induced statistical error on the theory to take our accuracy threshold into account, defined as

$$\sigma_{F_i,\rm theory} = \frac{\rm acc}{2}F_{\rm theory}(k_i)\,, \tag{3.7}$$

where acc is our desired accuracy threshold, e.g. 1% for the power spectrum. This theoretical error term, while only contributing acc/2 correction to cosmic variance, dominates over the shot-noise error near $k_{\rm NL}$. The contribution from the first five modes is suppressed by the usual cosmic variance and stays less than 1% of the summation,

which is dominated by contributions near $k_{\rm NL}$. In effect, what this computes is the average deviation from our accuracy threshold in units of the error, i.e. in units of sigma, and finds where that crosses 1.5 sigma.

A final note about our choice of 1.5 sigma is in order. Here, the 1.5 sigma constraint is somewhat arbitrary and was determined by empirical inspection, to match the $k_{\rm NL}$ we determine in Eq. (3.6) and the values from the comparison plots such as Fig. 3.5 and Fig. 3.7: using 1 sigma is too strict and 2 sigma is too lenient. The choice of threshold sigma, however, does not alter the results in any significant way and merely shifts the specific values of k_{NL} up or down while maintaining the same general relationships. Typically the difference from 1 to 1.5 and 1.5 to 2 is about a 10% difference at each step. For values of $k_{\rm NL}$ that do not fall exactly on a simulation bin center we use cubic spline interpolation to increase our precision.

3.4.1 Power Spectrum

To visualize the differences between the two (LO and LO+NLO) models and the N-body result we present a plot of all three curves at all three plotting redshifts ($z = 0,\ 1,\ 3$) in Fig. 3.4. To facilitate visualization of the nonlinearities in BAO, we also divide the curves by the no-wiggle power spectrum from [1] on the right panel of Fig. 3.4.

Here, we see excellent agreement between everything on large scales, with the small-scale agreement being highly dependent on redshift, as expected [37]. The non-wiggle plots emphasize the baryon acoustic oscillation (BAO) feature and show that LO+NLO perturbation theory prediction can accurately capture the nonlinearities in BAO at $z = 3$, while failing at lower redshifts ($z = 0,\ 1$).

We also show the error plots for our three plotting redshifts ($z = 0,\ 1,\ 3$) in the left panel of Fig. 3.5 along with overplotted lines to highlight 1% and 2% residuals. We see the expected redshift evolution that both LO and NLO perturbation theory predictions become more accurate at higher redshifts. Corresponding $k_{\rm NL}$ values as we compute following Eq. (3.6) can be seen for all redshifts and models in the right panel of Fig. 3.5. Note that there is a sharp discontinuity in the "Linear 1%" model. This sudden increase of $k_{\rm NL}$ is due to the first BAO wiggle being inconsistent to 1% at low redshift but consistent at high redshift. Besides that, the scaling shows the expected behavior with slow increases on either side of the linear discontinuity and steep increases at each redshift step for the LO+NLO model.

We fit a simple model to the results of our calculation for the LO+NLO results and

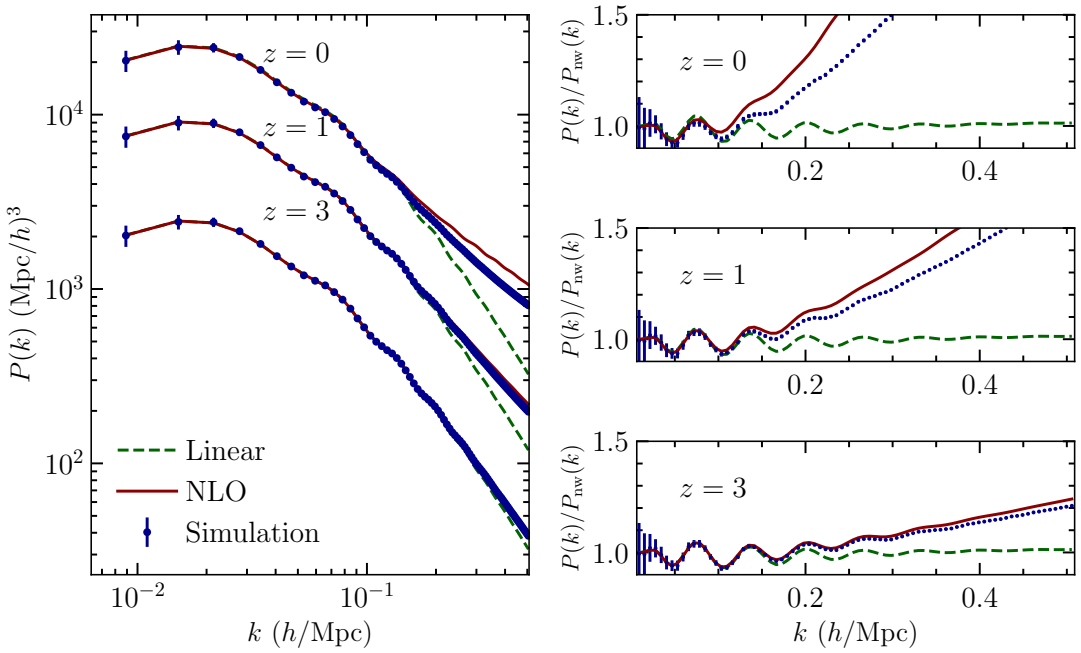

Figure 3.4. (*Left*): The power spectrum for all three of our models at all three plotting redshifts (0, 1, 3). We plot all three redshifts on the same plot since the scaling makes them mostly distinct. The largest valued set of power spectra is the $z = 0$ set, while the smallest is the $z = 3$ set. It can clearly be seen by eye how much better the high redshift curves match at smaller scales compared to the $z = 0$ set.
(*Right*): The various power spectrum models divided by the no-wiggle power spectrum from [1]. The redshifts follow the same pattern as on the left. Note that for both plots the errors are actually five-sigma errors to enhance visibility.

get an expression

$$\frac{k_{\rm NL}(z)}{h/\text{Mpc}} = 0.0502 + 0.0251 \left(\frac{D(z)}{D(0)}\right)^{-1.939} \tag{3.8}$$

where $D(z)$ is the linear growth factor. We do not fit a similar curve for the linear model due to the discontinuity caused by the first BAO wiggle. Along with our basic fit model we also look at the model described in [2]. This takes the form

$$\frac{k_{\rm NL}(z)^2}{6\pi^2} \int_0^{k_{NL}(z)} P_L(q, z)\, \mathrm{d}q < 0.18 \tag{3.9}$$

Where the constant on the right hand side varies depending on the model, here we use their $C^{\rm SPT}_{1\%}$. We find these k_{NL} values for our L+NLO model and plot it alongside our data and model in the right panel of Fig. 3.5. Our fitted model is quite consistent with our results, particularly at higher redshifts. The [2] model has similar behaviour to

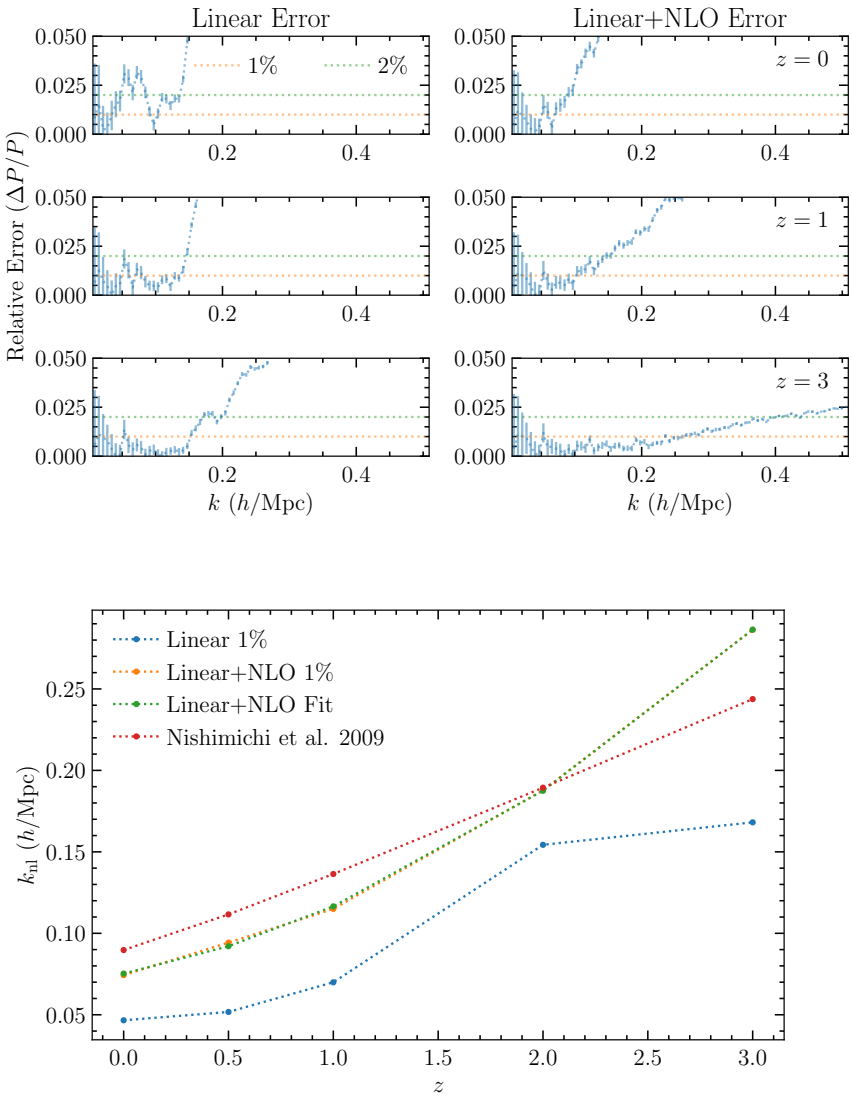

Figure 3.5. (*Top*): The relative error for each model compared to the simulation at three different redshifts, from top to bottom $z = 0$, $z = 1$, $z = 3$. Left: The error for the three linear models. Here we see significant redshift evolution, with the first point inconsistent with 1% going from ~ 0.05 h/Mpc at $z = 0$ to ~ 0.15 h/Mpc at $z = 3$. Right: The error for the three NLO models sees a similar redshift evolution, going from diverging at ~ 0.09 h/Mpc at $z = 0$ to ~ 0.3 h/Mpc at $z = 3$. It also remains consistently better than just the linear model. Overall we see significant accuracy improvement from both increasing the linear model to NLO and from increasing redshift.
(*Bottom*): The value of $k_{\rm NL}$ for each redshift using both linear and L+NLO models. These values were computed using Eq. (3.6). We see a clear increase with redshift for both linear and NLO models, expected for perturbative methods. We fit a simple model to our results, given by Eq. (3.8) that we plot alongside the model given by [2]. Note that although the form of the model is cosmology independent it was calibrated using a significantly different cosmology so differences of these levels are not unexpected. The same caution should be taken when applying our fit model.

our model, albeit with different scaling at high redshift, not unexpected for a model that was calibrated with a significantly different cosmology, WMAP3 [115] ($\Omega_m = 0.234$ $\sigma_8 = 0.76$) vs Planck18 [97] ($\Omega_m = 0.315$ $\sigma_8 = 0.811$). The difference suggests that care should be taken before applying Eq. (3.8) that, even though it is written in a form to be generalizable to other cosmologies, is likely to have errors when applied to moderately different cosmologies.

3.4.2 Bispectrum

Similarly to the power-spectrum case, here we present spherical bispectrum plots for all redshifts ($z = 0$, 1, 3) and models (LO and LO+NLO) in Fig. 3.6. We see very similar behavior to the power spectrum, one of our motivations for introducing the spherical-bispectrum visualization technique, with the LO+NLO model having better overall agreement and the agreement becomes better with redshift. Since the full bispectrum does not have a single scale associated with each element, we define the range of validity $k_{\rm sph,NL}$ based off the spherical bispectrum. The use of $k_{\rm sph,NL}$ allows us to clearly analyze a single effective scale for deviation of the two models from N-body data.

We essentially use Eq. (3.6) but with $B(k_{\rm sph})$ as F, and with a few different cutoff errors, 2-5%, instead of 1% as for the power spectrum since both observational and statistical errors are larger for the bispectrum. This is because the bispectrum is a higher-order statistic, involving a larger number of individual measurements. We present relative error plots of both LO and LO+NLO perturbative bispectrum models at our three plotting redshifts ($z = 0$, 1, 3) in the top panels of Fig. 3.7 with overplotted lines to highlight 2% and 5% errors, the bounds of our analysis. We again see a similar pattern with LO+NLO having better accuracy than LO, and the accuracy also increasing with redshift for both models. Our final results for the total bispectrum $k_{\rm sph,nl}$ are presented in the Fig. 3.7. Due to the difference between $k_{\rm sph}$ and k and the nature of $B_{\rm sph}$ itself, it is hard to make a direct comparison between the bottom panel of Fig. 3.7 and the right panel of Fig. 3.5. Nevertheless, we can read off the trend that $k_{\rm NL}$ with 1% accuracy in power spectrum corresponds to $k_{\rm sph,NL}$ with 3% accuracy in bispectrum.

We can also perform this comparison between the theory calculation and N-body results for specific configurations to disentangle the averaging effect in $B_{\rm sph}$. This study can also clarify that the accuracy of PT's bispectrum modeling depends on the configuration. To compute $k^{\rm (config)}_{\rm sph,NL}$ at each cutoff percentage, we again use Eq. (3.6) but with the bispectrum filtered to a specific configuration, instead of the bispectrum of all modes. We repeat the calculation for each model and with all six configurations.

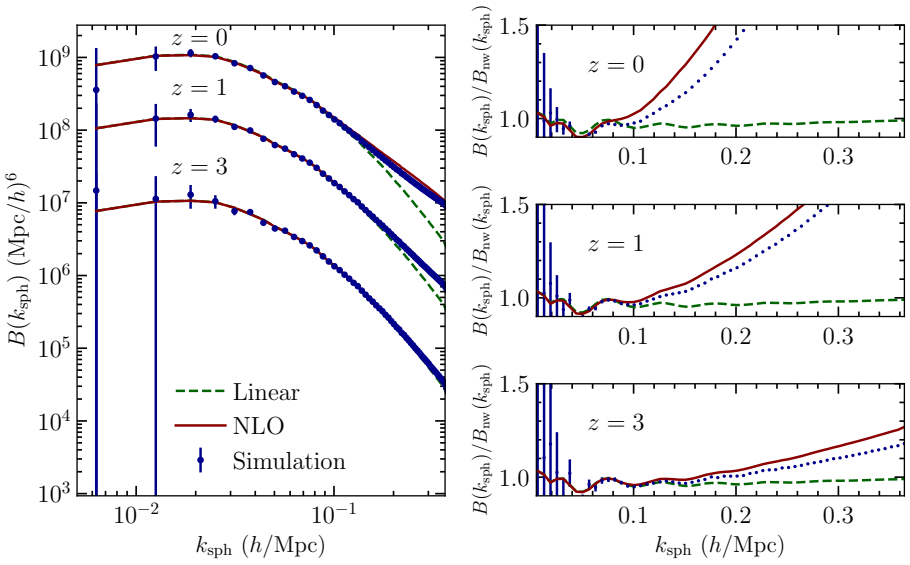

Figure 3.6. Left: The bispectrum for all three of our models at all three plotting redshifts (0, 1, 3). We plot all three redshifts on the same plot since the scaling makes them mostly distinct. The largest valued set of bispectra is the z=0 set, while the smallest is the z=3 set. It can clearly be seen by eye how much better the high redshift curves match at smaller scales compared to the z=0 set. Right: The various bispectrum models divided by the no-wiggle bispectrum, the LO bispectrum generated using the no-wiggle power spectrum from [1]. The redshifts follow the same pattern as on the left.

We show the results for the each configuration in Fig. 3.8 and Fig. 3.9. Here we see that most configurations behave in a similar way, LO+NLO is more accurate than just LO, often by a significant amount, and accuracy improves dramatically at higher redshifts with our accuracy threshold having the expected minor scaling. There are a number of mildly anomalous results in that there are a number of points where LO is equally as accurate as LO+NLO, in the All, Isosceles, and Obtuse-Isosceles plots we see a slight decrease in accuracy going from $z = 2$ to $z = 3$. We attribute these features to either be statistical fluctuations or a consequence of imperfect binning corrections, some configurations are significantly more dependent on the binning effect than others [77; 79]. Due to the inaccuracy of our large-scale bispectrum measurements we leave the investigation of this problem for future work. A few other features of interest in the plot are the Equilateral curves having little variation with threshold. This represents the Equilateral models being very accurate with a sudden divergence from the model causing all the thresholds to be passed at the same point. There are also a few discontinuous points with the same cause as for the LO power spectrum (the blue line in the right panel of Fig. 3.5), a feature that isn't captured at lower redshifts accurately that falls

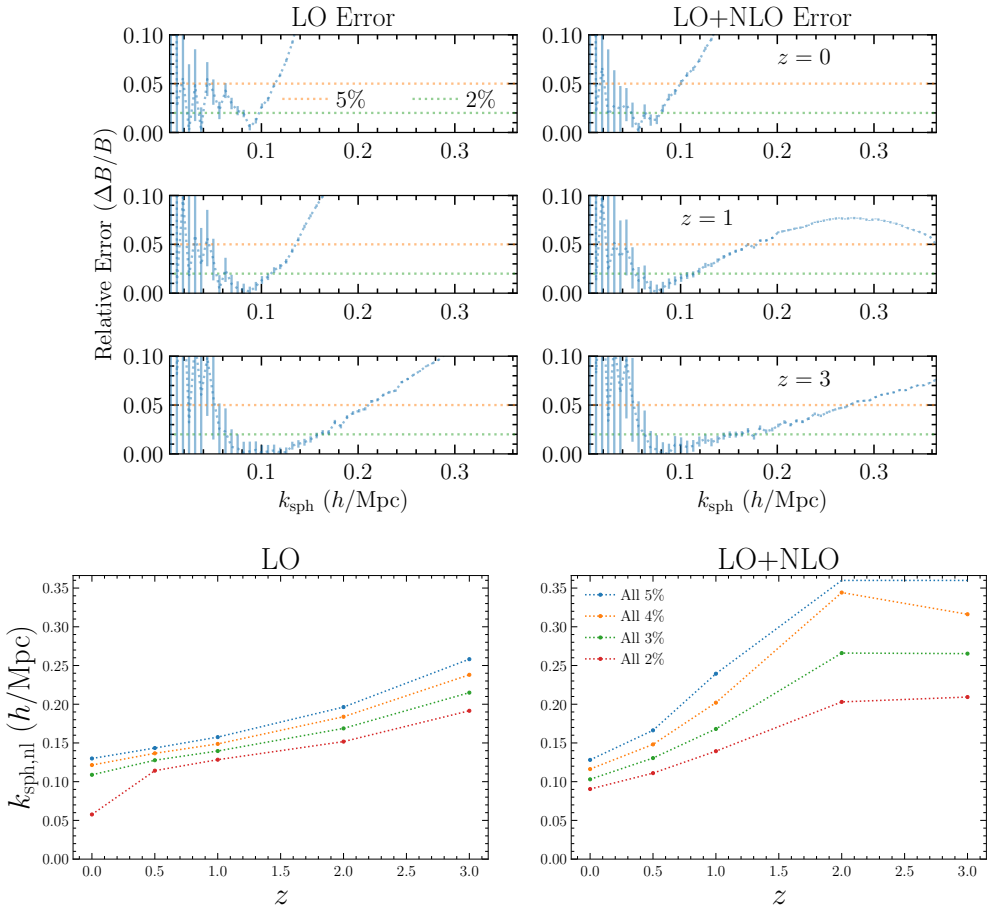

Figure 3.7. (*Top*): The relative error for each model compared to the simulation at three different redshifts, from top to bottom $z = 0$, $z = 1$, $z = 3$. Left: The error for the three LO models. Here we see significant redshift evolution, with the first point inconsistent with 5% going from ~ 0.2 h/Mpc at $z = 0$ to ~ 0.375 h/Mpc at $z = 3$. Right: The error for the three LO+NLO models sees a similar redshift evolution, going from diverging at ~ 0.2 h/Mpc at $z = 0$ to ~ 0.5 h/Mpc at $z = 3$. It also remains consistently better than just the linear model. Overall we see significant accuracy improvement from both increasing the LO model to LO+NLO and from increasing redshift.
(*Bottom*): The value of $k_{\rm sph,nl}$ found using Eq. (3.6) with the spherical bispectrum at four different threshold values. Left: The LO bispectrum results at four different accuracy thresholds. In general we see a smooth increase in $k_{\rm sph,nl}$ with both redshift and accuracy threshold. Right: The results for the LO+NLO model at four accuracy thresholds. Generally the results are similar to the LO results, except for a slight flattening/decrease between redshifts 2 and 3. The 5% results also hit the maximum value for which $k_{\rm sph}$ is complete, implying it is a lower bound.

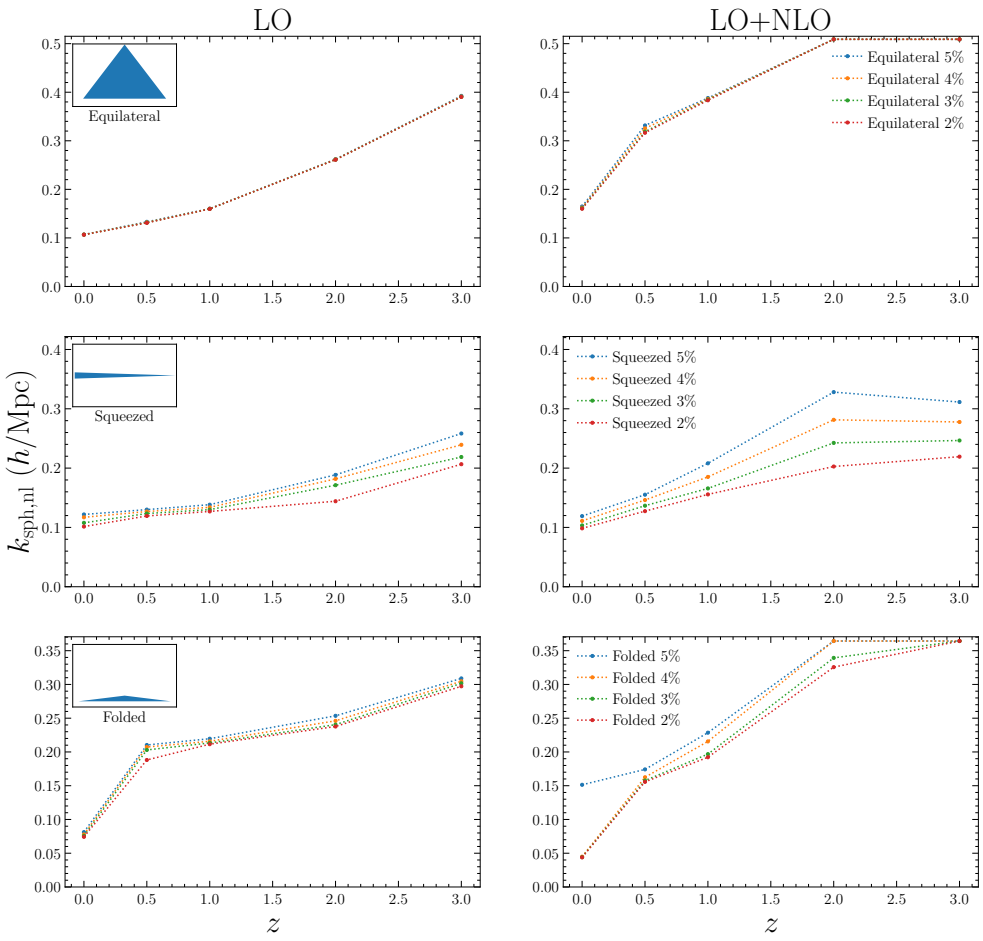

Figure 3.8. The value of $k_{\mathrm{sph,nl}}$ found using Eq. (3.6) with the spherical bispectrum, filtered to a specific configuration, at four different threshold values. Left: The results using the LO bispectrum model. Inset in each plot is a representative triangle showing the definition of the configuration. The equilateral results show that the threshold accuracy, within our bounds, does not change $k_{\mathrm{sph,nl}}$, signifying that the loss of accuracy is abrupt, but has a reasonable redshift scaling. Squeezed configurations seem to behave as expected, although the dependence on accuracy threshold is quite weak. Folded configurations seems to have little accuracy dependence, and experiences a significant jump from redshift 0 to 0.5. Right: The results for the LO+NLO model. At NLO Equilateral configurations retain their lack of dependence on accuracy threshold. It also hits the maximum of the data at both redshift 2 and 3, representing lower bounds. NLO Squeezed configurations have a much stronger accuracy dependence, with an added flattening between redshift 2 and 3. At NLO Folded configurations have more of a dependence on accuracy, hitting the maximum value at redshift 2, for some thresholds, and redshift 3, for all thresholds.

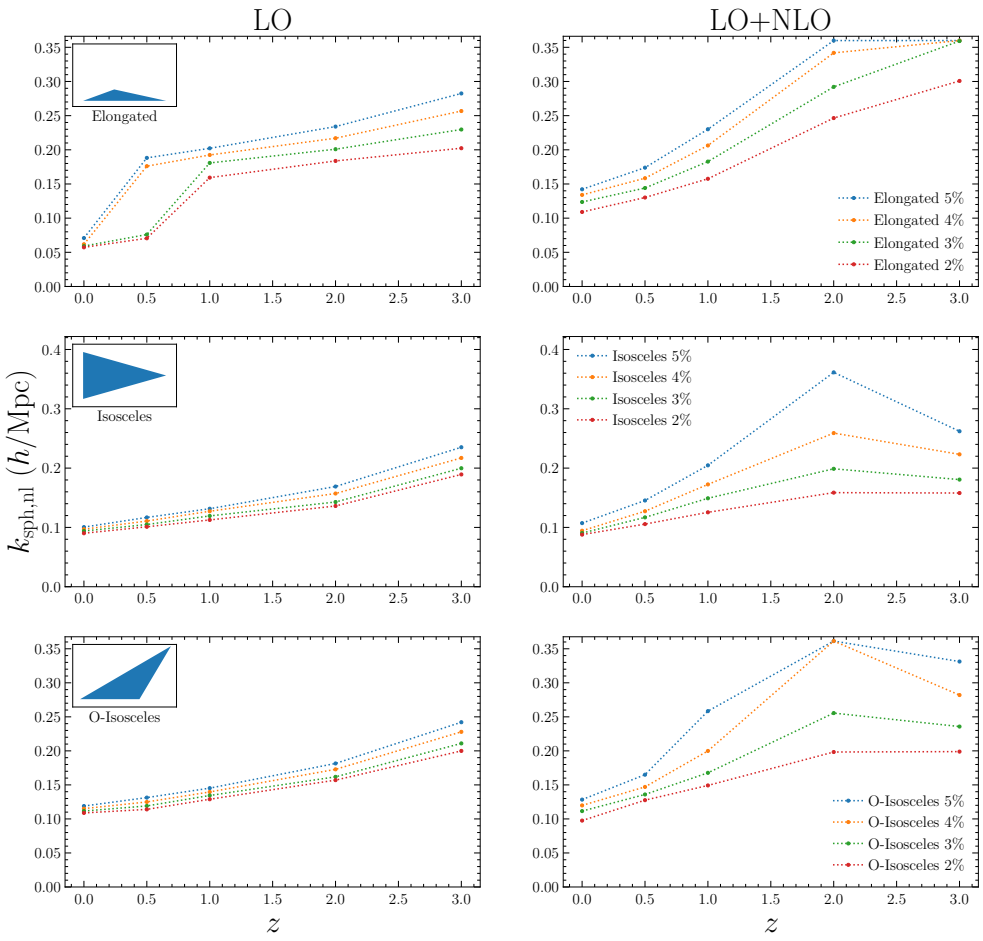

Figure 3.9. The value of $k_{\mathrm{sph,nl}}$ found using Eq. (3.6) with the spherical bispectrum, filtered to a specific configuration, at four different threshold values. Left: The results using the LO bispectrum model. Inset in each plot is a representative triangle showing the definition of the configuration. The elongated results show expected redshift and accuracy scaling, except between redshift 0 and 1 where the higher thresholds scale rapidly while the lower thresholds more slowly. The Isosceles configuration results show reasonable scaling with redshift, with a weak dependence on accuracy threshold. Similarly the Obtuse-Isosceles results are very similar to the Isosceles results. Right: The results for the LO+NLO model. At NLO Elongated configurations display the expected scaling, with some of the redshift 2 and 3 results hitting the maximum value, implying a lower bound. The NLO Isosceles configurations have a strange feature where there is a significant drop from redshift 2 to 3, at least for 5% accuracy. There are many potential causes for this, an unlikely statistical fluctuation, an unexpected binning error, or many other possibilities. At NLO Obtuse-Isosceles behaves similarly to Isosceles, with a drop from redshift 2 to 3, although it does hit the maximum value at redshift 2.

under the threshold as the redshift increases.

Chapter 4
The Galaxy Power Spectrum with Selection Effects

Combining all contributions we have discussed in Sec. 2.2, we find the expression for the one-loop (adding LO and NLO) galaxy power spectrum in redshift space as follows. Following the convention in [4], we organize the final result in the following way:

$$P^{gg,s}_{\rm LO+NLO}(k,\mu) = P^{gg,s}_{l+hd}(k,\mu) + P^{gg,s}_{22}(k,\mu) + 2P^{gg,s}_{13}(k,\mu)\,. \tag{4.1}$$

Here, we absorb all of the non-integral terms into a single term $P^{gg,s}_{l+hd}(k,\mu)$ which contains the leading order (LO) Kaiser terms, the stochastic terms and the higher derivative terms:

$$\begin{aligned} P^{gg,s}_{l+hd}(k,\mu) &= \left(b_1 - b_\eta f\mu^2\right)^2 P_L(k) + P^{\{0\}}_\epsilon + k^2 P^{\{2\}}_\epsilon + \mu^2 k^2 b_\eta P^{\{2\}}_{\epsilon\varepsilon_\eta} \\ &- 2\left[b_1 b_{\nabla^2\delta} - \mu^2 f b_\eta \left(b_{\nabla^2\delta} + b_1\beta_{\nabla^2\boldsymbol{v}} + b_1\beta_{\partial^2_\parallel\boldsymbol{v}}\mu^2\right) + \mu^4 f^2 b^2_\eta \left(\beta_{\nabla^2\boldsymbol{v}} + \beta_{\partial^2_\parallel\boldsymbol{v}}\mu^2\right)\right] k^2 P_L(k)\,. \end{aligned} \tag{4.2}$$

We further divide the rest of the NLO terms as $P^{gg,s}_{22}(k,\mu)$ that comes from the multiplication of two second order quantities, and $P^{gg,s}_{13}(k,\mu)$ that comes from the multiplication of linear order quantities and third order quantities. Including all local and selection observables in Eq. (2.14) and Eq. (2.24), there are 16 deterministic bias parameters to begin with.

The expression for $P^{gg,s}_{22}(k,\mu)$ may be written as

$$P^{gg,s}_{22}(k,\mu) = \sum_{\mathcal{O},\mathcal{O}'\in\mathfrak{D}_2} b_{\mathcal{O}} b_{\mathcal{O}'} \mathcal{I}^{\mathcal{O},\mathcal{O}'}(k,\mu)\,, \tag{4.3}$$

where the summation runs over all second order terms $\mathfrak{D}_2$ contributing to $\delta_{g,s}$ in Eq. (2.21):

$$\mathfrak{D}_2 = \left\{\delta^{(2)}, \eta^{(2)}, \delta^2, K^2, \delta\eta, \eta^2, (KK)_\parallel, \Pi^{[2]}_\parallel, u_\parallel\partial_\parallel\delta, u_\parallel\partial_\parallel\eta\right\}\,, \tag{4.4}$$

with associated coefficients for the second order contributions that we call $b_{\mathcal{O}}$

$$\{b_{\mathcal{O}}\}_{\mathfrak{D}_2} = \left\{b_1, b_\eta, b_{\delta^2} = b_2/2, b_{K^2}, b_{\delta\eta}, b_{\eta^2}, b_{(KK)_\parallel}, b_{\Pi^{[2]}_\parallel}, -b_1, -b_\eta\right\}\,. \tag{4.5}$$

The superscript () denotes the order of the operator, and no superscript denotes linear order. The functions $\mathcal{I}^{\mathcal{O},\mathcal{O}'}$ are the two-point correlators of the second-order operators:

$$\langle\mathcal{O}(\boldsymbol{k})\mathcal{O}'(\boldsymbol{k})\rangle = (2\pi)^3\mathcal{I}^{\mathcal{O},\mathcal{O}'}(k,\mu)\delta^D(\boldsymbol{k}+\boldsymbol{k}')\,, \tag{4.6}$$

and one can find the explicit formula of $\mathcal{I}^{\mathcal{O},\mathcal{O}'}(k,\mu)$ in terms of a loop integration over two linear power spectra in Ref. [4]. Taking all binary combinations of 10 terms in the second order expansion (Eq. (4.4)), one might expect that we need to compute 55 different $\mathcal{I}^{\mathcal{O},\mathcal{O}'}(k,\mu)$ terms. Ref. [4], however, further reduces the number of integrals, ends up finding that

$$P^{gg,s}_{22}(k,\mu) = \sum_{n=0}^{4}\sum_{(m,p)}\mathcal{A}_{n(m,p)}(f,\{b_{\mathcal{O}}\}_{\mathfrak{D}_2})\mathcal{I}_{mp}(k)\mu^{2n}\,, \tag{4.7}$$

with

$$\mathcal{I}_{mp}(k) \equiv 2\left[\int_{\boldsymbol{q}}\frac{q^{p-2}k^{6-p}}{|\boldsymbol{k}-\boldsymbol{q}|^4}\mu^m_{\hat{\boldsymbol{k}},\hat{\boldsymbol{q}}}P_{\rm L}(q)P_{\rm L}(|\boldsymbol{k}-\boldsymbol{q}|) - \frac{\delta_{p6}}{m+1}\left(\int_{\boldsymbol{q}}[P_{\rm L}(q)]^2\right)\right]\,. \tag{4.8}$$

It turns out that 23 combinations of (m,p) pairs suffices for the calculation of $P^{gg,s}_{22}(k,\mu)$.

Note that this form of $P^{gg,s}_{22}(k,\mu)$ does not suit the FFTLog-based fast calculation method that we are developing in this paper, and we develop an alternative expression using the Hankel transformation in Sec. 4.

The expression for $P^{gg,s}_{13}(k,\mu)$ takes a similar form

$$P^{gg,s}_{13}(k,\mu) = \sum_{\mathcal{O}\in\mathfrak{D}_3}\left(b_1 - b_\eta f\mu^2\right)b_{\mathcal{O}}f^{n_f(\mathcal{O})}f_{\mathcal{O}}(k,\mu)P_L(k)\,. \tag{4.9}$$

The NLO term $P^{gg,s}_{13}(k,\mu)$ is constructed from multiplying third order quantities with the linear order quantities that are encoded in the $(b_1 - b_\eta f\mu^2)$ term in the expression.

The summation runs over the third order contributions $\mathfrak{D}_3$, which are

$$\begin{aligned}\mathfrak{D}_3 = \Big\{&\delta^{(3)}, \eta^{(3)}, 2\mathrm{tr}[KK^{(2)}], \delta\eta^{(2)}, 2\eta\eta^{(2)}, 2(KK^{(2)})_\parallel, O_{td}, \delta\Pi^{[2]}_\parallel, \eta\Pi^{[2]}_\parallel, (\Pi^{[2]}K)_\parallel, s^k\partial_k\Pi^{[2]}_\parallel, \\ &u^{(2)}_\parallel\partial_\parallel\delta, u^{(2)}_\parallel\partial_\parallel\eta, u_\parallel\partial_\parallel\eta^{(2)}, u_\parallel\partial_\parallel\Pi^{[2]}_\parallel, \Pi^{[3]}_\parallel\Big\}\,,\end{aligned} \tag{4.10}$$

with corresponding coefficients $\{b_\mathcal{O}\}_{\mathfrak{D}_3}$ in the third order expressoin of $\delta_{g,s}$:

$$\begin{aligned}\{b_\mathcal{O}\}_{\mathfrak{D}_3} = \Big\{&b_1, b_\eta, b_{K^2}, b_{\delta\eta}, b_{\eta^2}, b_{(KK)_\parallel}, b_{td}, b_{\delta\Pi^{[2]}_\parallel}, b_{\eta\Pi^{[2]}_\parallel}, b_{(\Pi^{[2]}K)_\parallel}, -b_{\Pi^{[2]}_\parallel}, \\ &-b_1, -b_\eta, -b_\eta, -b_{\Pi^{[2]}_\parallel}, b_{\Pi^{[3]}_\parallel} + 2b_{\Pi^{[2]}_\parallel}\Big\}\,.\end{aligned} \tag{4.11}$$

Note that the set $\mathfrak{D}_3$ excludes the third order contributions coming from the product of three first-order operators. This is because we absorb their contribution into the coefficients of Eq. (4.2) by renormalization (see App. C.1 of Ref. [4] for the details). In addition to the bias parameters, each velocity-oriented operator in $\mathfrak{D}_3$ is multiplied with the linear growth rate f with the power denoted as $n_f(\mathcal{O})$ in Eq. (4.9). This power is the same as the number of velocity terms (either η or $u_\parallel$) in the operator:

$$\{n_f(\mathcal{O})\}_{\mathfrak{D}_3} = \{0, 1, 0, 1, 2, 0, 0, 0, 1, 0, 0, 1, 2, 2, 1, 0\}\,, \tag{4.12}$$

in the same order as the previous two sets.

Finally, the function

$$f_\mathcal{O}(k,\mu) = (1, \mu^2, \mu^4)\boldsymbol{\mathcal{M}}(\mathcal{O})\begin{bmatrix}\mathcal{I}_1(k)\\ \mathcal{I}_2(k)\\ \mathcal{I}_3(k)\\ \mathcal{I}_4(k)\\ \mathcal{I}_5(k)\end{bmatrix}\,, \tag{4.13}$$

contains the loop integrals $\mathcal{I}_n(k)$, which are (see App. D of [4] for the details)

$$\begin{aligned}\mathcal{I}_1(k) &= k^2\int_{\boldsymbol{q}}\frac{\boldsymbol{k}\cdot\boldsymbol{q}}{q^2|\boldsymbol{k}-\boldsymbol{q}|^2}(1-\mu^2_{\boldsymbol{k},\boldsymbol{q}})P_L(q)\\ \mathcal{I}_2(k) &= k^2\int_{\boldsymbol{q}}\frac{q^2}{q^2|\boldsymbol{k}-\boldsymbol{q}|^2}(1-\mu^2_{\boldsymbol{k},\boldsymbol{q}})P_L(q)\\ \mathcal{I}_3(k) &= \int_{\boldsymbol{q}}\left[\frac{q^2}{|\boldsymbol{k}-\boldsymbol{q}|^2}(1-\mu^2_{\boldsymbol{k},\boldsymbol{q}})-\frac{2}{3}\right]P_L(q)\end{aligned}$$

$$\mathcal{I}_4(k) = \int_{\boldsymbol{q}} \left[\frac{(\hat{\boldsymbol{k}}\cdot\boldsymbol{q})^2}{|\boldsymbol{k}-\boldsymbol{q}|^2}(1-\mu^2_{\boldsymbol{k},\boldsymbol{q}}) - \frac{2}{15} \right] P_L(q)$$
$$\mathcal{I}_5(k) = \int_{\boldsymbol{q}} \left[\frac{(\hat{\boldsymbol{k}}\cdot\boldsymbol{q})^4}{q^2|\boldsymbol{k}-\boldsymbol{q}|^2}(1-\mu^2_{\boldsymbol{k},\boldsymbol{q}}) - \frac{2}{35} \right] P_L(q)\,. \tag{4.14}$$

Here, $\boldsymbol{\mathcal{M}}(\mathcal{O})$ is the 3×5-coefficient matrix defined for each third-order operator. We present the matrices in App. B.

The main equation Eq. (4.1) combined with each component in Eq. (4.2), Eq. (4.7), and Eq. (4.9) completes the expression for observed (redshift-space) galaxy power spectrum to one-loop (LO+NLO) order. To compute the one-loop power spectrum, we need to evaluate the 28 (23 for $I_{mp}(k,\mu)$ and 5 for $I_n(k)$) two-dimensional integrals. To reduce the computational burden we reduce them into one-dimensional integrals which can be carried out faster by using the FFTlog-based method [66–69].

4.1 P22

Although the expression Eq. (4.7) is compact with only 23 $\mathcal{I}_{mp}(k)$ integrals, we find it difficult to manipulate $\mathcal{I}_{mp}(k)$ integrals into a form suitable for the FFTLog transformation. To take advantage of the FFTLog transformation, instead, we start from the second order kernel for the redshift-space density contrast as presented in Eq. (86) of [4]:

$$\begin{aligned}
Z_2(\boldsymbol{q}_1,\boldsymbol{q}_2) &= \frac{1}{2}b_2 + \frac{1}{9}b_{(KK)_\parallel} - \frac{1}{3}b_{K^2} + \frac{5}{7}\left(b_1 + b_{\Pi^{[2]}_\parallel}\mu^2\right) - \frac{3}{7}fb_\eta\mu^2 \\
&+ \frac{1}{2}\left(b_1 - fb_\eta\mu^2\right)\frac{k^2\boldsymbol{q}_1\cdot\boldsymbol{q}_2}{q_1^2q_2^2} + \left[b_{K^2} - \frac{5}{7}b_1 + \left(\frac{3}{7}fb_\eta - \frac{5}{7}b_{\Pi^{[2]}_\parallel}\right)\mu^2\right]\frac{(\boldsymbol{q}_1\cdot\boldsymbol{q}_2)^2}{q_1^2q_2^2} \\
&+ \left(b_{\Pi^{[2]}_\parallel} + b_{(KK)_\parallel}\right)\frac{(\boldsymbol{q}_1\cdot\boldsymbol{q}_2)q_{1z}q_{2z}}{q_1^2q_2^2} - \frac{1}{6}\left(3f(b_{\delta\eta}+b_1) + 2b_{(KK)_\parallel}\right)\frac{q_{1z}^2q_2^2 + q_1^2q_{2z}^2}{q_1^2q_2^2} + f^2(b_{\eta^2}+b_\eta)\frac{q_{1z}^2q_{2z}^2}{q_1^2q_2^2} \\
&+ \frac{(fk\mu)^2}{2}\frac{q_{1z}q_{2z}}{q_1^2q_2^2} + \frac{fk\mu}{2}\left[\frac{q_{1z}}{q_1^2}\left(b_1 - f(b_\eta+1)\frac{q_{2z}^2}{q_2^2}\right) + \frac{q_{2z}}{q_2^2}\left(b_1 - f(b_\eta+1)\frac{q_{1z}^2}{q_1^2}\right)\right]\,,
\end{aligned} \tag{4.15}$$

where we define $q_{iz} = q_i\mu_{\boldsymbol{n},\boldsymbol{q}_i} = q_i(\hat{\boldsymbol{n}}\cdot\hat{\boldsymbol{q}}_i)$. With the kernel Z_2, the expression for $P_{22}^{gg,s}(k,\mu)$ becomes

$$\begin{aligned}
P_{22}^{gg,s}(k,\mu) &= 2\int_{\boldsymbol{q}}[Z_2(\boldsymbol{q},\boldsymbol{k}-\boldsymbol{q})]^2P_L(q)P_L(|\boldsymbol{k}-\boldsymbol{q}|) - 2\int_{\boldsymbol{q}}[Z_2(\boldsymbol{q},-\boldsymbol{q})P_L(q)]^2 \\
&= 2(2\pi)^3\int_{\boldsymbol{p}}\int_{\boldsymbol{q}}[Z_2(\boldsymbol{p},\boldsymbol{q})]^2P_L(p)P_L(q)\delta^D(\boldsymbol{p}+\boldsymbol{q}-\boldsymbol{k}) - 2\int_{\boldsymbol{q}}[Z_2(\boldsymbol{q},-\boldsymbol{q})P_L(q)]^2\,.
\end{aligned} \tag{4.16}$$

Note that we subtract the constant term that renormalizes the shot-noise contribution P_0. Next, we expand $[Z_2(\boldsymbol{p},\boldsymbol{q})]^2$, separating the angular dependence in terms of Legendre polynomials for each of the angles in the kernel, $\hat{\boldsymbol{n}}\cdot\hat{\boldsymbol{q}}$, $\hat{\boldsymbol{n}}\cdot\hat{\boldsymbol{p}}$, and $\hat{\boldsymbol{p}}\cdot\hat{\boldsymbol{q}}$. The expression for $P_{22}^{gg,s}(k)$ then becomes the linear combination

$$P_{22}^{gg,s}(k,\mu) = 2\sum_{abcn_1n_2} \mathcal{C}_{abc}^{n_1n_2}(k,\mu,f,b_O)\mathcal{I}_{abc}^{n_1n_2}(k,\mu)\,, \tag{4.17}$$

with the coefficients $\mathcal{C}_{abc}^{n_1n_2}$ and the integral

$$\mathcal{I}_{abc}^{n_1n_2}(k,\mu) = (2\pi)^3\int_{\boldsymbol{q}}\int_{\boldsymbol{p}} q^{n_1-2}p^{n_2-2}\delta_D(\boldsymbol{p}+\boldsymbol{q}-\boldsymbol{k})P_L(q)P_L(p)\mathcal{L}_a\left(\hat{\boldsymbol{n}}\cdot\hat{\boldsymbol{q}}\right)\mathcal{L}_b\left(\hat{\boldsymbol{n}}\cdot\hat{\boldsymbol{p}}\right)\mathcal{L}_c\left(\hat{\boldsymbol{p}}\cdot\hat{\boldsymbol{q}}\right)\,. \tag{4.18}$$

The angular integral can be further simplified to yield

$$\begin{aligned}\mathcal{I}_{abc}^{n_1n_2}(k,\mu) = (2\pi)^3(-1)^{a+b+c}\sum_{\ell_r}\mathcal{L}_{\ell_r}(\mu)(2\ell_r+1)\begin{pmatrix}a & b & \ell_r\\ 0 & 0 & 0\end{pmatrix}\sum_{\ell_a\ell_b} i^{\ell_a+\ell_b-\ell_r}(2\ell_a+1)(2\ell_b+1)\\ \times\begin{pmatrix}a & \ell_a & c\\ 0 & 0 & 0\end{pmatrix}\begin{pmatrix}b & \ell_b & c\\ 0 & 0 & 0\end{pmatrix}\begin{pmatrix}\ell_r & \ell_a & \ell_b\\ 0 & 0 & 0\end{pmatrix}\begin{Bmatrix}a & b & \ell_r\\ \ell_b & \ell_a & c\end{Bmatrix}\int\frac{dr}{2\pi^2}r^2 j_{\ell_r}(kr)\xi_{n_1-2}^{\ell_a}(r)\xi_{n_2-2}^{\ell_b}(r)\,,\end{aligned} \tag{4.19}$$

with a Wigner-3j symbol $\begin{pmatrix}a & b & c\\ 0 & 0 & 0\end{pmatrix}$, a Wigner-6j symbol $\begin{Bmatrix}a & b & c\\ d & e & f\end{Bmatrix}$, and $\xi_n^\ell(r)$ defined in Eq. (2.25). We present the detailed derivation of the angular integration in App. C.

Note that the Wigner symbols in Eq. (4.19) dictates that (A) $\ell_a+\ell_b-\ell_r$ is even which guarantees the integrand is real, and (B) the values of ℓ_a, ℓ_b, and ℓ_r are bounded by triangle conditions, for example, $|\ell_r-\ell_a|\le\ell_b\le\ell_r+\ell_a$, for any permutation and likewise for every other 3j symbol. We refer the readers to Ref. [116] for the other properties of Wigner symbols.

The coefficients $\mathcal{C}_{abc}^{n_1n_2}$ are too lengthy to list in the paper, and we present them in the supplementary material of [117]. In total there are 51 unique coefficients for the 83 different possible combinations of indices when taking into account the symmetry of the expression, $\mathcal{I}_{abc}^{n_1n_2}=\mathcal{I}_{bac}^{n_2n_1}$. Implementation of Eq. (4.17) along with Eq. (4.19) requires 98 FFTlog computations.

To reduce the number of FFTlog transformations, we manipulate Eq. (4.17) and Eq. (4.19) such that the FFTlog (r-integration) operation takes place only at the last step. That is, for a given combination of $k^n\mathcal{L}_\ell(\mu)j_{\ell_r}(kr)$, we pre-compute all *internal*

summations in Eq. (4.17) and Eq. (4.19) so that the final expression for the $P_{22}^{gg,s}(k,\mu)$ becomes

$$P_{22}^{gg,s}(k,\mu) = 2(2\pi)^3 \sum_{\ell=0}^{4} \mathcal{L}_{2\ell}(\mu) \sum_{n=0}^{4} k^n \sum_{\ell_r=0}^{8} \int \frac{\mathrm{d}r}{2\pi^2} r^2 j_{\ell_r}(kr) \mathcal{M}_{\ell_r}^{n,\ell}(f, b_{\mathcal{O}}, r)\,. \tag{4.20}$$

Here, $\mathcal{M}$ contains summation over Wigner symbols and $\xi_n^\ell(r)$ functions and depends on the parameters such as f and $b_{\mathcal{O}}$. We have also absorbed the renormalization contributions into $\mathcal{M}_{\ell_r}^{0,\ell}$. Again, the expression for $\mathcal{M}$ is very lengthy, so we present them only in the supplementary material of [117]. The final expression in Eq. (4.20) reduces the number of FFTlog transformation down to 73, a significant decrease from the earlier method using Eq. (4.19). For the numeric calculations in this work, and the code we provide, therefore, we use this form of $P_{22}^{gg,s}(k,\mu)$.

4.2 P13

To transform the 1-3 integrals in Eq. (4.9) into the numerically faster form of Eq. (2.25) we first factor them into radial and angular components, then do the angular integral analytically. This leaves us with just a radial integral which is in the form of a spherical Bessel transformation and can be done very quickly with FFTLog. That is, we can directly transform these integrals, $\mathcal{I}_i(k)$ defined in Eq. (4.14), with an identity from Ref. [64],

$$\int_{\boldsymbol{q}} \frac{1}{|\boldsymbol{k}-\boldsymbol{q}|^2} q^n (\hat{\boldsymbol{k}}\cdot\hat{\boldsymbol{q}})^\ell P_L(q) = \sum_{\ell'=0}^{\ell} (2\ell'+1)\alpha_{\ell\ell'} \int_0^\infty \mathrm{d}r\, r j_{\ell'}(kr) \xi_n^{\ell'}(r) \equiv \sum_{\ell'=0}^{\ell} (2\ell'+1)\alpha_{\ell\ell'} \mathcal{P}_{13}^{\ell,n}(k)\,, \tag{4.21}$$

with

$$\alpha_{\ell\ell'} = \begin{cases} \frac{\ell!}{2^{(\ell-\ell')/2}[(\ell-\ell')/2]!(\ell+\ell'+1)!!} & \text{if } \ell \geq \ell' \text{ and } \ell \text{ and } \ell' \text{ are both even or odd.} \\ 0 & \text{otherwise.} \end{cases} \tag{4.22}$$

Applying this identity to the five integrals in Eq. (4.14) results in

$$\mathcal{I}_1(k) = \frac{2k^3}{5}\left(\mathcal{P}_{13}^{1,-1}(k) - \mathcal{P}_{13}^{3,-1}(k)\right)$$
$$\mathcal{I}_2(k) = \frac{2k^2}{3}\left(\mathcal{P}_{13}^{0,0}(k) - \mathcal{P}_{13}^{2,0}(k)\right)$$

$$\mathcal{I}_3(k) = \frac{2}{3}\left(\mathcal{P}_{13}^{0,2}(k) - \mathcal{P}_{13}^{2,2}(k)\right)$$
$$\mathcal{I}_4(k) = \frac{2}{15}\mathcal{P}_{13}^{0,2}(k) + \frac{2}{21}\mathcal{P}_{13}^{2,2}(k) - \frac{8}{35}\mathcal{P}_{13}^{4,2}(k)$$
$$\mathcal{I}_5(k) = \frac{2}{35}\mathcal{P}_{13}^{0,2}(k) + \frac{2}{21}\mathcal{P}_{13}^{2,2}(k) - \frac{32}{385}\mathcal{P}_{13}^{4,2}(k) - \frac{16}{231}\mathcal{P}_{13}^{6,2}(k)\,. \tag{4.23}$$

Using these identities, we can calculate all of the integrals required for $P_{13}^{gg,s}(k,\mu)$ with 16 unique FFTLog transformations. It is worth noting that we have dropped the renormalization terms present in the original integrals, for example, in $I_3(k)$, $I_4(k)$ and $I_5(k)$. This is because FFTLog is immune to the constant (k-independent) contributions which requires the inclusion of $q = 0$ ($\log q = -\infty$).

The expressions for $P_{22}^{gg,s}$ and $P_{13}^{gg,s}$ have exactly four overlapping FFTLog transformations, resulting in a final total of 85 for the entire one-loop power spectrum model in the general bias expansion. Despite the seemingly large number of integrals that need to be done, this method is about a factor of thousand faster than using those integrals in Ref. [4], for example, going from ∼10 minutes to ∼1 second per power spectrum model on a 3.2 GHz Intel CPU with our Julia implementation.

4.3 Multipole Expansion

We decompose the line-of-sight angle dependence of the redshift-space power spectrum by expanding the μ-dependence into Legendre polynomials. When considering statistically homogeneous density and velocity fields at a constant time, the forward-directional velocity field is statistically in-distinguishable from the backward-directional velocity field; hence, the redshift-space power spectrum in this case only contains even power in μ. This case must be contrasted with the real universe where large-scale structure evolves along the line-of-sight direction, and such evolution generates odd-multipoles in the redshift-space power spectrum. This effect, however, is suppressed by a factor of $1/kr$ where r is the distance to the galaxy survey volume [51].

We denote the even-order Legendre multipoles as

$$P_{\rm LO+NLO}^{gg,s}(k,\mu) = \sum_{\ell=0}^{4} P_{\rm LO+NLO,2\ell}^{gg,s}(k)\mathcal{L}_{2\ell}(\mu) \equiv \sum_{\ell=0}^{4}\left[P_{l+hd,2\ell}^{gg,s}(k) + P_{22,2\ell}^{gg,s}(k) + 2P_{13,2\ell}^{gg,s}(k)\right]\mathcal{L}_{2\ell}(\mu)\,, \tag{4.24}$$

where

$$P^{gg,s}_{X,\ell}(k) = \frac{2\ell+1}{2}\int_{-1}^{1} \mathrm{d}\mu\, \mathcal{L}_\ell(\mu) P^{gg,s}_X(k,\mu). \tag{4.25}$$

We find the Legendre multipoles for the linear and higher derivative terms in Eq. (4.2) as

$$\begin{aligned}
P^{gg,s}_{l+hd,0}(k) &= b_1^2 P_L(k) - \frac{2}{15} b_1 P_L(k)\left[f b_\eta(-5\beta_{\nabla^2 \boldsymbol{v}} k^2 - 3\beta_{\partial^2_\parallel \boldsymbol{v}} k^2 + 5) + 15 b_{\nabla^2\delta} k^2\right] \\
&\quad - \frac{1}{35} f^2 P_L(k) b_\eta^2\left[14\beta_{\nabla^2\boldsymbol{v}} k^2 + 10\beta_{\partial^2_\parallel \boldsymbol{v}} k^2 - 7\right] + \frac{1}{3} k^2 b_\eta\left[2 b_{\nabla^2\delta} f P_L(k) + P^{\{2\}}_{\epsilon\varepsilon_\eta}\right] \\
&\quad + k^2 P^{\{2\}}_\epsilon + P^{\{0\}}_\epsilon \\
P^{gg,s}_{l+hd,2}(k) &= \frac{2}{21} b_\eta\left\{2 f P_L(k)\left[f b_\eta\left(3 - k^2(6\beta_{\nabla^2\boldsymbol{v}} + 5\beta_{\partial^2_\parallel \boldsymbol{v}})\right) + b_1\left(k^2(7\beta_{\nabla^2\boldsymbol{v}} + 6\beta_{\partial^2_\parallel \boldsymbol{v}}) - 7\right)\right]\right. \\
&\quad \left. + 7k^2(2 b_{\nabla^2\delta} f P_L(k) + P^{\{2\}}_{\epsilon\varepsilon_\eta})\right\} \\
P^{gg,s}_{l+hd,4}(k) &= -\frac{8}{385} f P_L(k) b_\eta\left[f b_\eta\left(22\beta_{\nabla^2\boldsymbol{v}} k^2 + 30\beta_{\partial^2_\parallel \boldsymbol{v}} k^2 - 11\right) - 22 b_1 \beta_{\partial^2_\parallel \boldsymbol{v}} k^2\right] \\
P^{gg,s}_{l+hd,6}(k) &= -\frac{32}{231}\beta_{\partial^2_\parallel \boldsymbol{v}} f^2 k^2 P_L(k) b_\eta^2.
\end{aligned} \tag{4.26}$$

For the 1-3 loop terms we get

$$P^{gg,s}_{13,\ell}(k) = \sum_{n=1}^{5} \mathcal{C}_n^{1-3,\ell}(f, \{b_\mathcal{O}\}_{\mathfrak{D}_3}) \mathcal{I}_n(k) P_L(k), \tag{4.27}$$

where $\mathcal{C}_n^{1-3,\ell}$ is a coefficient matrix listed in the supplementary material of [4]. The 2-2 loop terms are already in the proper format for multipole decomposition in Eq. (4.20).

4.4 Numerical Implementation

For the non-linear redshift-space power spectrum, we have implemented Eq. (4.2), Eq. (4.20), and Eq. (4.9) along with Eq. (4.23) in Julia. For the FFTlog transformations, we use the implementation of the TwoFAST module [69]. Our Julia module takes the linear power spectrum as an input and calculates the non-linear redshift-space power spectrum as a function of (k, μ) for given bias parameters $b_\mathcal{O}$ as well as the linear growth rate parameter $f = \mathrm{d}\ln D/\mathrm{d}\ln a$. One can of course calculate the multipole power spectrum as a function of wavenumber k as well.

In this section, we shall compare the outcome of the implementation with the previous results in literature [4; 37; 38; 64] to test the numerical stability and accuracy. For the calculations in this section we use the following numeric parameters, 1-D grid size $N = 16384$, $k_{\min} = e^{-25}$ h/Mpc, $k_{\max} = e^{25}$ h/Mpc, $r_{\min} = e^{-11}$ Mpc/h, $r_{\max} = e^{-11}$

Mpc/h. Our choice of FFTLog biasing parameter q is done using the procedure detailed in Sec. 2.3.

4.4.1 Matter Power Spectrum

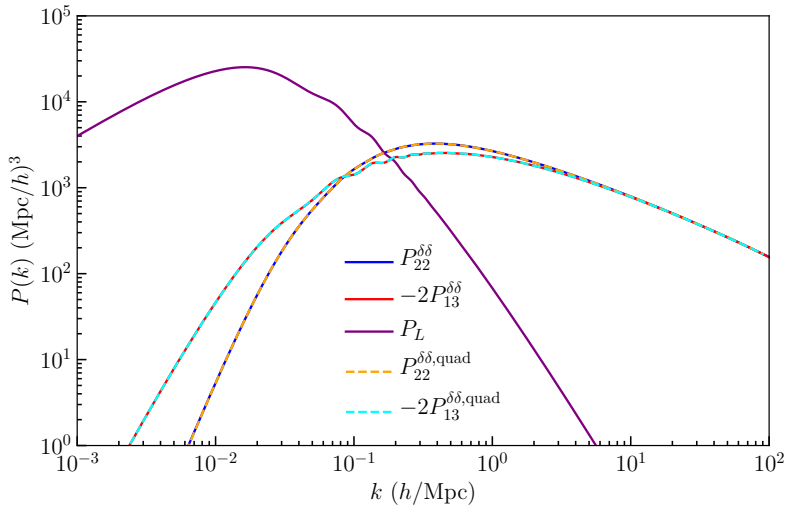

Figure 4.1. In green is our fiducial power spectrum. In blue is our codes calculation of $P_{22}^{\delta\delta}(k)$, and orange is our calculation of $P_{13}^{\delta\delta}(k)$. Both of these calculations were done using the methods described in Sec. 4.4. The dashed red and purple lines are results of manually integrating equations for $P_{22}^{\delta\delta}(k)$ and $P_{13}^{\delta\delta}(k)$. We see excellent agreement between the two methods, with the FFTLog based method being orders of magnitude faster. Note that the NLO perturbation theory breaks down around 0.2-0.5 h/Mpc depending on redshift

First, we perform the comparison with $P_{22}^{\delta\delta}(k)$ and $P_{13}^{\delta\delta}(k)$, both of which can be obtained by setting $b_1 = 1$ and all other parameters 0, in Fig. 4.1. Note that, in our implementation, $P_{13}^{\delta\delta}$ is given as

$$P_{13}^{\delta\delta,\mathcal{I}} = 3P_L(k)\left(\frac{2}{63}\mathcal{I}_1(k) + \frac{1}{42}\mathcal{I}_2(k) - \frac{1}{18}\mathcal{I}_3(k) - \frac{1}{18}k^2\sigma_v^2\right), \tag{4.28}$$

with

$$\sigma_v^2 = \int_{\boldsymbol{q}} \frac{P_L(q)}{q^2}\,. \tag{4.29}$$

That is, in order to obtain $P_{13}(k)$, in addition to the full 1-3 term with setting $b_O = 0$, $f = 0$, $b_1 = 1$, we need to add $-P_L(k)k^2\sigma_v^2/6$. In Fig. 4.1, we also plot $P_{13}^{\delta\delta,\mathrm{quad}}(k)$ and $P_{22}^{\delta\delta,\mathrm{quad}}(k)$ with the same computation method used in [37]. As shown there, different calculation methods agree within a sub-percent accuracy for all wavenumbers that we

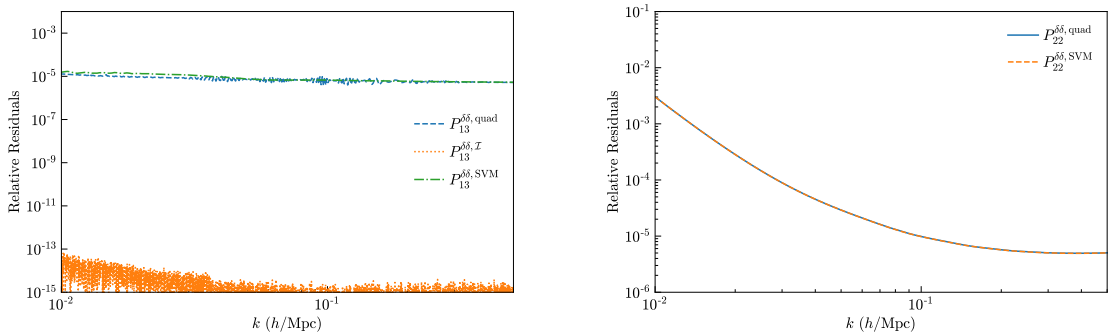

Figure 4.2. Left: The relative residuals of $P_{13}^{\delta\delta}(k)$ from this work calculated using three different methods. $P_{13}^{\delta\delta}$ is first calculated using our full one-loop code with the only bias parameters being $b_1 = 1$, then we compare it to the three methods described in Sec. 4.4.1. First we compute the integration directly using quadrature, quadosc, then as additional tests we use the additional expressions from Eq. (4.28) and Eq. (4.30). The errors compared to the quadrature method and Eq. (4.30) are around 0.001% well within any reasonable bounds, while the error compared to Eq. (4.28) is negligible. Right: The relative residuals of $P_{22}^{\delta\delta}(k)$ from this work calculated using two different methods. $P_{22}^{\delta\delta}$ is first calculated using our full one-loop code with the only bias parameter being $b_1 = 1$, then we compare it to the two methods described in Sec. 4.4.1. First we compute the integration directly using quadrature then as an additional test we use Eq. (4.31). The error on small scales is consistent with $P_{13}^{\delta\delta}$ at around 0.001% with the large scale errors, where the loop terms are less important, reaching 0.3%

plot here.

We have also calculated $P_{22}^{\delta\delta}(k)$ and $P_{13}^{\delta\delta}(k)$ by using an alternative FFTlog implementation of [64]:

$$P_{13}^{\delta\delta,\mathrm{SVM}}(k) = P_L(k)\left(\frac{67}{189}k^2\mathcal{P}_{13}^{0,0}(k) - \frac{1}{3}k^4\mathcal{P}_{13}^{0,-2}(k) + \frac{227}{315}k^3\mathcal{P}_{13}^{1,-1}(k) - \frac{37}{45}k\mathcal{P}_{13}^{1,1}(k)\right.$$
$$\left. -\frac{2}{3}k^4\mathcal{P}_{13}^{2,-2}(k) - \frac{46}{189}k^2\mathcal{P}_{13}^{2,0}(k) + \frac{76}{105}k^3\mathcal{P}_{13}^{3,-1}(k) + \frac{4}{15}k\mathcal{P}_{13}^{3,1}(k)\right). \tag{4.30}$$

$$P_{22}^{\delta\delta,\mathrm{SVM}}(k) = 4\pi\int_0^\infty \mathrm{d}r\, r^2 j_0(kr)\left[\frac{1219}{735}(\xi_0^0(r))^2 + \frac{1}{3}\xi_{-2}^0(r)\xi_2^0(r) - \frac{124}{35}\xi_{-1}^1(r)\xi_1^1(r)\right.$$
$$\left. +\frac{1342}{1029}(\xi_0^2(r))^2 + \frac{2}{3}\xi_{-2}^2(r)\xi_2^2(r) - \frac{16}{35}\xi_{-1}^3(r)\xi_1^3(r) + \frac{64}{1715}(\xi_0^4(r))^2\right]. \tag{4.31}$$

In Fig. 4.2, we plot the residuals between the method developed in this work with the previously discussed methods of calculating $P_{13}^{\delta\delta}$ and $P_{22}^{\delta\delta}$ (quadrature and Eqs. (4.28)–(4.31)). We again find excellent agreement between all methods, with differences consistently below 0.3% validating our numerical implementation. We also get an interesting

result from expanding our method analytically for the case of $P_{22}^{\delta\delta}(k)$

$$P_{22}^{\delta\delta}(k) = 4\pi \int_0^\infty \mathrm{d}r\, r^2 j_0(kr) \left(\frac{80}{147} \left(\xi_0^0(r)\right)^2 - \frac{800}{1029} \left(\xi_0^2(r)\right)^2 + \frac{80}{343} \left(\xi_0^4(r)\right)^2 + k^2 \left[\frac{4}{7} \left(\xi_{-1}^3(r)\right)^2 - \frac{4}{7} \left(\xi_{-1}^1(r)\right)^2 \right] + k^4 \left[\frac{1}{6} \left(\xi_{-2}^0(r)\right)^2 + \frac{1}{3} \left(\xi_{-2}^2(r)\right)^2 \right] \right) , \tag{4.32}$$

which provides a slightly faster way to compute $P_{22}^{\delta\delta}$, going from 12 total transformations to 10.

4.4.2 Pb2 & Pb22

We next consider two other limiting cases of $P_{22}^{gg,s}(k)$, $P_{b2}(k)$ and $P_{b22}(k)$ which are defined by considering only the local-in-matter-density (LIMD) bias expansion of $P_{22}^{gg,s}(k)$[38; 118]:

$$P_{22}^{\mathrm{LIMD}}(k) = b_1^2 \left[P_{22}^{\delta\delta}(k) + b_2 P_{b2}(k) + b_2^2 P_{b22}(k) \right] , \tag{4.33}$$

where the $P_{b2}(k)$ and $P_{b22}(k)$ are defined as

$$P_{b2}(k) = 2 \int_{\boldsymbol{q}} P_L(q) P_L(|\boldsymbol{k} - \boldsymbol{q}|) F_2^{(s)}(\boldsymbol{q}, \boldsymbol{k} - \boldsymbol{q}) , \tag{4.34}$$

and

$$P_{b22}(k) = \frac{1}{2} \int_{\boldsymbol{q}} P_L(q) \left[P_L(|\boldsymbol{k} - \boldsymbol{q}|) - P_L(q) \right] . \tag{4.35}$$

On the other hand, we can also extract $P_{b2}(k)$ and $P_{b22}(k)$ using our general bias method by solving the system of linear equation at each wavenumber k. In Fig. 4.3, we show the residuals between the results of the two different implementations. For all wavenubmers for which NLO contributions are relevant, the differences stays within a sub-percent accuracy.

4.5 The Galaxy Power Spectrum Response

With selection effects, the expression for the non-linear order one-loop power spectrum contains 22 bias parameters. The consistent cosmological analysis of the galaxy power spectrum in redshift space, therefore, must include these parameters along with the cosmological parameters. Having a plethora of parameters, the natural question is

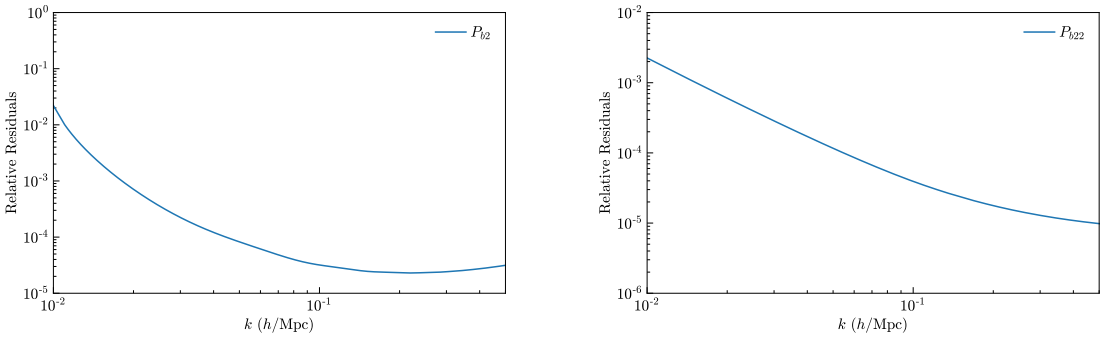

Figure 4.3. Left: Relative residuals for P_{b2} calculated using the full general bias expansion method described in this work, where we use two different sets of parameters for Eq. (4.33), compared to manually integrating using Eq. (4.34). We see a similar trend as in $P_{22}^{\delta\delta}$ with the error maximizing at large scales, where the loop terms are negligible, but remaining under 2%. Right: Relative residuals for P_{b22} calculated using the full general bias expansion method described in this work, where we use two different sets of parameters for Eq. (4.33), compared to manually integrating using Eq. (4.35). We see a similar trend to P_{b2} but with generally smaller errors, maxing out around 0.2%.

whether any of these parameters are strongly degenerate or not. The answer to this question depends, of course, sensitively on the survey parameters such as survey volume, number density and selection function. We can however glimpse the possible degeneracy between bias parameters by studying the power spectrum response, which is defined as

$$F_\ell(\theta, k) = \frac{1}{P_L(k)} \left. \frac{\mathrm{d}P^{gg,s}_{\mathrm{LO+NLO},\ell}(k)}{\mathrm{d}\theta} \right|_{\theta=\theta_f} , \tag{4.36}$$

for each parameter θ. Here, θ_f is the fiducial value listed in Tab. 4.1. The response appears in the usual statistical analysis based on the Fisher information matrix as following:

$$F_{ij} = \sum_\ell \sum_k w_\ell(k) \left[\frac{P_L(k)}{P^{gg,s}_{\mathrm{LO+NLO},\ell}(k)} \right]^2 F_\ell(\theta_i, k) F_\ell(\theta_j, k) \,, \tag{4.37}$$

where

$$w_\ell(k) \propto \frac{V_{\mathrm{survey}} k^2 \delta k}{\left[1 + 1/(\bar{n} P^{gg,s}_{\mathrm{LO+NLO},\ell}(k))\right]^2} \tag{4.38}$$

weights each k-mode differently taking into account the cosmic variance (numerator) and the finite galaxy density (denominator) effect. Note that $w_\ell(k)$ is inversely proportional to the variance of the power spectrum multipoles [119]. That is, we can think of the k-depending response functions as vectors whose inner product is the Fisher information matrix as defined above. The parameter degeneracy happens when the two response

Fiducial parameters for Figs. (4.4)–(4.8)			
b_1	1.5	$b_{\Pi^{[2]}_\parallel}$	0
b_2	-0.69	$b_{\Pi^{[3]}_\parallel}$	0
b_η	-1	$P^{\{0\}}_\epsilon$	0
b_{K^2}	-0.14	$b_{\nabla^2\delta}$	1
$b_{\delta\eta}$	-1.5	$\beta_{\nabla^2\boldsymbol{v}}$	1
b_{η^2}	1	$\beta_{\partial^2_\parallel\boldsymbol{v}}$	0
$b_{(KK)_\parallel}$	0	$P^{\{2\}}_\epsilon$	0
b_{td}	0.27	$P^{\{2\}}_{\epsilon\varepsilon_\eta}$	0
$b_{\delta\Pi^{[2]}_\parallel}$	0	$b_{(\Pi^{[2]}K)_\parallel}$	0
$b_{\eta\Pi^{[2]}_\parallel}$	0	f	0.53

Table 4.1. The fiducial values of each bias parameters that we take derivatives about for calculating the response function. The fiducial values of b_1, b_2, and b_{K^2} come from Tab. 6 of [3], while the fiducial values of b_η, $b_{\delta\eta}$, b_{η^2}, $b_{(KK)_\parallel}$, $b_{\Pi^{[2]}_\parallel}$, $b_{\delta\Pi^{[2]}_\parallel}$, $b_{\eta\Pi^{[2]}_\parallel}$, $b_{(\Pi^{[2]}K)_\parallel}$, $b_{\Pi^{[3]}_\parallel}$, $\beta_{\partial^2_\parallel\boldsymbol{v}}$ come from considering no selection effects, see Eq. 2.30 of [4]. The fiducial higher derivative biases are simply set to 1 arbitrarily. The fiducial value for b_{td} is set by Eq. (2.53) of [3]. The fiducial stochastic parameters are set as 0. Finally the fiducial value of f is set by $f \approx \Omega_m^{0.55}$ [5] with our fiducial Ω_m set by [6].

functions behave exactly the same way as a function of k.

In this section we use our code for calculating $P^{gg,s}_{\mathrm{LO+NLO},\ell}$ to examine the power spectrum response function defined in Eq. (4.36) for each bias parameter, and f. For reference, we show the power spectrum multipoles with the fiducial parameters shown in Tab. 4.1 in Fig. 4.4. For $\ell < 6$, the NLO multipole power spectrum is proportional to $P_L(k)$ on larger scales, which is our motivation of including $P_L(k)$ in the definition of the response in Eq. (4.36).

In Figs. (4.5)–(4.8), we show the response for the multipole power spectra $P_\ell(k)$ ($\ell = 0$, 2, 4, 6, 8). The responses for the monopole can be seen in Fig. 4.5. While many of the bias parameters are distinct, b_1, b_η, and f are almost perfectly degenerate on large-scales, which is already expected from the linear theory prediction: $P^{gg,s}_{l+hd,0}(k) \ni (b_1^2 - \frac{2}{3}b_1 f b_\eta + \frac{1}{5}f^2 b_\eta^2)P_L(k)$. On small scales, $k \gtrsim 0.1\,h/\mathrm{Mpc}$, however, the NLO contribution potentially distinguishes f. We also find that b_{K^2} and $b_{(KK)_\parallel}$ are degenerate on small scales, although they behave differently on large scales. In the right panel, we show that, when just considering the monopole, the parameters b_{td}, $b_{\delta\Pi^{[2]}_\parallel}$, $b_{\eta\Pi^{[2]}}$, and $b_{(\Pi^{[2]}K)_\parallel}$ are also nearly perfectly degenerate on large scales.

The quadropole ($\ell = 2$) responses are presented in Fig. 4.6. Focusing on just the unresolved degeneracies in monopole, we find that, on small scales ($k \gtrsim 0.1\,h/\mathrm{Mpc}$), we

gain the ability to distinguish between b_1 and b_η. The quadropole also further breaks the b_{K^2}-$b_{(KK)_\parallel}$ degeneracy on small scales. With regards to the four parameters with the worst degeneracy we see some potential for $b_{\eta\Pi^{[2]}_\parallel}$ to be isolated on small scales, leaving only the three parameters $b_{\delta\Pi^{[2]}_\parallel}$, b_{td}, and $b_{(\Pi^{[2]}K)_\parallel}$ which are degenerate with each other. If we further include the octopole ($\ell = 4$), Fig. 4.7, then we see that it is independent of b_{td}, useful for breaking the primary remaining degeneracy, and that $b_{(\Pi^{[2]}K)_\parallel}$ could potentially be determined based on small scales, leaving no strong degeneracies between the parameters. While there is some potential in the $\ell = 6$ mode (Fig. 4.8) to clarify some of the parameters, given the small signal-to-noise ratio we anticipate that it does not significantly contribute towards breaking degeneracies, and similarly for the $\ell = 8$ mode (Fig. 4.8).

Of course, the discussion in this section is only based on the shape of the power spectrum response function. We however stress here that the scale- and angular- dependencies of all bias parameters are quite distinctive, so, when applied to the high-z galaxy surveys, the NLO power spectrum has a great potential for exploiting the cosmological information. In particular, the unique scale- and angular-dependence of the linear growth rate parameter f may enable us to measure the parameter as it is, instead of the usual combination of $f\sigma_8$.

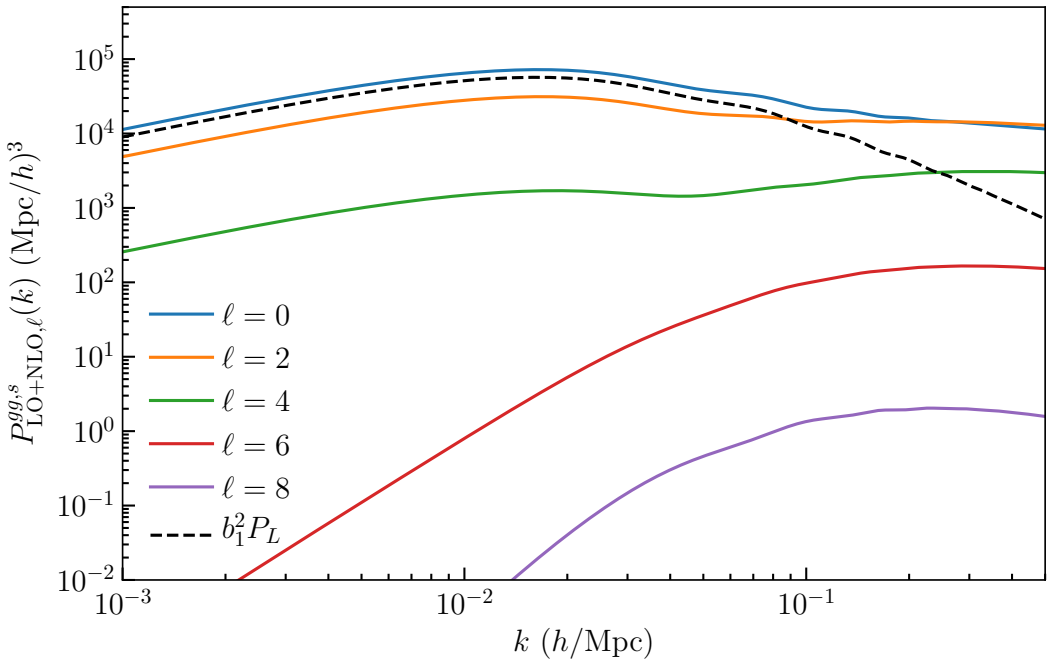

Figure 4.4. The power spectrum multipoles ($P^{gg,s}_{\mathrm{LO+NLO}\ell}(k)$) generated using the bias values in Tab. 4.1.

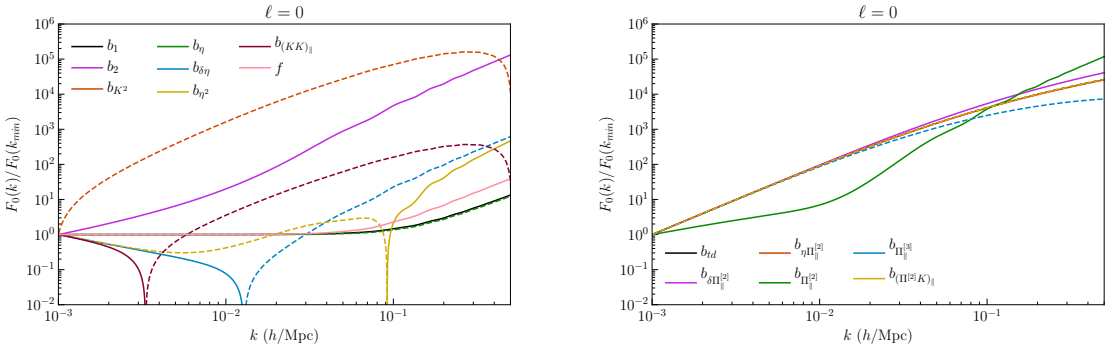

Figure 4.5. The response function for the monopole LO+NLO power spectrum. We neglect a few bias parameters that are described exactly analytically from Eq. (4.26). For discussion about the degeneracies between parameters see Sec. 4.5.

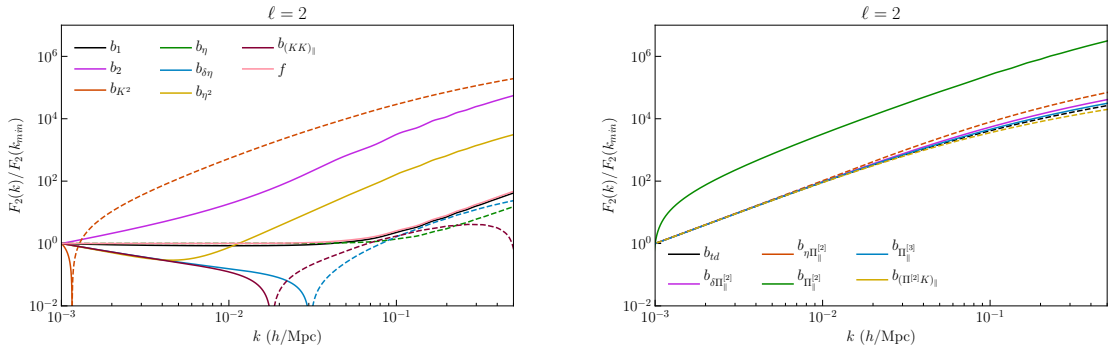

Figure 4.6. The response function for the quadropole LO+NLO power spectrum. We neglect a few bias parameters that are described exactly analytically from Eq. (4.26). For discussion about the degeneracies between parameters see Sec. 4.5.

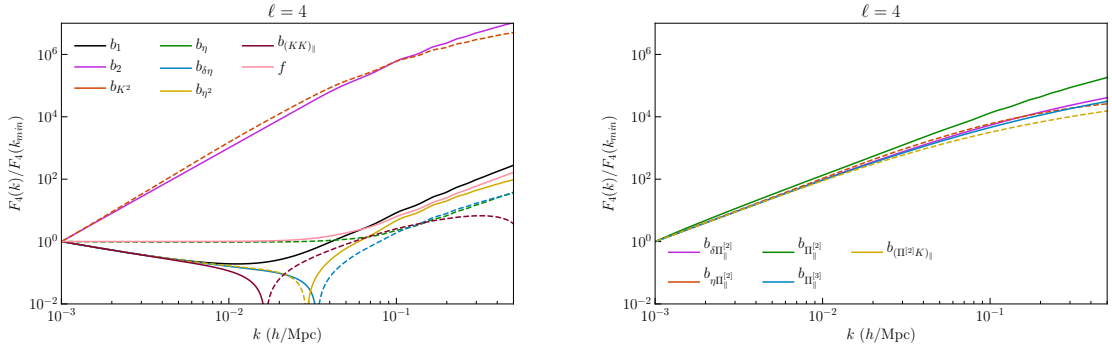

Figure 4.7. The response function for the octopole LO+NLO power spectrum. We neglect a few bias parameters that are described exactly analytically from Eq. (4.26). For discussion about the degeneracies between parameters see Sec. 4.5.

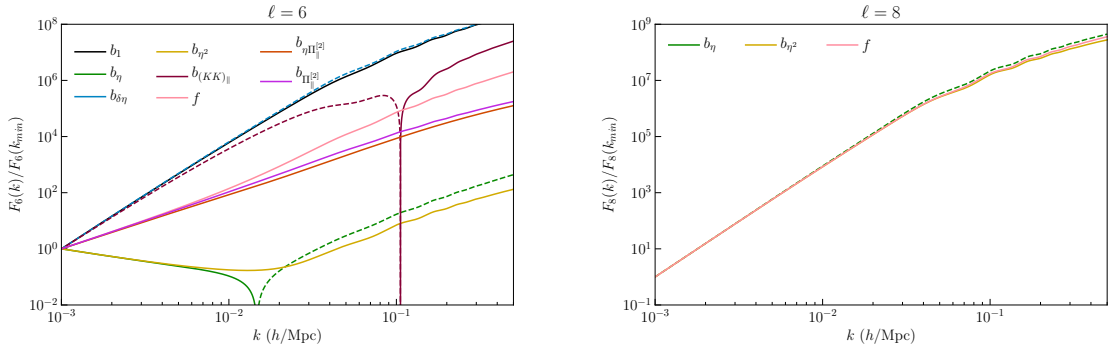

Figure 4.8. Left: The response function for the hexadecapole LO+NLO power spectrum. We neglect a few bias parameters that are described exactly analytically from Eq. (4.26). Right: The response function for the $\ell = 8$ LO+NLO power spectrum. For discussion about the degeneracies between parameters see Sec. 4.5.

Chapter 5
The Next-to-Leading Order Matter Bispectrum

We begin our analysis of the bispectrum by briefly restating some key parts of SPT we will use in this chapter.

5.1 Perturbation Theory Review

The perturbation theory ansatz density and velocity solutions are

$$\begin{aligned}\delta(\boldsymbol{k}) =&\delta_L(\boldsymbol{k}) + \int_{\boldsymbol{q}}\int_{\boldsymbol{p}} F_2^{(s)}(\boldsymbol{q},\boldsymbol{p})\delta_L(\boldsymbol{q})\delta_L(\boldsymbol{p})(2\pi)^3\delta^D(\boldsymbol{k}-\boldsymbol{q}-\boldsymbol{p}) + \cdots \\ \theta(\boldsymbol{k}) =&- aHf\left[\delta_L(\boldsymbol{k}) + \int_{\boldsymbol{q}}\int_{\boldsymbol{p}} G_2^{(s)}(\boldsymbol{q},\boldsymbol{p})\delta_L(\boldsymbol{q})\delta_L(\boldsymbol{p})(2\pi)^3\delta^D(\boldsymbol{k}-\boldsymbol{q}-\boldsymbol{p}) + \cdots\right]. \end{aligned} \tag{5.1}$$

The ansatz involves integration kernels whose complexity increases with the order of the solution. The second order kernels are

$$\begin{aligned} F_2^{(s)}(\boldsymbol{q},\boldsymbol{p}) =&\frac{5}{7} + \frac{1}{2}\frac{\boldsymbol{q}\cdot\boldsymbol{p}}{qp}\left(\frac{q}{p}+\frac{p}{q}\right) + \frac{2}{7}\left(\frac{\boldsymbol{q}\cdot\boldsymbol{p}}{qp}\right)^2 = \frac{5}{7} + \frac{1}{2}\mu_{q,p}\left(\frac{q}{p}+\frac{p}{q}\right) + \frac{2}{7}\mu_{q,p}^2 \\ =&\frac{5}{7} + \mu_{q,p}\frac{q^2+p^2+2pq\mu_{qp}}{2pq} - \mu_{q,p}^2 + \frac{2}{7}\mu_{q,p}^2 = \frac{5}{7}\left(1-\mu_{q,p}^2\right) + \frac{|\boldsymbol{p}+\boldsymbol{q}|^2}{2pq}\mu_{q,p} \\ G_2^{(s)}(\boldsymbol{q},\boldsymbol{p}) =&\frac{3}{7} + \frac{1}{2}\mu_{q,p}\left(\frac{q}{p}+\frac{p}{q}\right) + \frac{4}{7}\mu_{q,p}^2 = \frac{3}{7}\left(1-\mu_{q,p}^2\right) + \frac{|\boldsymbol{p}+\boldsymbol{q}|^2}{2pq}. \end{aligned} \tag{5.2}$$

The higher order kernels are generated by the following recurrence relation

$$F_n(\boldsymbol{q}_1,\cdots,\boldsymbol{q}_n) = \sum_{m=1}^{n-1}\frac{G_m^{(s)}(\boldsymbol{q}_1,\cdots,\boldsymbol{q}_m)}{(2n+3)(n-1)}\left[(2n+1)\frac{\boldsymbol{q}_{1\cdots n}\cdot\boldsymbol{q}_{1\cdots m}}{q_{1\cdots m}^2}F_{n-m}^{(s)}(\boldsymbol{q}_{m+1},\cdots,\boldsymbol{q}_n)\right.$$

$$+\frac{q_{1\cdots n}^2\left(\boldsymbol{q}_{1\cdots m}\cdot\boldsymbol{q}_{m+1\cdots n}\right)}{q_{1\cdots m}^2 q_{m+1\cdots n}^2}G_{n-m}^{(s)}(\boldsymbol{q}_{m+1},\cdots,\boldsymbol{q}_n)\Bigg]$$

$$G_n(\boldsymbol{q}_1,\cdots,\boldsymbol{q}_n)=\sum_{m=1}^{n-1}\frac{G_m^{(s)}(\boldsymbol{q}_1,\cdots,\boldsymbol{q}_m)}{(2n+3)(n-1)}\left[3\frac{\boldsymbol{q}_{1\cdots n}\cdot\boldsymbol{q}_{1\cdots m}}{q_{1\cdots m}^2}F_{n-m}^{(s)}(\boldsymbol{q}_{m+1},\cdots,\boldsymbol{q}_n)\right.$$
$$\left.+n\frac{q_{1\cdots n}^2\left(\boldsymbol{q}_{1\cdots m}\cdot\boldsymbol{q}_{m+1\cdots n}\right)}{q_{1\cdots m}^2 q_{m+1\cdots n}^2}G_{n-m}^{(s)}(\boldsymbol{q}_{m+1},\cdots,\boldsymbol{q}_n)\right]. \tag{5.3}$$

This gives third order kernels

$$F_3^{(s)}(\boldsymbol{q}_1,\boldsymbol{q}_2,\boldsymbol{q}_3)=\frac{2q_{123}^2}{54}\left(\frac{\boldsymbol{q}_1\cdot\boldsymbol{q}_{23}}{q_1^2q_{23}^2}G_2(\boldsymbol{q}_2,\boldsymbol{q}_3)\right)+\frac{7}{54}\left(\frac{\boldsymbol{q}_{123}\cdot\boldsymbol{q}_{23}}{q_{23}^2}G_2(\boldsymbol{q}_2,\boldsymbol{q}_3)\right)$$
$$+\frac{7}{54}\left(\frac{\boldsymbol{q}_{123}\cdot\boldsymbol{q}_1}{q_1^2}F_2(\boldsymbol{q}_2,\boldsymbol{q}_3)\right)+(2\text{ cyc.})$$
$$G_3^{(s)}(\boldsymbol{q}_1,\boldsymbol{q}_2,\boldsymbol{q}_3)=\frac{q_{123}^2}{9}\left(\frac{\boldsymbol{q}_1\cdot\boldsymbol{q}_{23}}{q_1^2q_{23}^2}G_2(\boldsymbol{q}_2,\boldsymbol{q}_3)\right)+\frac{1}{18}\left(\frac{\boldsymbol{q}_{123}\cdot\boldsymbol{q}_{23}}{q_{23}^2}G_2(\boldsymbol{q}_2,\boldsymbol{q}_3)\right)$$
$$+\frac{1}{18}\left(\frac{\boldsymbol{q}_{123}\cdot\boldsymbol{q}_1}{q_1^2}F_2(\boldsymbol{q}_2,\boldsymbol{q}_3)\right)+(2\text{ cyc.}). \tag{5.4}$$

The fourth order unsymmetrized density kernel is then

$$F_4(\boldsymbol{q}_1,\cdots,\boldsymbol{q}_4)=\sum_{m=1}^{3}\frac{G_m^{(s)}(\boldsymbol{q}_1,\cdots,\boldsymbol{q}_m)}{33}\left[\frac{q_{1234}^2(\boldsymbol{q}_{1\cdots m}\cdot\boldsymbol{q}_{m+1\cdots 4})}{q_{1\cdots m}^2q_{m+1\cdots 4}^2}G_{4-m}^{(s)}(\boldsymbol{q}_{m+1},\cdots,\boldsymbol{q}_4)\right.$$
$$\left.+9\frac{\boldsymbol{q}_{1234}\cdot\boldsymbol{q}_{1\cdots m}}{q_{1\cdots m}}F_{4-m}^{(s)}(\boldsymbol{q}_{m+1},\cdots,\boldsymbol{q}_4)\right]. \tag{5.5}$$

We symmetrize this in the usual way

$$F_4^{(s)}(\boldsymbol{q}_1,\cdots,\boldsymbol{q}_4)=\frac{1}{n!}\sum_\sigma F_4(\boldsymbol{q}_{\sigma 1},\cdots,\boldsymbol{q}_{\sigma 4}), \tag{5.6}$$

where σ is all permutations of the set $\{1,2,3,4\}$. Since we are only taking δ to 4th order we do not need G_4 in this work.

The NLO bispectrum can be written as

$$B^{\rm NLO}(k_1,k_2,k_3)=B_L(k_1,k_2,k_3)+B_{222}(k_1,k_2,k_3)+B_{411}(k_1,k_2,k_3)$$
$$+B_{123}^I(k_1,k_2,k_3)+B_{123}^{II}(k_1,k_2,k_3), \tag{5.7}$$

where

$$B_L=2F_2^{(s)}(\boldsymbol{k}_1,\boldsymbol{k}_2)P_L(k_1)P_L(k_2)+(2\text{ cyc.})$$

$$
\begin{aligned}
B_{222} &= 8\int_{\boldsymbol{q}} F_2^{(s)}(\boldsymbol{q},\boldsymbol{k}_1-\boldsymbol{q})F_2^{(s)}(-\boldsymbol{q},\boldsymbol{k}_2+\boldsymbol{q})F_2^{(s)}(\boldsymbol{q}-\boldsymbol{k}_1,-\boldsymbol{k}_2-\boldsymbol{q})P_L(q)P_L(|\boldsymbol{k}_1-\boldsymbol{q}|)P_L(|\boldsymbol{k}_2+\boldsymbol{q}|)\\
B_{411} &= 12P_L(k_1)P_L(k_2)\int_{\boldsymbol{q}} F_4^{(s)}(\boldsymbol{q},-\boldsymbol{q},-\boldsymbol{k}_1,-\boldsymbol{k}_2)P_L(q) + (2\text{ cyc.})\\
B_{123}^{I} &= 6P_L(k_1)\int_{\boldsymbol{q}} F_2^{(s)}(\boldsymbol{q},\boldsymbol{k}_2-\boldsymbol{q})F_3^{(s)}(-\boldsymbol{q},\boldsymbol{q}-\boldsymbol{k}_2,-\boldsymbol{k}_1)P_L(q)P_L(|\boldsymbol{k}_2-\boldsymbol{q}|) + (5\text{ cyc.})\\
B_{123}^{II} &= 6P_L(k_1)P_L(k_2)F_2^{(s)}(\boldsymbol{k}_1,\boldsymbol{k}_2)\int_{\boldsymbol{q}} F_3^{(s)}(\boldsymbol{q},-\boldsymbol{q},\boldsymbol{k}_2)P_L(q) + (5\text{ cyc.})\,. \qquad (5.8)
\end{aligned}
$$

The B_{123}^{II} term is trivially

$$
B_{123}^{II} = 2P_L(k_1)F_2^{(s)}(\boldsymbol{k}_1,\boldsymbol{k}_2)P_{13}(k_2) + (5\text{ cyc.})\,. \qquad (5.9)
$$

The other three terms need to be handled separately.

5.2 B_{222}

Neglecting the prefactor we are left with the integration

$$
\int_{\boldsymbol{q}} F_2^{(s)}(\boldsymbol{q},\boldsymbol{k}_1-\boldsymbol{q})F_2^{(s)}(-\boldsymbol{q},\boldsymbol{k}_2+\boldsymbol{q})F_2^{(s)}(\boldsymbol{k}_1-\boldsymbol{q},\boldsymbol{k}_2+\boldsymbol{q})P_L(q)P_L(|\boldsymbol{k}_1-\boldsymbol{q}|)P_L(|\boldsymbol{k}_2+\boldsymbol{q}|) \qquad (5.10)
$$

Introducing Dirac deltas to make the variables inside the power spectra tractable

$$
\int_{\boldsymbol{q}}\int_{\boldsymbol{p}}\int_{\boldsymbol{d}} F_2^{(s)}(\boldsymbol{q},\boldsymbol{p})F_2^{(s)}(-\boldsymbol{q},\boldsymbol{d})F_2^{(s)}(\boldsymbol{p},\boldsymbol{d})P_L(q)P_L(p)P_L(d)\delta^D(\boldsymbol{k}_1-\boldsymbol{q}-\boldsymbol{p})\delta^D(\boldsymbol{k}_2+\boldsymbol{q}-\boldsymbol{d}) \qquad (5.11)
$$

Now we factor the integration kernel products into their fundamental form to get the base integral

$$
\int_{\boldsymbol{q}}\int_{\boldsymbol{p}}\int_{\boldsymbol{d}} q^{n_1}p^{n_2}d^{n_3}\mathcal{L}_{\ell_1}(\mu_{q,p})\mathcal{L}_{\ell_2}(\mu_{q,d})\mathcal{L}_{\ell_3}(\mu_{p,d})P_L(q)P_L(p)P_L(d)\delta^D(\boldsymbol{k}_1-\boldsymbol{q}-\boldsymbol{p})\delta^D(\boldsymbol{k}_2+\boldsymbol{q}-\boldsymbol{d}) \qquad (5.12)
$$

5.2.1 222-Type Integral

We first expand the Dirac deltas into plane waves

$$
\begin{aligned}
&\int_{\boldsymbol{q}}\int_{\boldsymbol{p}}\int_{\boldsymbol{d}} q^{n_1}p^{n_2}d^{n_3}\mathcal{L}_{\ell_1}(\mu_{q,p})\mathcal{L}_{\ell_2}(\mu_{q,d})\mathcal{L}_{\ell_3}(\mu_{p,d})P_L(q)P_L(p)P_L(d)\\
&\left(\int_{\boldsymbol{r}} e^{i\boldsymbol{k}_1\cdot\boldsymbol{r}}e^{-i\boldsymbol{q}\cdot\boldsymbol{r}}e^{-i\boldsymbol{p}\cdot\boldsymbol{r}}\right)\left(\int_{\boldsymbol{s}} e^{i\boldsymbol{k}_2\cdot\boldsymbol{s}}e^{i\boldsymbol{q}\cdot\boldsymbol{s}}e^{-i\boldsymbol{d}\cdot\boldsymbol{s}}\right) \qquad (5.13)
\end{aligned}
$$

Then we expand the Legendre polynomials into spherical harmonics

$$\int_{\boldsymbol{q}}\int_{\boldsymbol{p}}\int_{\boldsymbol{d}}\int_{\boldsymbol{r}}\int_{\boldsymbol{s}} q^{n_1}p^{n_2}d^{n_3}P_L(q)P_L(p)P_L(d)e^{i\boldsymbol{k}_1\cdot\boldsymbol{r}}e^{-i\boldsymbol{q}\cdot\boldsymbol{r}}e^{-i\boldsymbol{p}\cdot\boldsymbol{r}}e^{i\boldsymbol{k}_2\cdot\boldsymbol{s}}e^{i\boldsymbol{q}\cdot\boldsymbol{s}}e^{-i\boldsymbol{d}\cdot\boldsymbol{s}}$$
$$\left(\frac{4\pi}{2\ell_1+1}\sum_{m_1}Y_{\ell_1m_1}(\hat{\boldsymbol{q}})Y^*_{\ell_1m_1}(\hat{\boldsymbol{p}})\right)\left(\frac{4\pi}{2\ell_2+1}\sum_{m_2}Y_{\ell_2m_2}(\hat{\boldsymbol{q}})Y^*_{\ell_2m_2}(\hat{\boldsymbol{d}})\right)\left(\frac{4\pi}{2\ell_3+1}\sum_{m_3}Y_{\ell_3m_3}(\hat{\boldsymbol{p}})Y^*_{\ell_3m_3}(\hat{\boldsymbol{d}})\right) \tag{5.14}$$

Hereafter we use the notation $\prod_x^n = (2\ell_x+1)^{n/2}$. Simplifying

$$\int_{\boldsymbol{q}}\int_{\boldsymbol{p}}\int_{\boldsymbol{d}}\int_{\boldsymbol{r}}\int_{\boldsymbol{s}}\sum_{m_1m_2m_3}(4\pi)^3\prod\nolimits_{123}^{-2}q^{n_1}p^{n_2}d^{n_3}P_L(q)P_L(p)P_L(d)$$
$$Y_{\ell_1m_1}(\hat{\boldsymbol{q}})Y^*_{\ell_1m_1}(\hat{\boldsymbol{p}})Y_{\ell_2m_2}(\hat{\boldsymbol{q}})Y^*_{\ell_2m_2}(\hat{\boldsymbol{d}})Y_{\ell_3m_3}(\hat{\boldsymbol{p}})Y^*_{\ell_3m_3}(\hat{\boldsymbol{d}})$$
$$e^{i\boldsymbol{k}_1\cdot\boldsymbol{r}}e^{-i\boldsymbol{q}\cdot\boldsymbol{r}}e^{-i\boldsymbol{p}\cdot\boldsymbol{r}}e^{i\boldsymbol{k}_2\cdot\boldsymbol{s}}e^{i\boldsymbol{q}\cdot\boldsymbol{s}}e^{-i\boldsymbol{d}\cdot\boldsymbol{s}} \tag{5.15}$$

Now expanding the exponentials into spherical harmonics

$$\int_{\boldsymbol{q}}\int_{\boldsymbol{p}}\int_{\boldsymbol{d}}\int_{\boldsymbol{r}}\int_{\boldsymbol{s}}\sum_{m_1m_2m_3}(4\pi)^3\prod\nolimits_{123}^{-2}q^{n_1}p^{n_2}d^{n_3}P_L(q)P_L(p)P_L(d)$$
$$Y_{\ell_1m_1}(\hat{\boldsymbol{q}})Y^*_{\ell_1m_1}(\hat{\boldsymbol{p}})Y_{\ell_2m_2}(\hat{\boldsymbol{q}})Y^*_{\ell_2m_2}(\hat{\boldsymbol{d}})Y_{\ell_3m_3}(\hat{\boldsymbol{p}})Y^*_{\ell_3m_3}(\hat{\boldsymbol{d}})$$
$$\left(4\pi\sum_{\ell_{kr}m_{kr}}i^{\ell_{kr}}j_{\ell_{kr}}(k_1r)Y_{\ell_{kr}m_{kr}}(\hat{\boldsymbol{r}})Y^*_{\ell_{kr}m_{kr}}(\hat{\boldsymbol{k}}_1)\right)\left(4\pi\sum_{\ell_{qr}m_{qr}}i^{-\ell_{qr}}j_{\ell_{qr}}(qr)Y_{\ell_{qr}m_{qr}}(\hat{\boldsymbol{q}})Y^*_{\ell_{qr}m_{qr}}(\hat{\boldsymbol{r}})\right)$$
$$\left(4\pi\sum_{\ell_{pr}m_{pr}}i^{-\ell_{pr}}j_{\ell_{pr}}(pr)Y_{\ell_{pr}m_{pr}}(\hat{\boldsymbol{p}})Y^*_{\ell_{pr}m_{pr}}(\hat{\boldsymbol{r}})\right)\left(4\pi\sum_{\ell_{ks}m_{ks}}i^{\ell_{ks}}j_{\ell_{ks}}(k_2s)Y_{\ell_{ks}m_{ks}}(\hat{\boldsymbol{s}})Y^*_{\ell_{ks}m_{ks}}(\hat{\boldsymbol{k}}_2)\right)$$
$$\left(4\pi\sum_{\ell_{qs}m_{qs}}i^{\ell_{qs}}j_{\ell_{qs}}(qs)Y_{\ell_{qs}m_{qs}}(\hat{\boldsymbol{q}})Y^*_{\ell_{qs}m_{qs}}(\hat{\boldsymbol{s}})\right)\left(4\pi\sum_{\ell_{ds}m_{ds}}i^{-\ell_{ds}}j_{\ell_{ds}}(ds)Y_{\ell_{ds}m_{ds}}(\hat{\boldsymbol{d}})Y^*_{\ell_{ds}m_{ds}}(\hat{\boldsymbol{s}})\right) \tag{5.16}$$

Simplifying

$$\int_{\boldsymbol{qpdrs}}\sum_{\ell_{kr}\ell_{qr}\ell_{pr}\ell_{ks}\ell_{qs}\ell_{ds}}\sum_{m_1m_2m_3m_{kr}m_{qr}m_{pr}m_{ks}m_{qs}m_{ds}}(4\pi)^9\prod\nolimits_{123}^{-2}i^{\ell_{kr}-\ell_{qr}-\ell_{pr}+\ell_{ks}+\ell_{qs}-\ell_{ds}}$$
$$q^{n_1}p^{n_2}d^{n_3}P_L(q)P_L(p)P_L(d)j_{\ell_{kr}}(k_1r)j_{\ell_{qr}}(qr)j_{\ell_{pr}}(pr)j_{\ell_{ks}}(k_2s)j_{\ell_{qs}}(qs)j_{\ell_{ds}}(ds)$$
$$Y_{\ell_1m_1}(\hat{\boldsymbol{q}})Y^*_{\ell_1m_1}(\hat{\boldsymbol{p}})Y_{\ell_2m_2}(\hat{\boldsymbol{q}})Y^*_{\ell_2m_2}(\hat{\boldsymbol{d}})Y_{\ell_3m_3}(\hat{\boldsymbol{p}})Y^*_{\ell_3m_3}(\hat{\boldsymbol{d}})Y_{\ell_{kr}m_{kr}}(\hat{\boldsymbol{r}})Y^*_{\ell_{kr}m_{kr}}(\hat{\boldsymbol{k}}_1)Y_{\ell_{qr}m_{qr}}(\hat{\boldsymbol{q}})Y^*_{\ell_{qr}m_{qr}}(\hat{\boldsymbol{r}})$$
$$Y_{\ell_{pr}m_{pr}}(\hat{\boldsymbol{p}})Y^*_{\ell_{pr}m_{pr}}(\hat{\boldsymbol{r}})Y_{\ell_{ks}m_{ks}}(\hat{\boldsymbol{s}})Y^*_{\ell_{ks}m_{ks}}(\hat{\boldsymbol{k}}_2)Y_{\ell_{qs}m_{qs}}(\hat{\boldsymbol{q}})Y^*_{\ell_{qs}m_{qs}}(\hat{\boldsymbol{s}})Y_{\ell_{ds}m_{ds}}(\hat{\boldsymbol{d}})Y^*_{\ell_{ds}m_{ds}}(\hat{\boldsymbol{s}}) \tag{5.17}$$

We can factor each angular integral separately

$$\int_{qpdrs} \sum_{\ell_{kr}\ell_{qr}\ell_{pr}\ell_{ks}\ell_{qs}\ell_{ds}} \sum_{m_1m_2m_3m_{kr}m_{qr}m_{pr}m_{ks}m_{qs}m_{ds}} (4\pi)^9 \prod_{123}^{-2} i^{\ell_{kr}-\ell_{qr}-\ell_{pr}+\ell_{ks}+\ell_{qs}-\ell_{ds}}$$
$$q^{n_1}p^{n_2}d^{n_3}P_L(q)P_L(p)P_L(d)j_{\ell_{kr}}(k_1r)j_{\ell_{qr}}(qr)j_{\ell_{pr}}(pr)j_{\ell_{ks}}(k_2s)j_{\ell_{qs}}(qs)j_{\ell_{ds}}(ds)$$
$$\left(\int_{\hat{\boldsymbol{q}}} Y_{\ell_1m_1}(\hat{\boldsymbol{q}})Y_{\ell_2m_2}(\hat{\boldsymbol{q}})Y_{\ell_{qr}m_{qr}}(\hat{\boldsymbol{q}})Y_{\ell_{qs}m_{qs}}(\hat{\boldsymbol{q}})\right)$$
$$\left(\int_{\hat{\boldsymbol{p}}} Y^*_{\ell_1m_1}(\hat{\boldsymbol{p}})Y_{\ell_3m_3}(\hat{\boldsymbol{p}})Y_{\ell_{pr}m_{pr}}(\hat{\boldsymbol{p}})\right)\left(\int_{\hat{\boldsymbol{d}}} Y^*_{\ell_2m_2}(\hat{\boldsymbol{d}})Y^*_{\ell_3m_3}(\hat{\boldsymbol{d}})Y_{\ell_{ds}m_{ds}}(\hat{\boldsymbol{d}})\right)$$
$$\left(\int_{\hat{\boldsymbol{r}}} Y_{\ell_{kr}m_{kr}}(\hat{\boldsymbol{r}})Y^*_{\ell_{qr}m_{qr}}(\hat{\boldsymbol{r}})Y^*_{\ell_{pr}m_{pr}}(\hat{\boldsymbol{r}})\right)\left(\int_{\hat{\boldsymbol{s}}} Y_{\ell_{ks}m_{ks}}(\hat{\boldsymbol{s}})Y^*_{\ell_{qs}m_{qs}}(\hat{\boldsymbol{s}})Y^*_{\ell_{ds}m_{ds}}(\hat{\boldsymbol{s}})\right) Y^*_{\ell_{kr}m_{kr}}(\hat{\boldsymbol{k}}_1)Y^*_{\ell_{ks}m_{ks}}(\hat{\boldsymbol{k}}_2) \tag{5.18}$$

The angular integrals with only three spherical harmonics can be done straightforwardly with the gaunt integral Eq. (A.5)

$$\int_{qpdrs} \sum_{\ell_{kr}\ell_{qr}\ell_{pr}\ell_{ks}\ell_{qs}\ell_{ds}} \sum_{m_1m_2m_3m_{kr}m_{qr}m_{pr}m_{ks}m_{qs}m_{ds}} (4\pi)^9 \prod_{123}^{-2} i^{\ell_{kr}-\ell_{qr}-\ell_{pr}+\ell_{ks}+\ell_{qs}-\ell_{ds}}$$
$$q^{n_1}p^{n_2}d^{n_3}P_L(q)P_L(p)P_L(d)j_{\ell_{kr}}(k_1r)j_{\ell_{qr}}(qr)j_{\ell_{pr}}(pr)j_{\ell_{ks}}(k_2s)j_{\ell_{qs}}(qs)j_{\ell_{ds}}(ds)$$
$$\left(\int_{\hat{\boldsymbol{q}}} Y_{\ell_1m_1}(\hat{\boldsymbol{q}})Y_{\ell_2m_2}(\hat{\boldsymbol{q}})Y_{\ell_{qr}m_{qr}}(\hat{\boldsymbol{q}})Y_{\ell_{qs}m_{qs}}(\hat{\boldsymbol{q}})\right)(-1)^{m_1}\mathcal{G}^{-m_1,m_3,m_{pr}}_{\ell_1\ell_3\ell_{pr}}(-1)^{m_2+m_3}\mathcal{G}^{-m_2,-m_3,m_{ds}}_{\ell_2\ell_3\ell_{ds}}$$
$$(-1)^{m_{qr}+m_{pr}}\mathcal{G}^{m_{kr},-m_{qr},-m_{pr}}_{\ell_{kr}\ell_{qr}\ell_{pr}}(-1)^{m_{qs}+m_{ds}}\mathcal{G}^{m_{ks},-m_{qs},-m_{ds}}_{\ell_{ks}\ell_{qs}\ell_{ds}}Y^*_{\ell_{kr}m_{kr}}(\hat{\boldsymbol{k}}_1)Y^*_{\ell_{ks}m_{ks}}(\hat{\boldsymbol{k}}_2) \tag{5.19}$$

We can now set our coordinate system such that $\boldsymbol{k}_1$ is entirely in the z direction while $\boldsymbol{k}_2$ is on the $z-x$ plane. This gives the simplification

$$Y^*_{\ell_{kr}m_{kr}}(\hat{\boldsymbol{k}}_1) = \sqrt{\frac{2\ell_{kr}+1}{4\pi}}\delta_{m_{kr},0} \tag{5.20}$$

Which when applied to the previous expression leads to

$$\int_{qpdrs} \sum_{\ell_{kr}\ell_{qr}\ell_{pr}\ell_{ks}\ell_{qs}\ell_{ds}} \sum_{m_1m_2m_3m_{qr}m_{pr}m_{ks}m_{qs}m_{ds}} (4\pi)^{8.5} \prod_{123}^{-2}\prod_{(kr)} i^{\ell_{kr}-\ell_{qr}-\ell_{pr}+\ell_{ks}+\ell_{qs}-\ell_{ds}}$$
$$q^{n_1}p^{n_2}d^{n_3}P_L(q)P_L(p)P_L(d)j_{\ell_{kr}}(k_1r)j_{\ell_{qr}}(qr)j_{\ell_{pr}}(pr)j_{\ell_{ks}}(k_2s)j_{\ell_{qs}}(qs)j_{\ell_{ds}}(ds)$$
$$\left(\int_{\hat{\boldsymbol{q}}} Y_{\ell_1m_1}(\hat{\boldsymbol{q}})Y_{\ell_2m_2}(\hat{\boldsymbol{q}})Y_{\ell_{qr}m_{qr}}(\hat{\boldsymbol{q}})Y_{\ell_{qs}m_{qs}}(\hat{\boldsymbol{q}})\right)(-1)^{m_1}\mathcal{G}^{-m_1,m_3,m_{pr}}_{\ell_1\ell_3\ell_{pr}}(-1)^{m_2+m_3}\mathcal{G}^{-m_2,-m_3,m_{ds}}_{\ell_2\ell_3\ell_{ds}}$$
$$(-1)^{m_{qr}+m_{pr}}\mathcal{G}^{0,m_{qr},m_{pr}}_{\ell_{kr}\ell_{qr}\ell_{pr}}(-1)^{m_{qs}+m_{ds}}\mathcal{G}^{m_{ks},-m_{qs},-m_{ds}}_{\ell_{ks}\ell_{qs}\ell_{ds}}Y^*_{\ell_{ks}m_{ks}}(\hat{\boldsymbol{k}}_2) \tag{5.21}$$

Where we have used the fact that the signs of the m's in a Gaunt integral (the third one) can all change signs for free. The 0 in the third Gaunt integral enforces the condition $m_{pr} = -m_{qr}$ which we apply

$$\int_{qpdrs} \sum_{\ell_{kr}\ell_{qr}\ell_{pr}\ell_{ks}\ell_{qs}\ell_{ds}} \sum_{m_1 m_2 m_3 m_{qr} m_{ks} m_{qs} m_{ds}} (4\pi)^{8.5} \prod_{123}^{-2} \prod_{(kr)} i^{\ell_{kr}-\ell_{qr}-\ell_{pr}+\ell_{ks}+\ell_{qs}-\ell_{ds}}$$
$$q^{n_1} p^{n_2} d^{n_3} P_L(q) P_L(p) P_L(d) j_{\ell_{kr}}(k_1 r) j_{\ell_{qr}}(qr) j_{\ell_{pr}}(pr) j_{\ell_{ks}}(k_2 s) j_{\ell_{qs}}(qs) j_{\ell_{ds}}(ds)$$
$$\left(\int_{\hat{\boldsymbol{q}}} Y_{\ell_1 m_1}(\hat{\boldsymbol{q}}) Y_{\ell_2 m_2}(\hat{\boldsymbol{q}}) Y_{\ell_{qr} m_{qr}}(\hat{\boldsymbol{q}}) Y_{\ell_{qs} m_{qs}}(\hat{\boldsymbol{q}}) \right) (-1)^{m_1} \mathcal{G}^{-m_1, m_3, -m_{qr}}_{\ell_1 \ell_3 \ell_{pr}} (-1)^{m_2+m_3} \mathcal{G}^{-m_2, -m_3, m_{ds}}_{\ell_2 \ell_3 \ell_{ds}}$$
$$\mathcal{G}^{0, m_{qr}, -m_{qr}}_{\ell_{kr}\ell_{qr}\ell_{pr}} (-1)^{m_{qs}+m_{ds}} \mathcal{G}^{m_{ks}, -m_{qs}, -m_{ds}}_{\ell_{ks}\ell_{qs}\ell_{ds}} Y^*_{\ell_{ks} m_{ks}}(\hat{\boldsymbol{k}}_2) \tag{5.22}$$

We will now perform the q angular integral using the extended Gaunt integral

$$\int_{\hat{\boldsymbol{q}}} Y_{\ell_1 m_1}(\hat{\boldsymbol{q}}) Y_{\ell_2 m_2}(\hat{\boldsymbol{q}}) Y_{\ell_{qr} m_{qr}}(\hat{\boldsymbol{q}}) Y_{\ell_{qs} m_{qs}}(\hat{\boldsymbol{q}}) = \sum_{L_q} (-1)^{M_q} \mathcal{G}^{m_1, m_2, -M_q}_{\ell_1 \ell_2 L_q} \mathcal{G}^{M_q, m_{qr}, m_{qs}}_{L_q \ell_{qr} \ell_{qs}} \tag{5.23}$$

Note that M_q is defined by both $M_q = m_1 + m_2$ and $M_q = -m_{qr} - m_{qs}$ as is required by the 3j symbols. We introduce a sum over M_q to simplify further work. Combining this with the previous expression

$$\int_{qpdrs} \sum_{\ell_{kr}\ell_{qr}\ell_{pr}\ell_{ks}\ell_{qs}\ell_{ds}L_q} \sum_{m_1 m_2 m_3 m_{qr} m_{ks} m_{qs} m_{ds} M_q} (4\pi)^{8.5} \prod_{123}^{-2} \prod_{(kr)} i^{\ell_{kr}-\ell_{qr}-\ell_{pr}+\ell_{ks}+\ell_{qs}-\ell_{ds}}$$
$$q^{n_1} p^{n_2} d^{n_3} P_L(q) P_L(p) P_L(d) j_{\ell_{kr}}(k_1 r) j_{\ell_{qr}}(qr) j_{\ell_{pr}}(pr) j_{\ell_{ks}}(k_2 s) j_{\ell_{qs}}(qs) j_{\ell_{ds}}(ds) (-1)^{m_3+m_{qs}+m_{ds}}$$
$$\mathcal{G}^{m_1, m_2, -M_q}_{\ell_1 \ell_2 L_q} \mathcal{G}^{M_q, m_{qr}, m_{qs}}_{L_q \ell_{qr} \ell_{qs}} \mathcal{G}^{-m_1, m_3, -m_{qr}}_{\ell_1 \ell_3 \ell_{pr}} \mathcal{G}^{-m_2, -m_3, m_{ds}}_{\ell_2 \ell_3 \ell_{ds}} \mathcal{G}^{0, m_{qr}, -m_{qr}}_{\ell_{kr}\ell_{qr}\ell_{pr}} \mathcal{G}^{m_{ks}, -m_{qs}, -m_{ds}}_{\ell_{ks}\ell_{qs}\ell_{ds}} Y^*_{\ell_{ks} m_{ks}}(\hat{\boldsymbol{k}}_2) \tag{5.24}$$

Looking at some of the m equations we have $m_1 + m_2 = -m_{qr} - m_{qs}$ (First 2 G). We also have $m_{qr} = m_3 - m_1$ (3rd G), plugging in: $m_2 + m_3 = -m_{qs}$. Then we have $m_{ds} = m_2 + m_3$ (4th G) which means $m_{ds} = -m_{qs}$. Plugging this in

$$\int_{qpdrs} \sum_{\ell_{kr}\ell_{qr}\ell_{pr}\ell_{ks}\ell_{qs}\ell_{ds}L_q} \sum_{m_1 m_2 m_3 m_{qr} m_{ks} m_{qs} M_q} (4\pi)^{8.5} \prod_{123}^{-2} \prod_{(kr)} i^{\ell_{kr}-\ell_{qr}-\ell_{pr}+\ell_{ks}+\ell_{qs}-\ell_{ds}}$$
$$q^{n_1} p^{n_2} d^{n_3} P_L(q) P_L(p) P_L(d) j_{\ell_{kr}}(k_1 r) j_{\ell_{qr}}(qr) j_{\ell_{pr}}(pr) j_{\ell_{ks}}(k_2 s) j_{\ell_{qs}}(qs) j_{\ell_{ds}}(ds) (-1)^{m_3}$$
$$\mathcal{G}^{m_1, m_2, -M_q}_{\ell_1 \ell_2 L_q} \mathcal{G}^{M_q, m_{qr}, m_{qs}}_{L_q \ell_{qr} \ell_{qs}} \mathcal{G}^{-m_1, m_3, -m_{qr}}_{\ell_1 \ell_3 \ell_{pr}} \mathcal{G}^{-m_2, -m_3, -m_{qs}}_{\ell_2 \ell_3 \ell_{ds}} \mathcal{G}^{0, m_{qr}, -m_{qr}}_{\ell_{kr}\ell_{qr}\ell_{pr}} \mathcal{G}^{m_{ks}, -m_{qs}, m_{qs}}_{\ell_{ks}\ell_{qs}\ell_{ds}} Y^*_{\ell_{ks} m_{ks}}(\hat{\boldsymbol{k}}_2) \tag{5.25}$$

Now the sixth Gaunt integral implies that $m_{ks} = 0$. Applying that

$$\int_{qpdrs} \sum_{\ell_{kr}\ell_{qr}\ell_{pr}\ell_{ks}\ell_{qs}\ell_{ds}L_q} \sum_{m_1 m_2 m_3 m_{qr} m_{qs} M_q} (4\pi)^8 \prod\nolimits_{123}^{-2} \prod_{(kr)(ks)} i^{\ell_{kr}-\ell_{qr}-\ell_{pr}+\ell_{ks}+\ell_{qs}-\ell_{ds}}$$
$$q^{n_1} p^{n_2} d^{n_3} P_L(q) P_L(p) P_L(d) j_{\ell_{kr}}(k_1 r) j_{\ell_{qr}}(qr) j_{\ell_{pr}}(pr) j_{\ell_{ks}}(k_2 s) j_{\ell_{qs}}(qs) j_{\ell_{ds}}(ds) (-1)^{m_3}$$
$$\mathcal{G}^{m_1,m_2,-M_q}_{\ell_1\ell_2 L_q} \mathcal{G}^{M_q,m_{qr},m_{qs}}_{L_q\ell_{qr}\ell_{qs}} \mathcal{G}^{-m_1,m_3,-m_{qr}}_{\ell_1\ell_3\ell_{pr}} \mathcal{G}^{-m_2,-m_3,-m_{qs}}_{\ell_2\ell_3\ell_{ds}} \mathcal{G}^{0,m_{qr},-m_{qr}}_{\ell_{kr}\ell_{qr}\ell_{pr}} \mathcal{G}^{0,-m_{qs},m_{qs}}_{\ell_{ks}\ell_{qs}\ell_{ds}} \mathcal{L}_{\ell_{ks}}(\boldsymbol{k}_1 \cdot \boldsymbol{k}_2) \tag{5.26}$$

Where we have used

$$Y_{\ell_{ks}0}(\hat{\boldsymbol{k}}_2) = \sqrt{\frac{2\ell_{ks}+1}{4\pi}} \mathcal{L}_{\ell_{ks}}(\cos\theta_{\hat{\boldsymbol{k}}_2}) \tag{5.27}$$

We also use that $\cos\theta_{\hat{\boldsymbol{k}}_2} = \boldsymbol{k}_1 \cdot \boldsymbol{k}_2 = \frac{k_1^2+k_2^2-k_3^2}{2k_1k_2}$ (This arises from the law of cosines applied to the wavenumber triangle)

$$\begin{aligned}
&(-1)^{M_q}(4\pi)^{3/2} \sum_{m_1 m_2 m_3} (-1)^{m_3+m_1+m_2} \mathcal{G}^{m_{qr},m_1,-m_3}_{\ell_{pr}\ell_1\ell_3} \mathcal{G}^{m_{qs},m_2,m_3}_{\ell_{ds}\ell_2\ell_3} \mathcal{G}^{M_q,-m_1,-m_2}_{L_q\ell_1\ell_2} \\
&= (-1)^{M_q} \prod\nolimits_{123}^{2} \prod_{(pr)(ds)L_q} \begin{pmatrix} \ell_{pr} & \ell_1 & \ell_3 \\ 0 & 0 & 0 \end{pmatrix} \begin{pmatrix} \ell_{ds} & \ell_2 & \ell_3 \\ 0 & 0 & 0 \end{pmatrix} \begin{pmatrix} L_q & \ell_1 & \ell_2 \\ 0 & 0 & 0 \end{pmatrix} \\
&\times (-1)^{\ell_1+\ell_2+\ell_3} \begin{Bmatrix} \ell_{pr} & \ell_{ds} & L_q \\ \ell_2 & \ell_1 & \ell_3 \end{Bmatrix} \begin{pmatrix} \ell_{pr} & \ell_{ds} & L_q \\ m_{qr} & m_{qs} & M_q \end{pmatrix}
\end{aligned} \tag{5.28}$$

Where we have used that $m_1 + m_2 - M_q = 0$ to induce a factor $(-1)^{m_1+m_2-M_q}$. We used Eq. (C.12) in exact order above. Applying this to the original expression

$$\int_{qpdrs} \sum_{\ell_{kr}\ell_{qr}\ell_{pr}\ell_{ks}\ell_{qs}\ell_{ds}L_q} \sum_{m_{qr}m_{qs}M_q} (4\pi)^{6.5} \prod_{(kr)(ks)(pr)(ds)L_q} (-1)^{\ell_1+\ell_2+\ell_3} i^{\ell_{kr}-\ell_{qr}-\ell_{pr}+\ell_{ks}+\ell_{qs}-\ell_{ds}}$$
$$q^{n_1} p^{n_2} d^{n_3} P_L(q) P_L(p) P_L(d) j_{\ell_{kr}}(k_1 r) j_{\ell_{qr}}(qr) j_{\ell_{pr}}(pr) j_{\ell_{ks}}(k_2 s) j_{\ell_{qs}}(qs) j_{\ell_{ds}}(ds) \mathcal{L}_{\ell_{ks}}(\boldsymbol{k}_1 \cdot \boldsymbol{k}_2) (-1)^{M_q}$$
$$\begin{pmatrix} \ell_{pr} & \ell_1 & \ell_3 \\ 0 & 0 & 0 \end{pmatrix} \begin{pmatrix} \ell_{ds} & \ell_2 & \ell_3 \\ 0 & 0 & 0 \end{pmatrix} \begin{pmatrix} L_q & \ell_1 & \ell_2 \\ 0 & 0 & 0 \end{pmatrix} \mathcal{G}^{M_q,m_{qr},m_{qs}}_{L_q\ell_{qr}\ell_{qs}} \mathcal{G}^{0,m_{qr},-m_{qr}}_{\ell_{kr}\ell_{qr}\ell_{pr}} \mathcal{G}^{0,-m_{qs},m_{qs}}_{\ell_{ks}\ell_{qs}\ell_{ds}}$$
$$\begin{pmatrix} \ell_{pr} & \ell_{ds} & L_q \\ m_{qr} & m_{qs} & M_q \end{pmatrix} \begin{Bmatrix} \ell_{pr} & \ell_{ds} & L_q \\ \ell_2 & \ell_1 & \ell_3 \end{Bmatrix} \tag{5.29}$$

We reintroduce m_{pr} along with a sum over it to simplify notation.

$$(4\pi) \sum_{M_q m_{qr} m_{pr}} (-1)^{M_q+m_{qr}+m_{pr}} \begin{pmatrix} \ell_{ds} & L_q & \ell_{pr} \\ m_{qs} & M_q & -m_{pr} \end{pmatrix} \mathcal{G}^{0,m_{qr},m_{pr}}_{\ell_{kr}\ell_{qr}\ell_{pr}} \mathcal{G}^{-m_{qs},-M_q,-m_{qr}}_{\ell_{qs}L_q\ell_{qr}}$$

$$= \prod_{(qr)}^{2} \prod_{(kr)(pr)(qs)L_q} \begin{pmatrix} \ell_{kr} & \ell_{qr} & \ell_{pr} \\ 0 & 0 & 0 \end{pmatrix} \begin{pmatrix} \ell_{qs} & L_q & \ell_{qr} \\ 0 & 0 & 0 \end{pmatrix}$$
$$\times (-1)^{\ell_{pr}+L_q+\ell_{qr}} \begin{pmatrix} \ell_{ds} & \ell_{kr} & \ell_{qs} \\ m_{qs} & 0 & -m_{qs} \end{pmatrix} \begin{Bmatrix} \ell_{ds} & \ell_{kr} & \ell_{qs} \\ \ell_{qr} & L_q & \ell_{pr} \end{Bmatrix} \tag{5.30}$$

Where we have induced a factor $(-1)^{m_{qr}+m_{pr}}$ since it is trivially 1. We again use Eq. (C.12) in exact order (with a 3-j instead of a Gaunt integral). Returning to the original expression

$$\int_{qpdrs} \sum_{\ell_{kr}\ell_{qr}\ell_{pr}\ell_{ks}\ell_{qs}\ell_{ds}L_q} \sum_{m_{qs}} (4\pi)^5 \prod_{(qr)(kr)(pr)(ks)(ds)(qs)L_q}^{2} (-1)^{\ell_1+\ell_{qr}} i^{\ell_{kr}-\ell_{qr}-\ell_{pr}+\ell_{ks}+\ell_{qs}-\ell_{ds}}$$
$$q^{n_1} p^{n_2} d^{n_3} P_L(q) P_L(p) P_L(d) j_{\ell_{kr}}(k_1 r) j_{\ell_{qr}}(qr) j_{\ell_{pr}}(pr) j_{\ell_{ks}}(k_2 s) j_{\ell_{qs}}(qs) j_{\ell_{ds}}(ds) \mathcal{L}_{\ell_{ks}}(\boldsymbol{k}_1 \cdot \boldsymbol{k}_2)$$
$$\begin{pmatrix} \ell_{pr} & \ell_1 & \ell_3 \\ 0 & 0 & 0 \end{pmatrix} \begin{pmatrix} \ell_{ds} & \ell_2 & \ell_3 \\ 0 & 0 & 0 \end{pmatrix} \begin{pmatrix} L_q & \ell_1 & \ell_2 \\ 0 & 0 & 0 \end{pmatrix} \begin{pmatrix} \ell_{kr} & \ell_{qr} & \ell_{pr} \\ 0 & 0 & 0 \end{pmatrix} \begin{pmatrix} \ell_{qs} & L_q & \ell_{qr} \\ 0 & 0 & 0 \end{pmatrix} \begin{pmatrix} \ell_{ks} & \ell_{qs} & \ell_{ds} \\ 0 & 0 & 0 \end{pmatrix}$$
$$\begin{pmatrix} \ell_{ks} & \ell_{qs} & \ell_{ds} \\ 0 & -m_{qs} & m_{qs} \end{pmatrix} \begin{pmatrix} \ell_{ds} & \ell_{kr} & \ell_{qs} \\ m_{qs} & 0 & -m_{qs} \end{pmatrix} \begin{Bmatrix} \ell_{ds} & \ell_{kr} & \ell_{qs} \\ \ell_{qr} & L_q & \ell_{pr} \end{Bmatrix} \begin{Bmatrix} \ell_{pr} & \ell_{ds} & L_q \\ \ell_2 & \ell_1 & \ell_3 \end{Bmatrix} \tag{5.31}$$

Here we have reduced some factors in the -1 by absorbing them into zero m 3-j symbols and expanded the final Gaunt integral. We can now use 3-j orthogonality

$$\sum_{m_{qs}} \begin{pmatrix} \ell_{qs} & \ell_{ds} & \ell_{ks} \\ -m_{qs} & m_{qs} & 0 \end{pmatrix} \begin{pmatrix} \ell_{qs} & \ell_{ds} & \ell_{kr} \\ -m_{qs} & m_{qs} & 0 \end{pmatrix} = \delta_{\ell_{ks},\ell_{kr}} \prod_{(ks)}^{-2} \tag{5.32}$$

Plugging this in

$$\int_{qpdrs} \sum_{\ell_{kr}\ell_{qr}\ell_{pr}\ell_{qs}\ell_{ds}L_q} (4\pi)^5 \prod_{(qr)(kr)(pr)(ds)(qs)L_q}^{2} (-1)^{\ell_1+\ell_{qr}} i^{2\ell_{kr}-\ell_{qr}-\ell_{pr}+\ell_{qs}-\ell_{ds}}$$
$$q^{n_1} p^{n_2} d^{n_3} P_L(q) P_L(p) P_L(d) j_{\ell_{kr}}(k_1 r) j_{\ell_{qr}}(qr) j_{\ell_{pr}}(pr) j_{\ell_{kr}}(k_2 s) j_{\ell_{qs}}(qs) j_{\ell_{ds}}(ds) \mathcal{L}_{\ell_{kr}}(\boldsymbol{k}_1 \cdot \boldsymbol{k}_2)$$
$$\begin{pmatrix} \ell_{pr} & \ell_1 & \ell_3 \\ 0 & 0 & 0 \end{pmatrix} \begin{pmatrix} \ell_{ds} & \ell_2 & \ell_3 \\ 0 & 0 & 0 \end{pmatrix} \begin{pmatrix} L_q & \ell_1 & \ell_2 \\ 0 & 0 & 0 \end{pmatrix} \begin{pmatrix} \ell_{kr} & \ell_{qr} & \ell_{pr} \\ 0 & 0 & 0 \end{pmatrix}$$
$$\begin{pmatrix} \ell_{qs} & L_q & \ell_{qr} \\ 0 & 0 & 0 \end{pmatrix} \begin{pmatrix} \ell_{kr} & \ell_{qs} & \ell_{ds} \\ 0 & 0 & 0 \end{pmatrix} \begin{Bmatrix} \ell_{qs} & \ell_{qr} & L_q \\ \ell_{pr} & \ell_{ds} & \ell_{kr} \end{Bmatrix} \begin{Bmatrix} \ell_2 & \ell_1 & L_q \\ \ell_{pr} & \ell_{ds} & \ell_3 \end{Bmatrix} \tag{5.33}$$

Writing the final expression in terms of FFTLog functions

$$\sum_{\ell_{kr}\ell_{qr}\ell_{pr}\ell_{qs}\ell_{ds}L_q} (4\pi)^5 \prod_{(qr)(kr)(pr)(ds)(qs)L_q}^{2} (-1)^{\ell_1+\ell_{qr}} i^{2\ell_{kr}-\ell_{qr}-\ell_{pr}+\ell_{qs}-\ell_{ds}} \mathcal{L}_{\ell_{kr}}(\boldsymbol{k}_1 \cdot \boldsymbol{k}_2)$$
$$\mathcal{B}^{(222),n_1 n_2 n_3}_{\ell_{kr}\ell_{kr}\ell_{qr}\ell_{qs}\ell_{pr}\ell_{ds}}(k_1, k_2)$$

$$\begin{pmatrix} \ell_{pr} & \ell_1 & \ell_3 \\ 0 & 0 & 0 \end{pmatrix} \begin{pmatrix} \ell_{ds} & \ell_2 & \ell_3 \\ 0 & 0 & 0 \end{pmatrix} \begin{pmatrix} L_q & \ell_1 & \ell_2 \\ 0 & 0 & 0 \end{pmatrix} \begin{pmatrix} \ell_{kr} & \ell_{qr} & \ell_{pr} \\ 0 & 0 & 0 \end{pmatrix}$$
$$\begin{pmatrix} \ell_{qs} & L_q & \ell_{qr} \\ 0 & 0 & 0 \end{pmatrix} \begin{pmatrix} \ell_{kr} & \ell_{qs} & \ell_{ds} \\ 0 & 0 & 0 \end{pmatrix} \begin{Bmatrix} \ell_{qs} & \ell_{qr} & L_q \\ \ell_{pr} & \ell_{ds} & \ell_{kr} \end{Bmatrix} \begin{Bmatrix} \ell_2 & \ell_1 & L_q \\ \ell_{pr} & \ell_{ds} & \ell_3 \end{Bmatrix} \tag{5.34}$$

Where we define the final 2d FFTLog transformation

$$\mathcal{B}^{(222),n_1n_2n_3}_{\ell_{kr}\ell_{kr}\ell_{qr}\ell_{qs}\ell_{pr}\ell_{ds}}(k_1,k_2) = \int_{rs} j_{\ell_{kr}}(k_1 r) j_{\ell_{kr}}(k_2 s) \Xi^{n_1}_{\ell_{qr}\ell_{qs}}(r,s) \xi^{n_2}_{\ell_{pr}}(r) \xi^{n_3}_{\ell_{ds}}(s) \tag{5.35}$$

Note that while this looks like many infinite sums, when applying the restrictions imposed by the Wigner symbols only one sum can remain unbound. Specifically given $\ell_{123} = 2$ (max value) then the max for $\ell_{pr} = \ell_{ds} = L_q = 4$ this tells us that $|\ell_{kr} - \ell_{qr}| = |\ell_{kr} - \ell_{qs}| = |\ell_{qr} - \ell_{qs}| = 4$ is the max difference. This does not place a maximum on them but it does effectively reduce this to only a single infinite sum (since the other two must be clustered around the other.) Since the total sum must be even this allows (say we perform the infinite sum over ℓ_{kr}) ℓ_{qr} to be $\ell_{kr} \pm 4$, $\ell_{kr} \pm 2$ and ℓ_{kr}. ℓ_{qs} suffers an even harsher restriction, bounded by both other l's, for a maximum of 5 values (when $\ell_{qr} = \ell_{kr}$). Other non-maximal cases of the given l's or the bounded l's will result in even tighter windows. Testing the sum reveals that for most configurations it converges very quickly (1% within 10-20 terms) and those configurations where it converges worse are themselves smaller contributions to the final result.

5.3 B_{123}

Neglecting the prefactor and cyclic terms we are left with the integration

$$\int_{\boldsymbol{q}} F_2^{(s)}(\boldsymbol{q}, \boldsymbol{k}_2 - \boldsymbol{q}) F_3^{(s)}(\boldsymbol{q}, \boldsymbol{k}_2 - \boldsymbol{q}, \boldsymbol{k}_1) P_L(q) P_L(|\boldsymbol{k}_2 - \boldsymbol{q}|) \tag{5.36}$$

Introducing dirac deltas to make the variables inside the power spectra tractable

$$\int_{\boldsymbol{q}} \int_{\boldsymbol{p}} F_2^{(s)}(\boldsymbol{q}, \boldsymbol{p}) F_3^{(s)}(\boldsymbol{q}, \boldsymbol{p}, \boldsymbol{k}_1) P_L(q) P_L(p) \delta^D(\boldsymbol{k}_2 - \boldsymbol{q} - \boldsymbol{p}) \tag{5.37}$$

Expanding this results in the fundamental integral

$$\int_{\boldsymbol{q}} \int_{\boldsymbol{p}} \frac{1}{|\boldsymbol{k}_1 + \boldsymbol{q}|^{2b_1} |\boldsymbol{k}_1 + \boldsymbol{p}|^{2b_2}} q^{n_1} p^{n_2} \mathcal{L}_{\ell_1}(\mu_{q,p}) \mathcal{L}_{\ell_2}(\mu_{q,k_1}) \mathcal{L}_{\ell_3}(\mu_{p,k_1}) P_L(q) P_L(p) \delta^D(\boldsymbol{k}_2 - \boldsymbol{q} - \boldsymbol{p}) \tag{5.38}$$

Where only a single denominator term occurs at once. Since the integral is symmetric about q and p we only need to consider one of the denominators. We can factor the symmetric kernel (with only one possible denominator) such that the denominator appears in every term, leaving us with just a single integral to solve.

$$\int_{\boldsymbol{q}}\int_{\boldsymbol{p}} \frac{q^{n_1}p^{n_2}}{|\boldsymbol{k}_1+\boldsymbol{q}|^2}\mathcal{L}_{\ell_1}(\mu_{q,k_1})\mathcal{L}_{\ell_2}(\mu_{p,k_1})\mathcal{L}_{\ell_3}(\mu_{q,p})P_L(q)P_L(p)\delta^D(\boldsymbol{k}_2-\boldsymbol{q}-\boldsymbol{p}) \tag{5.39}$$

5.3.1 123-Type Integral

We can introduce a dirac delta to reduce the denominator to a simpler form

$$\int_{\boldsymbol{q}}\int_{\boldsymbol{p}}\int_{\boldsymbol{d}} q^{n_1}p^{n_2}d^{-2}\mathcal{L}_{\ell_1}(\mu_{q,k_1})\mathcal{L}_{\ell_2}(\mu_{p,k_1})\mathcal{L}_{\ell_3}(\mu_{q,p})P_L(q)P_L(p)\delta^D(\boldsymbol{k}_2-\boldsymbol{q}-\boldsymbol{p})\delta^D(\boldsymbol{k}_1+\boldsymbol{q}-\boldsymbol{d}) \tag{5.40}$$

From this base integral we first plane wave expand the dirac deltas

$$\int_{\boldsymbol{qpd}} q^{n_1}p^{n_2}d^{-2}\mathcal{L}_{\ell_1}(\mu_{q,k_1})\mathcal{L}_{\ell_2}(\mu_{p,k_1})\mathcal{L}_{\ell_3}(\mu_{q,p})P_L(q)P_L(p)\left(\int_{\boldsymbol{s}} e^{i\boldsymbol{k}_2\cdot\boldsymbol{s}}e^{-i\boldsymbol{q}\cdot\boldsymbol{s}}e^{-i\boldsymbol{p}\cdot\boldsymbol{s}}\right)\left(\int_{\boldsymbol{r}} e^{i\boldsymbol{k}_1\cdot\boldsymbol{r}}e^{i\boldsymbol{q}\cdot\boldsymbol{r}}e^{-i\boldsymbol{d}\cdot\boldsymbol{r}}\right) \tag{5.41}$$

We can do the d integral directly here since it is a well known identity

$$\int_{\boldsymbol{d}} \frac{1}{d^2}e^{-i\boldsymbol{d}\cdot\boldsymbol{r}} = \frac{1}{4\pi r} \tag{5.42}$$

Applying this

$$\int_{\boldsymbol{qprs}} q^{n_1}p^{n_2}r^{-1}(4\pi)^{-1}\mathcal{L}_{\ell_1}(\mu_{q,k_1})\mathcal{L}_{\ell_2}(\mu_{p,k_1})\mathcal{L}_{\ell_3}(\mu_{q,p})P_L(q)P_L(p)e^{i\boldsymbol{k}_2\cdot\boldsymbol{s}}e^{-i\boldsymbol{q}\cdot\boldsymbol{s}}e^{-i\boldsymbol{p}\cdot\boldsymbol{s}}e^{i\boldsymbol{k}_1\cdot\boldsymbol{r}}e^{i\boldsymbol{q}\cdot\boldsymbol{r}} \tag{5.43}$$

We now expand each legendre polynomial into spherical harmonics

$$\begin{aligned}&\int_{\boldsymbol{qprs}} q^{n_1}p^{n_2}r^{-1}(4\pi)^2\prod\nolimits_{123}^{-2}\sum_{m_1m_2m_3} Y_{\ell_1m_1}(\hat{\boldsymbol{q}})Y^*_{\ell_1m_1}(\hat{\boldsymbol{k}}_1)Y_{\ell_2m_2}(\hat{\boldsymbol{p}})Y^*_{\ell_2m_2}(\hat{\boldsymbol{k}}_1)Y_{\ell_3m_3}(\hat{\boldsymbol{q}})Y^*_{\ell_3m_3}(\hat{\boldsymbol{p}})\\ &P_L(q)P_L(p)e^{i\boldsymbol{k}_2\cdot\boldsymbol{s}}e^{-i\boldsymbol{q}\cdot\boldsymbol{s}}e^{-i\boldsymbol{p}\cdot\boldsymbol{s}}e^{i\boldsymbol{k}_1\cdot\boldsymbol{r}}e^{i\boldsymbol{q}\cdot\boldsymbol{r}}\end{aligned} \tag{5.44}$$

Continuing we expand each exponential into spherical harmonics

$$\int_{\boldsymbol{qprs}} q^{n_1}p^{n_2}r^{-1}(4\pi)^7\prod\nolimits_{123}^{-2}\sum_{\ell_{ks}\ell_{qs}\ell_{ps}\ell_{kr}\ell_{qr}}\sum_{m_1m_2m_3m_{ks}m_{qs}m_{ps}m_{kr}m_{qr}} P_L(q)P_L(p)i^{\ell_{ks}-\ell_{qs}-\ell_{ps}+\ell_{kr}+\ell_{qr}}$$

$$j_{\ell_{ks}}(k_2 s) j_{\ell_{qs}}(qs) j_{\ell_{ps}}(ps) j_{\ell_{kr}}(k_1 r) j_{\ell_{qr}}(qr) Y_{\ell_1 m_1}(\hat{\boldsymbol{q}}) Y^*_{\ell_1 m_1}(\hat{\boldsymbol{k}}_1) Y_{\ell_2 m_2}(\hat{\boldsymbol{p}}) Y^*_{\ell_2 m_2}(\hat{\boldsymbol{k}}_1) Y_{\ell_3 m_3}(\hat{\boldsymbol{q}}) Y^*_{\ell_3 m_3}(\hat{\boldsymbol{p}})$$
$$Y_{\ell_{ks} m_{ks}}(\hat{\boldsymbol{s}}) Y^*_{\ell_{ks} m_{ks}}(\hat{\boldsymbol{k}}_2) Y_{\ell_{qs} m_{qs}}(\hat{\boldsymbol{q}}) Y^*_{\ell_{qs} m_{qs}}(\hat{\boldsymbol{s}}) Y_{\ell_{ps} m_{ps}}(\hat{\boldsymbol{p}}) Y^*_{\ell_{ps} m_{ps}}(\hat{\boldsymbol{s}})$$
$$Y_{\ell_{kr} m_{kr}}(\hat{\boldsymbol{r}}) Y^*_{\ell_{kr} m_{kr}}(\hat{\boldsymbol{k}}_1) Y_{\ell_{qr} m_{qr}}(\hat{\boldsymbol{q}}) Y^*_{\ell_{qr} m_{qr}}(\hat{\boldsymbol{r}}) \tag{5.45}$$

Factoring into each angular integral

$$\int_{qprs} q^{n_1} p^{n_2} r^{-1} (4\pi)^7 \prod\nolimits_{123}^{-2} \sum_{\ell_{ks}\ell_{qs}\ell_{ps}\ell_{kr}\ell_{qr}} \sum_{m_1 m_2 m_3 m_{ks} m_{qs} m_{ps} m_{kr} m_{qr}} P_L(q) P_L(p) i^{\ell_{ks}-\ell_{qs}-\ell_{ps}+\ell_{kr}+\ell_{qr}}$$
$$j_{\ell_{ks}}(k_2 s) j_{\ell_{qs}}(qs) j_{\ell_{ps}}(ps) j_{\ell_{kr}}(k_1 r) j_{\ell_{qr}}(qr) Y^*_{\ell_1 m_1}(\hat{\boldsymbol{k}}_1) Y^*_{\ell_2 m_2}(\hat{\boldsymbol{k}}_1) Y^*_{\ell_{ks} m_{ks}}(\hat{\boldsymbol{k}}_2) Y^*_{\ell_{kr} m_{kr}}(\hat{\boldsymbol{k}}_1)$$
$$\left(\int_{\hat{\boldsymbol{r}}} Y_{\ell_{kr} m_{kr}}(\hat{\boldsymbol{r}}) Y^*_{\ell_{qr} m_{qr}}(\hat{\boldsymbol{r}})\right) \left(\int_{\hat{\boldsymbol{p}}} Y_{\ell_2 m_2}(\hat{\boldsymbol{p}}) Y^*_{\ell_3 m_3}(\hat{\boldsymbol{p}}) Y_{\ell_{ps} m_{ps}}(\hat{\boldsymbol{p}})\right) \left(\int_{\hat{\boldsymbol{s}}} Y_{\ell_{ks} m_{ks}}(\hat{\boldsymbol{s}}) Y^*_{\ell_{qs} m_{qs}}(\hat{\boldsymbol{s}}) Y^*_{\ell_{ps} m_{ps}}(\hat{\boldsymbol{s}})\right)$$
$$\left(\int_{\hat{\boldsymbol{q}}} Y_{\ell_1 m_1}(\hat{\boldsymbol{q}}) Y_{\ell_3 m_3}(\hat{\boldsymbol{q}}) Y_{\ell_{qs} m_{qs}}(\hat{\boldsymbol{q}}) Y_{\ell_{qr} m_{qr}}(\hat{\boldsymbol{q}})\right) \tag{5.46}$$

The r angular integral is trivial

$$\int_{\hat{\boldsymbol{r}}} Y_{\ell_{kr} m_{kr}}(\hat{\boldsymbol{r}}) Y^*_{\ell_{qr} m_{qr}}(\hat{\boldsymbol{r}}) = 4\pi \delta_{\ell_{kr},\ell_{qr}} \delta_{m_{kr},m_{qr}} \tag{5.47}$$

Applying this

$$\int_{qprs} q^{n_1} p^{n_2} r^{-1} (4\pi)^7 \prod\nolimits_{123}^{-2} \sum_{\ell_{ks}\ell_{qs}\ell_{ps}\ell_{kr}} \sum_{m_1 m_2 m_3 m_{ks} m_{qs} m_{ps} m_{kr}} P_L(q) P_L(p) i^{\ell_{ks}-\ell_{qs}-\ell_{ps}+2\ell_{kr}}$$
$$j_{\ell_{ks}}(k_2 s) j_{\ell_{qs}}(qs) j_{\ell_{ps}}(ps) j_{\ell_{kr}}(k_1 r) j_{\ell_{kr}}(qr) Y^*_{\ell_1 m_1}(\hat{\boldsymbol{k}}_1) Y^*_{\ell_2 m_2}(\hat{\boldsymbol{k}}_1) Y^*_{\ell_{ks} m_{ks}}(\hat{\boldsymbol{k}}_2) Y^*_{\ell_{kr} m_{kr}}(\hat{\boldsymbol{k}}_1)$$
$$\left(\int_{\hat{\boldsymbol{p}}} Y_{\ell_2 m_2}(\hat{\boldsymbol{p}}) Y^*_{\ell_3 m_3}(\hat{\boldsymbol{p}}) Y_{\ell_{ps} m_{ps}}(\hat{\boldsymbol{p}})\right) \left(\int_{\hat{\boldsymbol{s}}} Y_{\ell_{ks} m_{ks}}(\hat{\boldsymbol{s}}) Y^*_{\ell_{qs} m_{qs}}(\hat{\boldsymbol{s}}) Y^*_{\ell_{ps} m_{ps}}(\hat{\boldsymbol{s}})\right)$$
$$\left(\int_{\hat{\boldsymbol{q}}} Y_{\ell_1 m_1}(\hat{\boldsymbol{q}}) Y_{\ell_3 m_3}(\hat{\boldsymbol{q}}) Y_{\ell_{qs} m_{qs}}(\hat{\boldsymbol{q}}) Y_{\ell_{kr} m_{kr}}(\hat{\boldsymbol{q}})\right) \tag{5.48}$$

Before doing the remaining angular integrals we will next apply a coordinate system to simplify the problem. If we assign $\boldsymbol{k}_1$ to be the z-axis (equivalently the north pole) and then force $\boldsymbol{k}_2$ onto the x-z plane (equivalent to forcing the whole triangle on the plane), we get the simplification

$$Y_{lm}(\hat{\boldsymbol{k}}_1) = \sqrt{\frac{2l+1}{4\pi}} \delta_{m,0} \tag{5.49}$$

Applying this

$$\int_{qprs} q^{n_1} p^{n_2} r^{-1} (4\pi)^{5.5} \prod\nolimits_{3}^{-2} \prod\nolimits_{12}^{-1} \prod\nolimits_{(kr)} \sum_{\ell_{ks}\ell_{qs}\ell_{ps}\ell_{kr}} \sum_{m_3 m_{ks} m_{qs} m_{ps}} P_L(q) P_L(p) i^{\ell_{ks}-\ell_{qs}-\ell_{ps}+2\ell_{kr}}$$
$$j_{\ell_{ks}}(k_2 s) j_{\ell_{qs}}(qs) j_{\ell_{ps}}(ps) j_{\ell_{kr}}(k_1 r) j_{\ell_{kr}}(qr) Y^*_{\ell_{ks} m_{ks}}(\hat{\boldsymbol{k}}_2)$$

$$\left(\int_{\hat{\boldsymbol{p}}} Y_{\ell_2 0}(\hat{\boldsymbol{p}}) Y^*_{\ell_3 m_3}(\hat{\boldsymbol{p}}) Y_{\ell_{ps} m_{ps}}(\hat{\boldsymbol{p}})\right) \left(\int_{\hat{\boldsymbol{s}}} Y_{\ell_{ks} m_{ks}}(\hat{\boldsymbol{s}}) Y^*_{\ell_{qs} m_{qs}}(\hat{\boldsymbol{s}}) Y^*_{\ell_{ps} m_{ps}}(\hat{\boldsymbol{s}})\right)$$
$$\left(\int_{\hat{\boldsymbol{q}}} Y_{\ell_1 0}(\hat{\boldsymbol{q}}) Y_{\ell_3 m_3}(\hat{\boldsymbol{q}}) Y_{\ell_{qs} m_{qs}}(\hat{\boldsymbol{q}}) Y_{\ell_{kr} 0}(\hat{\boldsymbol{q}})\right) \tag{5.50}$$

We will first handle the p angular integral

$$\int_{\hat{\boldsymbol{p}}} Y_{\ell_2 0}(\hat{\boldsymbol{p}}) Y^*_{\ell_3 m_3}(\hat{\boldsymbol{p}}) Y_{\ell_{ps} m_{ps}}(\hat{\boldsymbol{p}}) = (-1)^{m_3} \mathcal{G}^{0,-m_3,m_{ps}}_{\ell_2 \ell_3 \ell_{ps}} \tag{5.51}$$

This obviously enforces $m_{ps} = m_3$. Applying this

$$\int_{qprs} q^{n_1} p^{n_2} r^{-1} (4\pi)^{5.5} \prod_3^{-2} \prod_{12}^{-1} \prod_{(kr)} \sum_{\ell_{ks}\ell_{qs}\ell_{ps}\ell_{kr}} \sum_{m_3 m_{ks} m_{qs} m_{ps}} P_L(q) P_L(p) i^{\ell_{ks}-\ell_{qs}-\ell_{ps}+2\ell_{kr}}$$
$$j_{\ell_{ks}}(k_2 s) j_{\ell_{qs}}(qs) j_{\ell_{ps}}(ps) j_{\ell_{kr}}(k_1 r) j_{\ell_{kr}}(qr) Y^*_{\ell_{ks} m_{ks}}(\hat{\boldsymbol{k}}_2)$$
$$(-1)^{m_3} \mathcal{G}^{0,m_3,-m_3}_{\ell_2 \ell_3 \ell_{ps}} \left(\int_{\hat{\boldsymbol{s}}} Y_{\ell_{ks} m_{ks}}(\hat{\boldsymbol{s}}) Y^*_{\ell_{qs} m_{qs}}(\hat{\boldsymbol{s}}) Y^*_{\ell_{ps} m_3}(\hat{\boldsymbol{s}})\right) \left(\int_{\hat{\boldsymbol{q}}} Y_{\ell_1 0}(\hat{\boldsymbol{q}}) Y_{\ell_3 m_3}(\hat{\boldsymbol{q}}) Y_{\ell_{qs} m_{qs}}(\hat{\boldsymbol{q}}) Y_{\ell_{kr} 0}(\hat{\boldsymbol{q}})\right) \tag{5.52}$$

Next we perform the s angular integral

$$\int_{\hat{\boldsymbol{s}}} Y_{\ell_{ks} m_{ks}}(\hat{\boldsymbol{s}}) Y^*_{\ell_{qs} m_{qs}}(\hat{\boldsymbol{s}}) Y^*_{\ell_{ps} m_3}(\hat{\boldsymbol{s}}) = (-1)^{q_s+m_3} \mathcal{G}^{m_{ks},-m_{qs},-m_3}_{\ell_{ks}\ell_{qs}\ell_{ps}} \tag{5.53}$$

Which gives

$$\int_{qprs} q^{n_1} p^{n_2} r^{-1} (4\pi)^{5.5} \prod_3^{-2} \prod_{12}^{-1} \prod_{(kr)} \sum_{\ell_{ks}\ell_{qs}\ell_{ps}\ell_{kr}} \sum_{m_3 m_{ks} m_{qs} m_{ps}} P_L(q) P_L(p) i^{\ell_{ks}-\ell_{qs}-\ell_{ps}+2\ell_{kr}}$$
$$j_{\ell_{ks}}(k_2 s) j_{\ell_{qs}}(qs) j_{\ell_{ps}}(ps) j_{\ell_{kr}}(k_1 r) j_{\ell_{kr}}(qr) Y^*_{\ell_{ks} m_{ks}}(\hat{\boldsymbol{k}}_2)$$
$$(-1)^{m_{qs}} \mathcal{G}^{0,m_3,-m_3}_{\ell_2 \ell_3 \ell_{ps}} \mathcal{G}^{m_{ks},-m_{qs},-m_3}_{\ell_{ks}\ell_{qs}\ell_{ps}} \left(\int_{\hat{\boldsymbol{q}}} Y_{\ell_1 0}(\hat{\boldsymbol{q}}) Y_{\ell_3 m_3}(\hat{\boldsymbol{q}}) Y_{\ell_{qs} m_{qs}}(\hat{\boldsymbol{q}}) Y_{\ell_{kr} 0}(\hat{\boldsymbol{q}})\right) \tag{5.54}$$

Now proceeding to the q angular integral

$$\int_{\hat{\boldsymbol{q}}} Y_{\ell_1 0}(\hat{\boldsymbol{q}}) Y_{\ell_3 m_3}(\hat{\boldsymbol{q}}) Y_{\ell_{qs} m_{qs}}(\hat{\boldsymbol{q}}) Y_{\ell_{kr} 0}(\hat{\boldsymbol{q}}) = \sum_{L_q} (-1)^{M_q} \mathcal{G}^{0,m_3,-M_q}_{\ell_1 \ell_3 L_q} \mathcal{G}^{M_q,m_{qs},0}_{L_q \ell_{qs} \ell_{kr}} \tag{5.55}$$

This obviously implies that $M_q = m_3$ and $m_{qs} = -m_3$ Applying this

$$\int_{qprs} q^{n_1} p^{n_2} r^{-1} (4\pi)^{5.5} \prod_3^{-2} \prod_{12}^{-1} \prod_{(kr)} \sum_{\ell_{ks}\ell_{qs}\ell_{ps}\ell_{kr} L_q} \sum_{m_3 m_{ks}} P_L(q) P_L(p) i^{\ell_{ks}-\ell_{qs}-\ell_{ps}+2\ell_{kr}}$$
$$j_{\ell_{ks}}(k_2 s) j_{\ell_{qs}}(qs) j_{\ell_{ps}}(ps) j_{\ell_{kr}}(k_1 r) j_{\ell_{kr}}(qr) Y^*_{\ell_{ks} m_{ks}}(\hat{\boldsymbol{k}}_2)$$

$$\mathcal{G}^{0,m_3,-m_3}_{\ell_2\ell_3\ell_{ps}}\mathcal{G}^{m_{ks},m_3,-m_3}_{\ell_{ks}\ell_{qs}\ell_{ps}}\mathcal{G}^{0,m_3,-m_3}_{\ell_1\ell_3L_q}\mathcal{G}^{m_3,-m_3,0}_{L_q\ell_{qs}\ell_{kr}} \tag{5.56}$$

This enforces that $m_{ks}=0$

$$\int_{qprs} q^{n_1}p^{n_2}r^{-1}(4\pi)^{5.5}\prod_3^{-2}\prod_{12}^{-1}\prod_{(kr)}\sum_{\ell_{ks}\ell_{qs}\ell_{ps}\ell_{kr}L_q}\sum_{m_3m_{ks}}P_L(q)P_L(p)i^{\ell_{ks}-\ell_{qs}-\ell_{ps}+2\ell_{kr}}$$
$$j_{\ell_{ks}}(k_2s)j_{\ell_{qs}}(qs)j_{\ell_{ps}}(ps)j_{\ell_{kr}}(k_1r)j_{\ell_{kr}}(qr)Y_{\ell_{ks}0}(\hat{\boldsymbol{k}}_2)\mathcal{G}^{0,m_3,-m_3}_{\ell_2\ell_3\ell_{ps}}\mathcal{G}^{0,m_3,-m_3}_{\ell_{ks}\ell_{qs}\ell_{ps}}\mathcal{G}^{0,m_3,-m_3}_{\ell_1\ell_3L_q}\mathcal{G}^{0,m_3,-m_3}_{\ell_{kr}L_q\ell_{qs}} \tag{5.57}$$

Expanding the last remaining spherical harmonic directly using

$$Y_{\ell_{ks}0}(\hat{\boldsymbol{k}}_2)=\sqrt{\frac{2\ell_{ks}+1}{4\pi}}\mathcal{L}_{\ell_{ks}}(\cos\theta_{\hat{\boldsymbol{k}}_2}) \tag{5.58}$$

Giving

$$\int_{qprs} q^{n_1}p^{n_2}r^{-1}(4\pi)^{5}\prod_3^{-2}\prod_{12}^{-1}\prod_{(kr)(ks)}\sum_{\ell_{ks}\ell_{qs}\ell_{ps}\ell_{kr}L_q}\sum_{m_3}P_L(q)P_L(p)i^{\ell_{ks}-\ell_{qs}-\ell_{ps}+2\ell_{kr}}$$
$$j_{\ell_{ks}}(k_2s)j_{\ell_{qs}}(qs)j_{\ell_{ps}}(ps)j_{\ell_{kr}}(k_1r)j_{\ell_{kr}}(qr)\mathcal{L}_{\ell_{ks}}(\hat{\boldsymbol{k}}_1\cdot\hat{\boldsymbol{k}}_2)\mathcal{G}^{0,m_3,-m_3}_{\ell_2\ell_3\ell_{ps}}\mathcal{G}^{0,m_3,-m_3}_{\ell_{ks}\ell_{qs}\ell_{ps}}\mathcal{G}^{0,m_3,-m_3}_{\ell_1\ell_3L_q}\mathcal{G}^{0,m_3,-m_3}_{\ell_{kr}L_q\ell_{qs}} \tag{5.59}$$

The m_3 sum can be written as

$$\begin{aligned}
&\sum_{m_3}\mathcal{G}^{m_3,0,-m_3}_{\ell_3\ell_2\ell_{ps}}\mathcal{G}^{m_3,0,-m_3}_{\ell_{ps}\ell_{ks}\ell_{qs}}\mathcal{G}^{m_3,0,-m_3}_{\ell_{qs}\ell_{kr}L_q}\mathcal{G}^{m_3,0,-m_3}_{L_q\ell_1\ell_3}\\
&=(-1)^{\ell_2+\ell_{kr}}\prod^2_{3(ps)(qs)L_q}\prod_{12(kr)(ks)}(4\pi)^{-2}\\
&\times\begin{pmatrix}\ell_3&\ell_2&\ell_{ps}\\0&0&0\end{pmatrix}\begin{pmatrix}\ell_{ps}&\ell_{ks}&\ell_{qs}\\0&0&0\end{pmatrix}\begin{pmatrix}\ell_{qs}&\ell_{kr}&L_q\\0&0&0\end{pmatrix}\begin{pmatrix}L_q&\ell_1&\ell_3\\0&0&0\end{pmatrix}\\
&\times\sum_{xm_x}(-1)^{x-m_x}\prod^2_x\begin{pmatrix}\ell_2&x&\ell_1\\0&-m_x&0\end{pmatrix}\begin{pmatrix}\ell_{ks}&x&\ell_{kr}\\0&m_x&0\end{pmatrix}\begin{Bmatrix}\ell_2&x&\ell_1\\L_q&\ell_3&\ell_{ps}\end{Bmatrix}\begin{Bmatrix}\ell_{ks}&x&\ell_{kr}\\L_q&\ell_{qs}&\ell_{ps}\end{Bmatrix}
\end{aligned} \tag{5.60}$$

This sum is given by [116] Eq. 12.1.4.10. Combing this with the original expression (and applying that m_x is obviously 0)

$$\int_{qprs} q^{n_1}p^{n_2}r^{-1}(4\pi)^{3}\prod^2_{(kr)(ks)(ps)(qs)L_qx}\sum_{\ell_{ks}\ell_{qs}\ell_{ps}\ell_{kr}L_qx}P_L(q)P_L(p)i^{\ell_{ks}-\ell_{qs}-\ell_{ps}+2\ell_{kr}}(-1)^{\ell_1+\ell_{kr}}$$

$$j_{\ell_{ks}}(k_2 s) j_{\ell_{qs}}(qs) j_{\ell_{ps}}(ps) j_{\ell_{kr}}(k_1 r) j_{\ell_{kr}}(qr) \mathcal{L}_{\ell_{ks}}(\hat{\boldsymbol{k}}_1 \cdot \hat{\boldsymbol{k}}_2) \begin{pmatrix} \ell_3 & \ell_2 & \ell_{ps} \\ 0 & 0 & 0 \end{pmatrix} \begin{pmatrix} \ell_{ps} & \ell_{ks} & \ell_{qs} \\ 0 & 0 & 0 \end{pmatrix} \begin{pmatrix} \ell_{qs} & \ell_{kr} & L_q \\ 0 & 0 & 0 \end{pmatrix}$$
$$\times \begin{pmatrix} L_q & \ell_1 & \ell_3 \\ 0 & 0 & 0 \end{pmatrix} \begin{pmatrix} \ell_2 & x & \ell_1 \\ 0 & 0 & 0 \end{pmatrix} \begin{pmatrix} \ell_{ks} & x & \ell_{kr} \\ 0 & 0 & 0 \end{pmatrix} \begin{Bmatrix} \ell_2 & x & \ell_1 \\ L_q & \ell_3 & \ell_{ps} \end{Bmatrix} \begin{Bmatrix} \ell_{ks} & x & \ell_{kr} \\ L_q & \ell_{qs} & \ell_{ps} \end{Bmatrix} \tag{5.61}$$

This is an infinite sum, very similar to the one discussed in Sec. 5.2.1. We can write this more succinctly as

$$\begin{aligned} &\sum_{\ell_{ks}\ell_{qs}\ell_{ps}\ell_{kr}L_q x} (4\pi)^3 \prod_{(kr)(ks)(ps)(qs)L_q x}^2 i^{\ell_{ks}-\ell_{qs}-\ell_{ps}+2\ell_{kr}} (-1)^{\ell_1+\ell_{kr}} \mathcal{L}_{\ell_{ks}}(\hat{\boldsymbol{k}}_1 \cdot \hat{\boldsymbol{k}}_2) \\ &\mathcal{B}^{(123I)n_1 n_2}_{\ell_{kr}\ell_{ks}\ell_{kr}\ell_{qs}\ell_{ps}}(k_1, k_2) \\ &\begin{pmatrix} \ell_3 & \ell_2 & \ell_{ps} \\ 0 & 0 & 0 \end{pmatrix} \begin{pmatrix} \ell_{ps} & \ell_{ks} & \ell_{qs} \\ 0 & 0 & 0 \end{pmatrix} \begin{pmatrix} \ell_{qs} & \ell_{kr} & L_q \\ 0 & 0 & 0 \end{pmatrix} \begin{pmatrix} L_q & \ell_1 & \ell_3 \\ 0 & 0 & 0 \end{pmatrix} \begin{pmatrix} \ell_2 & x & \ell_1 \\ 0 & 0 & 0 \end{pmatrix} \\ &\begin{pmatrix} \ell_{ks} & x & \ell_{kr} \\ 0 & 0 & 0 \end{pmatrix} \begin{Bmatrix} \ell_2 & x & \ell_1 \\ L_q & \ell_3 & \ell_{ps} \end{Bmatrix} \begin{Bmatrix} \ell_{ks} & x & \ell_{kr} \\ L_q & \ell_{qs} & \ell_{ps} \end{Bmatrix} \end{aligned} \tag{5.62}$$

Where

$$\mathcal{B}^{(123I)n_1 n_2}_{\ell_{kr}\ell_{ks}\ell_{kr}\ell_{qs}\ell_{ps}}(k_1, k_2) = \int_{rs} r^{-1} j_{\ell_{kr}}(k_1 r) j_{\ell_{ks}}(k_2 s) \Xi^{n_1}_{\ell_{kr}\ell_{qs}}(r, s) \xi^{n_2}_{\ell_{ps}}(s) \tag{5.63}$$

5.4 B_{411}

Neglecting the prefactor and cyclic terms we are left with the integration

$$\int_{\boldsymbol{q}} F_4^{(s)}(\boldsymbol{q}, -\boldsymbol{q}, -\boldsymbol{k}_1, -\boldsymbol{k}_2) P_L(q) \tag{5.64}$$

Expanding this results in the fundamental integral

$$\int_{\boldsymbol{q}} \frac{1}{|\boldsymbol{k}_1 - \boldsymbol{q}|^2 |\boldsymbol{k}_2 + \boldsymbol{q}|^2} q^n \mathcal{L}_{\ell_1}(\mu_{q,k_1}) \mathcal{L}_{\ell_2}(\mu_{q,k_2}) P_L(q) \tag{5.65}$$

Note that arriving at this fundamental form is non-trivial. We discuss how we got this form in Sec. 5.4.2.

5.4.1 411-Type Integral

We start by using dirac deltas to simplify the denominators

$$\int_{\boldsymbol{qpd}} \frac{1}{pd} q^n \mathcal{L}_{\ell_1}(\mu_{q,k_1}) \mathcal{L}_{\ell_2}(\mu_{q,k_2}) P_L(q) \delta^D(\boldsymbol{k}_1 - \boldsymbol{q} - \boldsymbol{p}) \delta^D(\boldsymbol{k}_2 + \boldsymbol{q} - \boldsymbol{d}) \tag{5.66}$$

Now we expand each delta

$$\int_{\boldsymbol{qpdrs}} \frac{1}{p^2 d^2} q^n \mathcal{L}_{\ell_1}(\mu_{q,k_1}) \mathcal{L}_{\ell_2}(\mu_{q,k_2}) P_L(q) e^{i\boldsymbol{k}_1 \cdot \boldsymbol{r}} e^{-i\boldsymbol{q}\cdot\boldsymbol{r}} e^{-i\boldsymbol{p}\cdot\boldsymbol{r}} e^{i\boldsymbol{k}_2\cdot\boldsymbol{s}} e^{i\boldsymbol{q}\cdot\boldsymbol{s}} e^{-i\boldsymbol{d}\cdot\boldsymbol{s}} \tag{5.67}$$

We can do both the p and d integral directly with the identity

$$\int_{\boldsymbol{p}} \frac{1}{p^2} e^{-i\boldsymbol{p}\cdot\boldsymbol{r}} = \frac{1}{4\pi r} \tag{5.68}$$

This results in

$$\int_{\boldsymbol{qrs}} \frac{1}{rs} q^n (4\pi)^{-2} \mathcal{L}_{\ell_1}(\mu_{q,k_1}) \mathcal{L}_{\ell_2}(\mu_{q,k_2}) P_L(q) e^{i\boldsymbol{k}_1 \cdot \boldsymbol{r}} e^{-i\boldsymbol{q}\cdot\boldsymbol{r}} e^{i\boldsymbol{k}_2\cdot\boldsymbol{s}} e^{i\boldsymbol{q}\cdot\boldsymbol{s}} \tag{5.69}$$

We now expand the remaining exponentials into spherical harmonics

$$\int_{\boldsymbol{qrs}} \frac{1}{rs} q^n (4\pi)^2 \mathcal{L}_{\ell_1}(\mu_{q,k_1}) \mathcal{L}_{\ell_2}(\mu_{q,k_2}) P_L(q) \sum_{\ell_{kr}\ell_{qr}\ell_{ks}\ell_{qs}} \sum_{m_{kr}m_{qr}m_{ks}m_{qs}} i^{\ell_{kr}-\ell_{qr}+\ell_{ks}+\ell_{qs}} j_{\ell_{kr}}(k_1 r) j_{\ell_{qr}}(qr)$$
$$j_{\ell_{ks}}(k_2 s) j_{\ell_{qs}}(qs) Y_{\ell_{kr}m_{kr}}(\hat{\boldsymbol{r}}) Y^*_{\ell_{kr}m_{kr}}(\hat{\boldsymbol{k}}_1) Y_{\ell_{qr}m_{qr}}(\hat{\boldsymbol{q}}) Y^*_{\ell_{qr}m_{qr}}(\hat{\boldsymbol{r}}) Y_{\ell_{ks}m_{ks}}(\hat{\boldsymbol{k}}_2) Y^*_{\ell_{ks}m_{ks}}(\hat{\boldsymbol{s}}) Y_{\ell_{qs}m_{qs}}(\hat{\boldsymbol{s}}) Y^*_{\ell_{qs}m_{qs}}(\hat{\boldsymbol{q}}) \tag{5.70}$$

The r and s angular integrals here are trivial applications of

$$\int_{\hat{\boldsymbol{r}}} Y_{\ell_{kr}m_{kr}}(\hat{\boldsymbol{r}}) Y^*_{\ell_{qr}m_{qr}}(\hat{\boldsymbol{r}}) = 4\pi \delta_{\ell_{kr},\ell_{qr}} \delta_{m_{kr},m_{qr}} \tag{5.71}$$

Simplifying

$$\int_{\boldsymbol{qrs}} \frac{1}{rs} q^n (4\pi)^4 \mathcal{L}_{\ell_1}(\mu_{q,k_1}) \mathcal{L}_{\ell_2}(\mu_{q,k_2}) P_L(q) \sum_{\ell_{kr}\ell_{ks}} \sum_{m_{kr}m_{ks}} (-1)^{\ell_{ks}} j_{\ell_{kr}}(k_1 r) j_{\ell_{kr}}(qr) j_{\ell_{ks}}(k_2 s) j_{\ell_{ks}}(qs)$$
$$Y^*_{\ell_{kr}m_{kr}}(\hat{\boldsymbol{k}}_1) Y_{\ell_{kr}m_{kr}}(\hat{\boldsymbol{q}}) Y_{\ell_{ks}m_{ks}}(\hat{\boldsymbol{k}}_2) Y^*_{\ell_{ks}m_{ks}}(\hat{\boldsymbol{q}}) \tag{5.72}$$

We now expand the legendre polynomials

$$\int_{\boldsymbol{qrs}} \sum_{\ell_{kr}\ell_{ks}} \sum_{m_{kr}m_{ks}m_1m_2} \frac{1}{rs} q^n (4\pi)^6 \prod\nolimits_{12}^{-2} P_L(q) (-1)^{\ell_{ks}} j_{\ell_{kr}}(k_1 r) j_{\ell_{kr}}(qr) j_{\ell_{ks}}(k_2 s) j_{\ell_{ks}}(qs)$$

$$Y_{\ell_1 m_1}(\hat{\boldsymbol{q}})Y^*_{\ell_1 m_1}(\hat{\boldsymbol{k}}_1)Y_{\ell_2 m_2}(\hat{\boldsymbol{q}})Y^*_{\ell_2 m_2}(\hat{\boldsymbol{k}}_2)Y^*_{\ell_{kr} m_{kr}}(\hat{\boldsymbol{k}}_1)Y_{\ell_{kr} m_{kr}}(\hat{\boldsymbol{q}})Y_{\ell_{ks} m_{ks}}(\hat{\boldsymbol{k}}_2)Y^*_{\ell_{ks} m_{ks}}(\hat{\boldsymbol{q}}) \quad (5.73)$$

The remaining q angular integral looks like

$$(-1)^{m_{ks}}\int_{\hat{\boldsymbol{q}}} Y_{\ell_1 m_1}(\hat{\boldsymbol{q}})Y_{\ell_2 m_2}(\hat{\boldsymbol{q}})Y_{\ell_{kr} m_{kr}}(\hat{\boldsymbol{q}})Y_{\ell_{ks} -m_{ks}}(\hat{\boldsymbol{q}}) = \sum_{L_q}(-1)^{M_q+m_{ks}}\mathcal{G}^{m_1,m_2,-M_q}_{\ell_1\ell_2 L_q}\mathcal{G}^{M_q,m_{kr},-m_{ks}}_{L_q\ell_{kr}\ell_{ks}} \quad (5.74)$$

Plugging this in

$$\int_{qrs}\sum_{\ell_{kr}\ell_{ks}L_q}\sum_{m_{kr}m_{ks}m_1m_2}\frac{1}{rs}q^n(4\pi)^6\prod_{12}^{-2}P_L(q)(-1)^{\ell_{ks}+m_{kr}}j_{\ell_{kr}}(k_1r)j_{\ell_{kr}}(qr)j_{\ell_{ks}}(k_2s)j_{\ell_{ks}}(qs)$$
$$Y^*_{\ell_1 m_1}(\hat{\boldsymbol{k}}_1)Y^*_{\ell_2 m_2}(\hat{\boldsymbol{k}}_2)Y^*_{\ell_{kr} m_{kr}}(\hat{\boldsymbol{k}}_1)Y_{\ell_{ks} m_{ks}}(\hat{\boldsymbol{k}}_2)\mathcal{G}^{m_1,m_2,-M_q}_{\ell_1\ell_2 L_q}\mathcal{G}^{M_q,m_{kr},-m_{ks}}_{L_q\ell_{kr}\ell_{ks}} \quad (5.75)$$

We now apply our coordinate system. If we assign $\boldsymbol{k}_1$ to be on the z-axis and then force $\boldsymbol{k}_2$ onto the x-z plane (note this also forces $\boldsymbol{k}_3$ onto the x-z plane). This enforces

$$Y_{lm}(\hat{\boldsymbol{k}}_1) = \sqrt{\frac{2l+1}{4\pi}}\delta_{m,0} \quad (5.76)$$

Applying this coordinate system to our integral results in

$$\int_{qrs}\sum_{\ell_{kr}\ell_{ks}L_q}\sum_{m_{ks}m_2}\frac{1}{rs}q^n(4\pi)^5\prod_{2}^{-2}\prod_{1}^{-1}\prod_{(kr)}P_L(q)(-1)^{\ell_{ks}}j_{\ell_{kr}}(k_1r)j_{\ell_{kr}}(qr)j_{\ell_{ks}}(k_2s)j_{\ell_{ks}}(qs)$$
$$Y^*_{\ell_2 m_2}(\hat{\boldsymbol{k}}_2)Y_{\ell_{ks} m_{ks}}(\hat{\boldsymbol{k}}_2)\mathcal{G}^{0,m_2,-M_q}_{\ell_1\ell_2 L_q}\mathcal{G}^{M_q,0,-m_{ks}}_{L_q\ell_{kr}\ell_{ks}} \quad (5.77)$$

The 3j symbols now enforce $M_q = m_2$ therefore $m_{ks} = m_2$

$$\int_{qrs}\sum_{\ell_{kr}\ell_{ks}L_q}\sum_{m_2}\frac{1}{rs}q^n(4\pi)^5\prod_{2}^{-2}\prod_{1}^{-1}\prod_{(kr)}P_L(q)(-1)^{\ell_{ks}}j_{\ell_{kr}}(k_1r)j_{\ell_{kr}}(qr)j_{\ell_{ks}}(k_2s)j_{\ell_{ks}}(qs)$$
$$Y^*_{\ell_2 m_2}(\hat{\boldsymbol{k}}_2)Y_{\ell_{ks} m_2}(\hat{\boldsymbol{k}}_2)\mathcal{G}^{0,m_2,-m_2}_{\ell_1\ell_2 L_q}\mathcal{G}^{m_2,0,-m_2}_{L_q\ell_{kr}\ell_{ks}} \quad (5.78)$$

This expands to

$$\int_{qrs}\sum_{\ell_{kr}\ell_{ks}L_q}\frac{1}{rs}q^n(4\pi)^4\prod_{2}^{-1}\prod_{\ell_{ks}}\prod_{(kr)L_q}^{2}P_L(q)(-1)^{\ell_{ks}}j_{\ell_{kr}}(k_1r)j_{\ell_{kr}}(qr)j_{\ell_{ks}}(k_2s)j_{\ell_{ks}}(qs)$$
$$\begin{pmatrix}\ell_1 & \ell_2 & L_q\\ 0 & 0 & 0\end{pmatrix}\begin{pmatrix}L_q & \ell_{kr} & \ell_{ks}\\ 0 & 0 & 0\end{pmatrix}\sum_{m_2}Y^*_{\ell_2 m_2}(\hat{\boldsymbol{k}}_2)Y_{\ell_{ks} m_2}(\hat{\boldsymbol{k}}_2)\begin{pmatrix}\ell_1 & \ell_2 & L_q\\ 0 & m_2 & -m_2\end{pmatrix}\begin{pmatrix}\text{Ł}_q & \ell_{kr} & \ell_{ks}\\ m_2 & 0 & -m_2\end{pmatrix} \quad (5.79)$$

We can combine both remaining spherical harmonics into a single spherical harmonic

$$\int_{qrs} \sum_{\ell_{kr}\ell_{ks}L_q} \frac{1}{rs} q^n (4\pi)^4 \prod_2^{-1} \prod_{\ell_{ks}} \prod_{(kr)L_q}^2 P_L(q)(-1)^{\ell_{ks}} j_{\ell_{kr}}(k_1 r) j_{\ell_{kr}}(qr) j_{\ell_{ks}}(k_2 s) j_{\ell_{ks}}(qs)$$
$$\begin{pmatrix} \ell_1 & \ell_2 & L_q \\ 0 & 0 & 0 \end{pmatrix} \begin{pmatrix} L_q & \ell_{kr} & \ell_{ks} \\ 0 & 0 & 0 \end{pmatrix} \sum_{m_2} (-1)^{m_2} \sum_{L_k} \mathcal{G}^{-m_2,m_2,0}_{\ell_2 \ell_{ks} L_k} Y_{L_k 0}(\hat{\boldsymbol{k}}_2) \begin{pmatrix} \ell_1 & \ell_2 & L_q \\ 0 & m_2 & -m_2 \end{pmatrix} \begin{pmatrix} L_q & \ell_{kr} & \ell_{ks} \\ m_2 & 0 & -m_2 \end{pmatrix} \tag{5.80}$$

The spherical harmonic trivially reduces by

$$Y_{L_k 0}(\hat{\boldsymbol{k}}_2) = \sqrt{\frac{2L_k+1}{4\pi}} \mathcal{L}_{L_k}(\hat{\boldsymbol{k}}_1 \cdot \hat{\boldsymbol{k}}_2) \tag{5.81}$$

Giving

$$\int_{qrs} \sum_{\ell_{kr}\ell_{ks}L_q L_k} \frac{1}{rs} q^n (4\pi)^3 \prod_{\ell_{ks}L_k(kr)L_q}^2 P_L(q)(-1)^{\ell_{ks}} j_{\ell_{kr}}(k_1 r) j_{\ell_{kr}}(qr) j_{\ell_{ks}}(k_2 s) j_{\ell_{ks}}(qs)$$
$$\mathcal{L}_{L_k}(\hat{\boldsymbol{k}}_1 \cdot \hat{\boldsymbol{k}}_2) \begin{pmatrix} \ell_1 & \ell_2 & L_q \\ 0 & 0 & 0 \end{pmatrix} \begin{pmatrix} L_q & \ell_{kr} & \ell_{ks} \\ 0 & 0 & 0 \end{pmatrix} \begin{pmatrix} \ell_2 & \ell_{ks} & L_k \\ 0 & 0 & 0 \end{pmatrix}$$
$$\sum_{m_2} (-1)^{m_2} \begin{pmatrix} \ell_2 & \ell_{ks} & L_k \\ -m_2 & m_2 & 0 \end{pmatrix} \begin{pmatrix} \ell_1 & \ell_2 & L_q \\ 0 & m_2 & -m_2 \end{pmatrix} \begin{pmatrix} L_q & \ell_{kr} & \ell_{ks} \\ m_2 & 0 & -m_2 \end{pmatrix} \tag{5.82}$$

This sum exactly follows [116] Eq. 12.1.3.6 resulting in

$$\sum_{m_2} (-1)^{m_2} \begin{pmatrix} \ell_2 & \ell_1 & L_q \\ m_2 & 0 & -m_2 \end{pmatrix} \begin{pmatrix} L_q & \ell_{kr} & \ell_{ks} \\ m_2 & 0 & -m_2 \end{pmatrix} \begin{pmatrix} \ell_{ks} & L_k & \ell_2 \\ m_2 & 0 & -m_2 \end{pmatrix}$$
$$= (-1)^{\ell_2 + L_q + \ell_{ks}} \begin{pmatrix} \ell_1 & \ell_{kr} & L_k \\ 0 & 0 & 0 \end{pmatrix} \begin{Bmatrix} \ell_1 & \ell_{kr} & L_k \\ \ell_{ks} & \ell_2 & L_q \end{Bmatrix} \tag{5.83}$$

Plugging this in

$$\int_{qrs} \sum_{\ell_{kr}\ell_{ks}L_q L_k} \frac{1}{rs} q^n (4\pi)^3 \prod_{\ell_{ks}L_k(kr)L_q}^2 P_L(q)(-1)^{\ell_1} j_{\ell_{kr}}(k_1 r) j_{\ell_{kr}}(qr) j_{\ell_{ks}}(k_2 s) j_{\ell_{ks}}(qs) \mathcal{L}_{L_k}(\hat{\boldsymbol{k}}_1 \cdot \hat{\boldsymbol{k}}_2)$$
$$\begin{pmatrix} \ell_2 & \ell_1 & L_q \\ 0 & 0 & 0 \end{pmatrix} \begin{pmatrix} L_q & \ell_{kr} & \ell_{ks} \\ 0 & 0 & 0 \end{pmatrix} \begin{pmatrix} \ell_{ks} & L_k & \ell_2 \\ 0 & 0 & 0 \end{pmatrix} \begin{pmatrix} \ell_1 & \ell_{kr} & L_k \\ 0 & 0 & 0 \end{pmatrix} \begin{Bmatrix} \ell_1 & \ell_{kr} & L_k \\ \ell_{ks} & \ell_2 & L_q \end{Bmatrix} \tag{5.84}$$

This is an infinite sum similar to the rest. This simplifies to

$$\sum_{\ell_{kr}\ell_{ks}L_qL_k} \frac{1}{rs} q^n (4\pi)^3 \prod_{\ell_{ks}L_k(kr)L_q}^2 (-1)^{\ell_1} \mathcal{B}^{(411)n}_{\ell_{kr}\ell_{ks}\ell_{kr}\ell_{ks}}(k_1,k_2) \mathcal{L}_{L_k}(\hat{\boldsymbol{k}}_1 \cdot \hat{\boldsymbol{k}}_2)$$
$$\begin{pmatrix} \ell_2 & \ell_1 & L_q \\ 0 & 0 & 0 \end{pmatrix} \begin{pmatrix} L_q & \ell_{kr} & \ell_{ks} \\ 0 & 0 & 0 \end{pmatrix} \begin{pmatrix} \ell_{ks} & L_k & \ell_2 \\ 0 & 0 & 0 \end{pmatrix} \begin{pmatrix} \ell_1 & \ell_{kr} & L_k \\ 0 & 0 & 0 \end{pmatrix} \begin{Bmatrix} \ell_1 & \ell_{kr} & L_k \\ \ell_{ks} & \ell_2 & L_q \end{Bmatrix} \tag{5.85}$$

Where

$$\mathcal{B}^{(411)n}_{\ell_{kr}\ell_{ks}\ell_{kr}\ell_{ks}}(k_1,k_2) = \int_{rs} \frac{1}{rs} \Xi^n_{\ell_{kr}\ell_{ks}}(r,s) j_{\ell_{kr}}(k_1 r) j_{\ell_{ks}}(k_2 s) \tag{5.86}$$

5.4.2 Fundamental Form Reduction

When expanding $F_4^{(s)}$ naively there are a variety of terms that appear. The fundamental distinction that matters for our purpose is the number of denominator terms and which k appears in them.

If we focus on the first cyclic term, hereafter known as the k_1k_2 cycle after the terms appearing in the power spectra outside of the integral, there are some terms that are trivially transformable into the desired fundamental form. For the "constant" terms, by which we mean no denominator, the terms involving just one of the desired two denominators, either the solo k_1 or solo k_2 terms, and of course the terms that are already in the desired fundamental form (note that any terms with only a sign difference are also trivial since the integral is symmetric about $q \to -q$.)

Besides these trivial terms there are some terms which are not able to directly transform into the fundamental form. There are three types of these terms we shall discuss one-by-one. The first are terms with two denominators but k_1 and k_3 instead of k_2. These terms can be transformed into the fundamental form by exchanging them with the equivalent terms from a different cycle. Specifically the equivalent terms here are the k_1 and k_2 denominator terms from the k_1k_3 cycle. Since these terms have identical coefficients we can merely swap them. Similarly there also exists k_2 and k_3 denominator terms which have an equivalent partner in the k_2k_3 cycles k_1 and k_2 denominator terms.

The final term which cannot trivially transform into the fundamental form are solo k_3 denominator terms. There does not quite exist an equivalent here to swap with, but instead we need to perform a cyclic exchange. What we mean by this is that the solo k_3 terms from the k_1k_2 cycle are given to the k_1k_3 cycle, which sends its own solo k_2 terms to the k_2k_3 cycle, which sends its solo k_1 terms to the original k_1k_2 cycle. In brief this is the direction of the exchange $k_1k_2 \to k_1k_3 \to k_2k_3 \to k_1k_2$. Note these all have identical

coefficients so the exchange can be performed straightforwardly. From here these terms can be trivially transformed into the fundamental form (just by multiplying and dividing by $|\boldsymbol{k}_2 + \boldsymbol{q}|^2$.)

Chapter 6
Higher Order Estimators & Parallelization

As we transition from the power spectrum to higher order clustering statistics, specifically the Bispectrum and other higher order polyspectra, an important computational cost to consider is their estimation from a dataset. Unlike with the power spectrum, naive estimation of a higher order polyspectrum can quickly become computationally expensive so in this section we take an existing optimized bispectrum estimator and extend it to all higher order polyspectra. In addition, we also demonstrate how to best parallelize such an estimator for optimal performance.

6.1 The Higher Order Scoccimarro Estimator

The estimator for polyspectra that we shall parallelize here is based on the Scoccimarro estimator [92; 120] that we summarize in this section. In this section, we shall mainly discuss the algorithm with the equations in the continuous limit and summarize the discrete implementation in App. D.

Let us begin with the bispectrum estimator. The estimator for the monopole bispectrum $B(k_1, k_2, k_3)$ takes the average of $\delta(\boldsymbol{q}_1)\delta(\boldsymbol{q}_2)\delta(\boldsymbol{q}_3)$ for all possible combinations of three vectors $|q_i - k_i| < \delta k_i/2$ $(i = 1, 2, 3)$ that satisfy the triangle condition $(\boldsymbol{q}_{123} = 0)$. We denote the bin size in i-th direction as δk_i, although, throughout the paper, we choose the bin size for all three directions the same for simplicity. The extension of the method to arbitrary bin size is trivial. We may formulate the bispectrum estimator as

$$B(k_1, k_2, k_3) = \frac{1}{VN_{(123)}} \sum_{q_1 \sim k_1} \sum_{q_2 \sim k_2} \sum_{q_3 \sim k_3}$$

$$\times \delta(\boldsymbol{q}_1)\delta(\boldsymbol{q}_2)\delta(\boldsymbol{q}_3)\delta^D(\boldsymbol{q}_{123})\,, \tag{6.1}$$

with $N_{(123)}$ being the number of triplets $(\boldsymbol{q}_1, \boldsymbol{q}_2, \boldsymbol{q}_3)$ satisfying the binning condition ($|q_i - k_i| < \delta k_i$ which is denoted as $q_i \sim k_i$) and the triangle condition: $N_{(123)} = \sum_{\boldsymbol{q}_1,\boldsymbol{q}_2,\boldsymbol{q}_3} \delta^D(\boldsymbol{q}_{123})$ with the same summation as Eq. (6.1). Throughout the paper, we impose the condition that $k_1 \geq k_2 \geq k_3$ to avoid the duplication.

In the continuous limit, the bispectrum estimator becomes (see, App. D for the details about the normalization factor)

$$\begin{aligned} B(k_1, k_2, k_3) =& \frac{V_f}{V^B_{(123)}(2\pi)^3} \int_{k_1} d^3q_1 \int_{k_2} d^3q_2 \int_{k_3} d^3q_3 \\ & \times \delta(\boldsymbol{q}_1)\delta(\boldsymbol{q}_2)\delta(\boldsymbol{q}_3)\delta_D(\mathbf{q}_{123}) \end{aligned} \tag{6.2}$$

where V_f is the volume of a fundamental Fourier cell, $(2\pi)^3/V$, and $V^B_{(123)}$ is the Fourier space volume defined as

$$V^B_{(123)} \;= \int_{k_1} d^3q_1 \int_{k_2} d^3q_2 \int_{k_3} d^3q_3 \delta_D(\mathbf{q}_{123})\,. \tag{6.3}$$

The key step for the Scoccimarro estimator is promoting the Dirac-delta operator with its Fourier representation:

$$\delta_D(\boldsymbol{q}_{123}) = \int \frac{d^3x}{(2\pi)^3} e^{-i\boldsymbol{x}\cdot(\boldsymbol{q}_1+\boldsymbol{q}_2+\boldsymbol{q}_3)}\,, \tag{6.4}$$

with which we can recast the three integrals for sampling triangles in Eq. (6.2) into single integration:

$$B(k_1, k_2, k_3) = \frac{V_f}{V^B_{(123)}(2\pi)^3} \int \frac{d^3x}{(2\pi)^3} I_{k_1}(\boldsymbol{x}) I_{k_2}(\boldsymbol{x}) I_{k_3}(\boldsymbol{x})\,. \tag{6.5}$$

Here,

$$I_{k_i}(\boldsymbol{x}) \equiv \int_{k_i} d^3q \delta(\boldsymbol{q}) e^{-i\boldsymbol{q}\cdot\boldsymbol{x}} \equiv \int d^3q \tilde{I}_{k_i}(\boldsymbol{q}) e^{-i\boldsymbol{q}\cdot\boldsymbol{x}}\,, \tag{6.6}$$

is the Fourier transformation of the function $\tilde{I}_{k_i}(\boldsymbol{q})$ that is defined with the density field in the spherical shell defined by $|q - k_i| < \delta k_i/2$ and zero otherwise. That is, instead of time-consuming operation of sampling all possible triangles, the Scoccimarro estimator involves Fourier transformation for computing $I_{k_i}(\boldsymbol{x})$ at each wavenumber bin, and summing over the product of three I_{k_i}s.

Note that the complexity, or the scaling of the computation time as a function of system size, of the Scoccimarro estimator is the same as the direct summation's scaling

of $N_{\rm max}^6$ for the case of bispectrum. The Scoccimarro estimator, however, reduces the computation time in two ways. First, we have fewer total numerical operations. The direct sampling involves looping over the full ranges of $-N_{\rm max} \sim N_{\rm max}$ for each component of $\boldsymbol{k}_1$ and $\pm N_{\rm max}/2 \sim \pm N_{\rm max}$ for each component of $\boldsymbol{k}_2$, because our convention of $k_1 \geq k_2 \geq k_3$ with triangle condition constrains $k_1/2 \leq k_2 \leq k_1$. On the other hand, the Scoccimarro estimator reduces it to the matrix inner product ($N_{\rm max}^3$ operation) only for the amplitude triplets (k_1, k_2, k_3). Second, for the Scoccimarro estimator, the three-dimensional array $\delta(\boldsymbol{q})$ is accessed in an ordered manner that is easier for the CPU to cache. In contrast, the direct sampling accesses $\delta(\boldsymbol{q}_3)$ in an irregular manner, which is inevitable because the value for $\boldsymbol{q}_3$ is determined by $\boldsymbol{q}_3 = -\boldsymbol{q}_1 - \boldsymbol{q}_2$. Combining these two factors, the serial version of the Scoccimarro estimator is a factor of 10 faster than the direct sampling in our implementation.

The reduction of operation time is even more striking as we calculate the higher order correlation functions. When computing the 'angle-averaged' n-point polyspectra that are only a function of the Fourier wavenumbers [121], the Scoccimarro estimator's complexity increases only by one more power of $N_{\rm max}$, $\mathcal{O}(N_{\rm max}^{n+3})$ while the direct sampling method's complexity grows by three powers of $N_{\rm max}$ at each order: $\mathcal{O}(N_{\rm max}^{3(n-1)})$. Needless to say that the base operation time for Scoccimarro estimator is much faster than the direct sampling case, as we have already seen in the case of the bispectrum where the two method have the same complexity.

Extending the bispectrum estimator in Eq. (6.5) for the angle averaged higher-order polyspectra is straightforward:

$$\begin{aligned}
&\tilde{P}_n(k_1 \cdots, k_n) \\
=&\frac{V_f}{V^{\tilde{n}}_{(12\cdots n)}(2\pi)^3} \int_{k_1} d^3q_1 \cdots \int_{k_n} d^3q_n \delta_D(\mathbf{q}_{1\cdots n}) \prod \delta(\mathbf{q}_i) \\
=&\frac{V_f}{V^{\tilde{n}}_{(12\cdots n)}(2\pi)^3} \int \frac{d^3x}{(2\pi)^3} I_{k_1}(\boldsymbol{x}) \cdots I_{k_n}(\boldsymbol{x})
\end{aligned} \tag{6.7}$$

with the Fourier volume

$$V^{\tilde{n}}_{(12\cdots n)} = \int_{k_1} d^3q_1 \cdots \int_{k_n} d^3q_n \delta_D(\mathbf{q}_{1\cdots n})\,. \tag{6.8}$$

occupied by $\boldsymbol{q}_1, \cdots, \boldsymbol{q}_n$ that contribute to the estimation of angle-averaged n-th order

polyspectrum. Note that we can compute $V_{\tilde{n}}$ with the exact same method:

$$V_{\tilde{n}} = \int \frac{d^3x}{(2\pi)^3} \prod_{j=1}^{n} \iota_{k_j}(\boldsymbol{x}) \,, \tag{6.9}$$

with

$$\iota_{k_j}(\boldsymbol{x}) = \int_{k_j} d^3q e^{-i\boldsymbol{q}\cdot\boldsymbol{x}} \,. \tag{6.10}$$

In this paper, we shall implement Eq. (6.9) to study the performance of the parallel algorithm.

6.1.1 Dimensionality

At this point, a cautionary remark on the dimensionality of n-th order polygon is in order. While we only consider the 'angle averaged' polyspectra in this paper, specifying the full shape of n-point ($n \geq 3$) correlation function (or polyspectra, its Fourier counterpart) in the three-dimensional space would require $3n-6$ real numbers. It is because adding one more point to a configuration of $(n-1)$ points introduces three additional real numbers (the coordinate of the new point relative to the $n-1$ points) to specify the configuration of n points. Starting the recursion from bispectrum (or three-point correlation function) that requires three numbers, therefore, each configuration of n-point correlation function is specified by $3n-6$ real numbers.

This argument does not apply for the two-point function ($n=2$) and the three point function ($n=3$) because of the underlying symmetry. For the two-point correlation function, translational symmetry removes three (we can always set the coordinate of the first point as origin) and the rotational symmetry removes two (correlation function must be independent of the orientation of the second point) real dimensions. As a result, we are left with one real dimension for the power spectrum. For the three-point correlation function, the rotational symmetry around the axis defined by existing two points removes one real dimension. As a result, we are left with three real dimensions for the bispectrum.

Along the same reasoning, adding redshift-space distortion [51] would require only two more real dimensions to the problem, because the coordinate of the newly added point is enough to determine the orientation of the point relative to the existing $n-1$ points. That is, from the two angles specifying the orientation of any three points relative to the line-of-sight direction, we can determine the relative orientation of all other points with respect to the line-of-sight direction.

Although we shall not discuss further in this paper, one can also implement the

polyspectra estimator with the full dependence by using a similar method. For example, in addition to the amplitude of four wavevectors, the general trispectrum also depends on the diagonals $d_1 = |\mathbf{k}_1 - \mathbf{k}_2|$ and $d_2 = |\mathbf{k}_1 - \mathbf{k}_3|$, takes the form

$$\begin{aligned}
&T(k_1, k_2, k_3, k_4, d_1, d_2) \\
=&\frac{V_f}{V_T(2\pi)^3} \int_{k_1} d^3q_1 \cdots \int_{k_4} d^3q_4 \int_{d_1} d^3p_1 \int_{d_2} d^3p_2 \delta_D(\mathbf{q}_{1234}) \\
&\times \delta_D(\mathbf{p}_1 - \mathbf{q}_1 + \mathbf{q}_2)\delta_D(\mathbf{p}_2 - \mathbf{q}_1 + \mathbf{q}_3)\delta_{\mathbf{q}_1}\delta_{\mathbf{q}_2}\delta_{\mathbf{q}_3}\delta_{\mathbf{q}_4} \\
=&\frac{V_f}{V_T(2\pi)^3} \int \frac{d^3x}{(2\pi)^3} I_{k_4}(\boldsymbol{x}) \int \frac{d^3y}{(2\pi)^3} \iota_{d_2}(\boldsymbol{y}) I_{k_3}(\boldsymbol{x}+\boldsymbol{y}) \\
&\times \int \frac{d^3z}{(2\pi)^3} \iota_{d_1}(\boldsymbol{z}) I_{k_1}(\boldsymbol{x}-\boldsymbol{z}-\boldsymbol{y}) I_{k_2}(\boldsymbol{x}+\boldsymbol{z})\,. \qquad (6.11)
\end{aligned}$$

One may use, again, Fourier transformation to calculate the double convolution. Note that the result must reduce to the angle averaged trispectrum when integrating over all possible d_1 and d_2.

6.2 Parallelization

The key to the efficient parallelization of the polyspectra estimator is minimizing the inter-CPU communication, and we achieve that by using the slab decomposition scheme.

The slab decomposition slices the data cube along a single dimension, generally the fastest varying index, and assigns each chunk to different process. As each process stores a full range of other dimensions and limited range of the sliced dimension, this separates the data into 'slabs' of the domain hence the name slab decomposition. We show a visualization of this decomposition in Fig. 6.1. For the specific case of the polyspectra estimator, this decomposition takes the form of decomposing along the fastest varying Fourier grid dimension while the other two grid dimensions and the wavenumber dimension remain fully accessible in each process. For example, for the Julia implementation, we assign each process $\tilde{I}_{k_i}(k_{1\mathrm{min}} : k_{1\mathrm{max}}, k_\mathrm{F} : k_\mathrm{max}, k_\mathrm{F} : k_\mathrm{max})$, and for C implementation, we assign each process $\tilde{I}_{k_i}(k_\mathrm{F} : k_\mathrm{max}, k_\mathrm{F} : k_\mathrm{max}, k_{3\mathrm{min}} : k_{3\mathrm{max}})$ for all i from 1 to N_max. As the arrays $\tilde{I}_{k_i}(\boldsymbol{k})$ are zero except for the shell defined as $|\boldsymbol{k}| \sim k_i$, for which we assign the value from the original data cube $\delta(\boldsymbol{k})$, generating N_max of N_max^3-cube arrays takes only the time that we read through the original data cube. That is, at no point does the generating process need more than a single slab of data at once in memory.

This memory distribution is also natural for the Fourier transformation as FFTW [122]

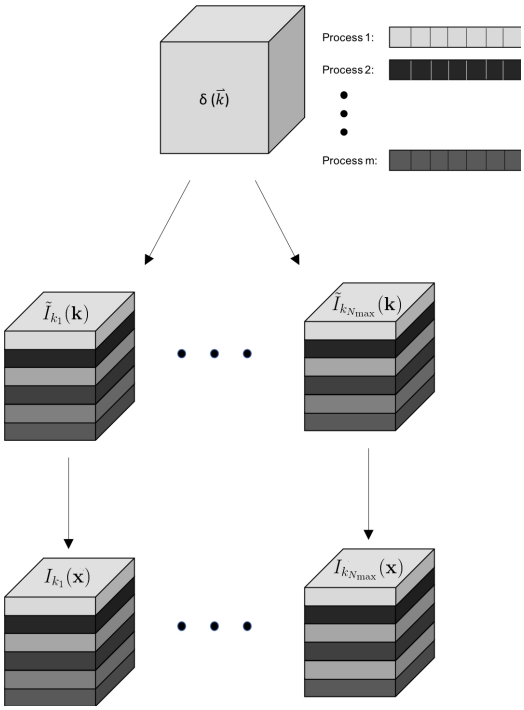

Figure 6.1. A visualization of the decomposition scheme. From the Fourier space density contrast field $\delta(\boldsymbol{k})$, we construct $N_{\max}$ Fourier data cubes $\tilde{I}_{k_i}(\boldsymbol{k})$ for $i = 1$ to $N_{\max}$ and distribute the array to m different processes depicted as different gray scale colors. The data cubes $\tilde{I}_{k_i}(\boldsymbol{k})$ are spread out over each process such that each one only has access to a single contiguous chunk of one index and the full range of the others. For example, the first process stores $\tilde{I}_{k_i}(k_F : k_{1\max}, k_F : k_{\max}, k_F : k_{\max})$ from all $\tilde{I}_{k_1}$ to $\tilde{I}_{k_{N_{\max}}}$. In this distribution scheme, the integration in Eq. (6.7) is done mostly in each local process, and the inter-CPU communication is only required at the last moment when we compute the total sum.

implements distributed Fourier transforms through slab decomposition and transposing, allowing for a very natural calculation without need to shuffle around memory between processes to get the right format. The only other step in the calculation is the product and sum, the product is always able to be done locally within each process and the sum is a trivially parallizable calculation with very little extra memory usage or communication as each processes calculates a local sum before the main processes collects and finalizes the sum. All together this memory distribution scheme allows us to easily and quickly calculate this estimator with minimal memory footprint and very little inter-CPU communication.

This method must be contrasted with the naïve parallelization that each process contains the full $\tilde{I}_{k_i}(\boldsymbol{k})$ and $I_{k_i}(\boldsymbol{x})$ for each wavenumber bin k_i. For this alternative case,

however, the time saved in the Fourier transform step is dwarfed by the significantly more expensive final step where we calculate sums of products across wavenumbers. As a result, this somewhat more natural decomposition is significantly slower than the slab decomposition.

6.3 Code Tests

In order to test the accuracy and performance of our implementation of the parallel estimator, we compute the number of polygons satisfying the homogeneity condition and the binning condition:

$$\begin{aligned} N_{n-\mathrm{poly}} =& \frac{V_{\tilde{n}}}{V_f^{n-1}} \\ =& \frac{1}{k_F^{3n-3}} \int_{k_1} d^3q_1 \cdots \int_{k_n} d^3q_n \delta_D(\mathbf{q}_{1\cdots n}), \end{aligned} \tag{6.12}$$

for which we have present an analytical estimation (see Sec. 6.3.1 for the detail). Here, V_f is the volume of the fundamental cell in the Fourier space, which is related to the fundamental Fourier wavenumber k_F by $V_f = k_F^3$.

In practice, we estimate the number of polygons by setting $\delta(\boldsymbol{k}) = 1$ for all Fourier modes and estimating the angle-averaged polyspectra. Therefore, counting the number of polygons requires exactly the same procedure as estimating the polyspectra.

6.3.1 Number of Polygons

To obtain the number of n-gons satisfying the binning conditions, we need to evaluate the $3n$-dimensional integration in Eq. (6.12). Again, using the Fourier representation of the Dirac-delta operator, we reduce the problem to the three-dimensional integration of multiplications of $\iota_k(\boldsymbol{x})$ (Eq. (6.9)), which is

$$\iota_k = \int_k d^3q e^{i\boldsymbol{q}\cdot\boldsymbol{x}} = 4\pi k^2 \left(\frac{\sin(kx)}{kx}\right) \delta k + \mathcal{O}(\delta k^3)\,. \tag{6.13}$$

Using the expression to leading order in the bin size δk, we further reduce the calculation of the $3n$-dimensional volume to the one-dimensional integration:

$$V_{\tilde{n}} = \int \frac{d^3x}{(2\pi)^3} \prod_{i=1}^{n} \iota_{k_i}(x)$$

$$=(4\pi\delta k)^n \int_0^\infty \frac{dx}{2\pi^2 x^{n-2}} \prod_{i=1}^{n} k_i \sin(k_i x)\,. \tag{6.14}$$

In App. E, We find a general expression for the radial integration,

$$\int_0^\infty \frac{dx}{x^{n-2}} \prod_{i=1}^{n} \sin(k_i x) = \frac{\pi}{2} \left(\prod_{i=3}^{n} \int_{-k_i}^{k_i} \frac{d\kappa_i}{2} \right) \times \left[\delta^D \left(\sum_{i=3}^{n} \kappa_i + k_1 - k_2 \right) - \delta^D \left(\sum_{i=3}^{n} \kappa_i - k_1 - k_2 \right) \right], \tag{6.15}$$

and apply Eq. (6.15) for $n = 3$ and $n = 4$ cases to find the number of triangles and quadrilaterals, which are given by

$$N_{\rm tri} = \frac{1}{k_F^6} \begin{cases} 4\pi^2 k_1 k_2 k_3 \left(\delta k\right)^3 & ,\ k_1 = k_2 + k_3 \\ 8\pi^2 k_1 k_2 k_3 \left(\delta k\right)^3 & ,\ k_1 < k_2 + k_3 \end{cases}, \tag{6.16}$$

and

$$N_{\rm quad} = \frac{1}{k_F^9} 8\pi^3 \left(\delta k\right)^4 k_1 k_2 k_3 k_4 (-k_1 + k_2 + k_3 + 3k_4 - |k_1 - k_2 - k_3 + k_4|)\,. \tag{6.17}$$

6.3.2 Results

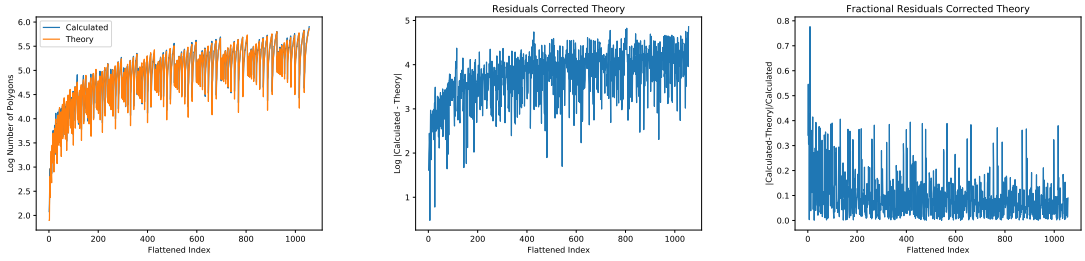

Figure 6.2. *Left*: The number of triangles satisfying the binning conditions measured from the parallel bispectrum estimator. The blue curve is the output from the numerical estimation, and the orange curve is according to our analytical estimation in Eq. (6.16) (see App. E for the derivation). *Middle*: The difference between the numerical measurement and theoretical estimation. *Right:* The fractional difference between the two. Besides the largest-scales (earlier indices) that we expect the analytical estimation breaks down, the analytical estimation in Eq. (6.16) is good to about 20 % accuracy.

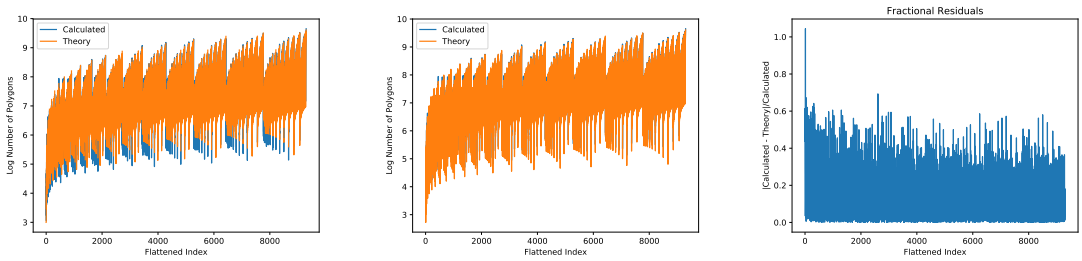

Figure 6.3. *Left*: The number of quadrilaterals satisfying the binning conditions measured from the parallel trispectrum estimator. The blue curve is the output from the numerical estimation, and the orange curve is according to our analytical estimation in Eq. (6.17). *Middle*: The same numerical result (blue) along with the improved analytical calculation, using exact expression for $\iota_k(x)$ (see, Eq. (E.27)) and calculate the correction for the co-linear quadrilaterals as in Eq. (E.29). *Right*: The fractional difference between the two curves in the middle panel. The small-scale (large wavenumber) discrepancies are consistently about 40 %.

In this section, we shall present number of polygons that we calculated using the parallelized polyspectra estimator and compare the result with the analytical estimation that we find in Sec. 6.3.1. We shall show the result for triangles ($n = 3$), quadrilaterals ($n = 4$), pentagons ($n = 5$), and hexagons ($n = 6$) that are estimated using, respectively, the parallel estimators of bispectrum, trispectrum, quadspectrum, and pentaspectrum.

To show the full shape dependence of the number of polygons as a function of their side length (wavenumbers), we need to visualize them in n-dimensional space of $(k_1, k_2, \cdots, k_n)$. For our purpose, however, to compare the outcome of the parallel computation and analytical estimation, it suffices to flatten n-dimensional data points to the one-dimensional ordered sequence. Following the convention in [80], we impose the condition $k_i \geq k_{i+1}$ to avoid duplication and form the sequence by taking the row-major order of the n-dimensional points (k_n is the fastest varying dimension).

In all comparison plots that we present here, the x axes show the index of the n-dimensional point $(k_1, \cdots, k_n)$ in the flattened sequence, and y axes show the number of polygons whose n sides are $(k_1, \cdots, k_n)$. We use blue color to show the numerical result and orange color to show the analytical estimation.

First, we show the number of triangles using the parallel bispectrum estimator in Fig. 6.2. The left panel shows the numerical result (blue) and analytical prediction (Eq. (6.16)), while the middle and right panels show the absolute number (middle) and fractional (right) differences. On large scales (or small indices), we expect the analytical estimation is not accurate because the bin's size is of order the wavenumber ($k_i \simeq \delta k$). For small scales, although the absolute residuals increases with wavenumbers (the lowest

order error term goes as $\prod k_i$ just like the $N_{\rm tri}$ in Eq. (6.16)), the fractional residual between the numerical and analytical estimation are consistently off by $10 \sim 20\%$, and the biggest differences happen for the folded triangles ($k_1 = k_2 + k_3$). This result suggests that the variance of bispectrum estimated by using Eq. (6.16) (for example, in the Fisher information forecast in Ref. [3]) must be off by the same factor. For an accurate estimation of the variance of the bispectrum, one must use the numerically estimated number of triangles.

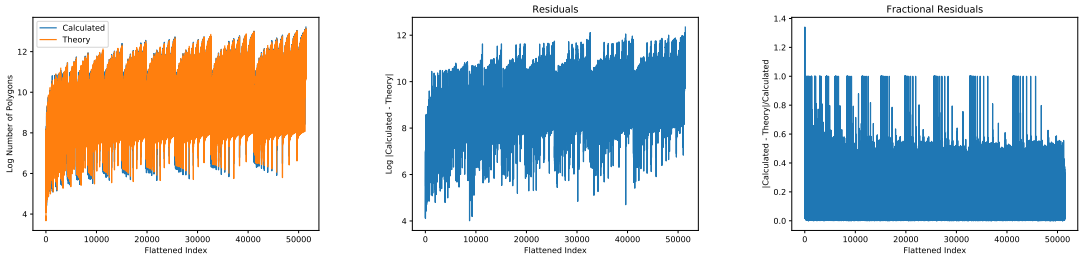

Figure 6.4. The flattened number of pentagons/Angle Averaged Quadspectrum of unity. The orange is according to the number predicted by App. E and the blue curve is the output of the estimator run on a grid of unity on a spherical shell. The Quadspectrum shows very similar error behaviour to the Trispectrum and for much the same reasons cannot be practically used when calculating actual Quadspectrum.

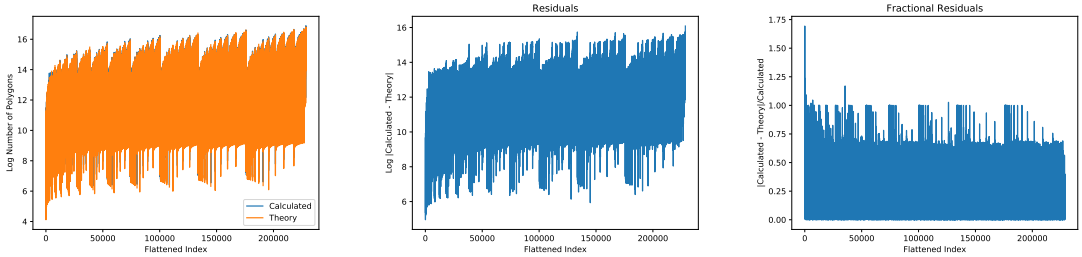

Figure 6.5. The flattened number of hexagons/Angle Averaged Pentaspectrum of unity. The orange is according to the number predicted by App. E and the blue curve is the output of the estimator run on a grid of unity on a spherical shell. The Pentaspectrum displays near identical error behaviour to the other high order polyspectra.

We perform the same analysis for the number of quadraliterals by using the parallel estimator for trispectrum. The left panel of Fig. 6.3 shows the comparison between the numerical result and the analytical estimation in Eq. (6.17). It turns out that biggest the discrepancies are for the co-linear quadrilaterals ($k_1 = k_2 + k_3 + k_4$) where the analytical formula, Eq. (6.17), predicts zero. To remedy the situation, we add the exact corrections for the co-linear quadrilaterals, Eq. (E.29), and the analytical estimate indeed matches the numerical calculation better, as shown in the middle panel of Fig. 6.3.

We can easily extend the parallel estimator for the bispectrum and trispectrum to measure any $n > 4$ polyspectra. We extend the estimator to $n = 5$ and $n = 6$ order polyspectra, and show the result in Fig. 6.4 and Fig. 6.5, respectively. In all cases the fractional errors between numerical calculation and analytical estimate are dominated by a collection of 100% error terms. These occur, just as the co-linear case for the quadrilaterals, because the leading-order approximation in the analytical calculation yields zeros when the actual calculation yields small but not-zero numbers. This happens for all $n > 4$ cases, and it further reinforces the need for manually calculating the number of polygons when estimating the polyspectra, or estimating their variance.

6.3.3 Code Performance

In this section, we present the performance of the parallel algorithm. All of our benchmarking work was done with 2.2 GHz Intel Xeon Processors on nodes with 40 CPU/node, 1 TB of RAM, 10 Gbps Ethernet and FDR Infiniband.

We have implemented two versions of parallel bispectrum estimator, one using C and the other using Julia. These two pieces of software perform the same algorithm. In Fig. 6.6, we compare the performance of the two implementations. Overall, as a function of domain length, the size of one-dimensional Fourier grid N and the maximum wavenumber $N_{\rm max} = k_{\rm max}/k_F$, the performance scales as $\mathcal{O}(N^3 N_{\rm max}^n)$, as we have analyzed in Sec. 6. If we apply the aliasing condition which requires that $N > nN_{\rm max}$ we can rewrite the scaling as $\mathcal{O}(n^3 N_{\rm max}^{n+3})$.

The C implementation (blue) out performs the Julia implementation (orange) for all domain lengths. The improvement, however, stays constant at about 30 seconds offset for reasonable grid sizes. As it is easier to read and modify the Julia version, we have extended the software to higher order polyspectra estimator only using Julia.

Fig. 6.7 shows the performance of our Julia implementation as a function of number of processors. Here, we use the domain size of $N = 256$ (left panel) and $N = 512$ (right panel). Initially, adding more CPUs improves the performance and reduces the execution time, but the improvement stops at some point. In fact, when the grid size per CPU is sufficiently small then adding more processes actually slows down the performance; the increased overhead time cancels the small gains in extra discretization.

How long does it take to estimate the bispectrum? In order to avoid the aliasing effect, the grid size must satisfy $N > 3N_{\rm max}$ for estimating the bispectrum. Therefore, probing the bispectrum up to $N_{\rm max} \simeq 340$ requires the one-dimensional Fourier grid of $N = 1024$; we can estimate the bispectrum in 20 minutes using 40 cores.

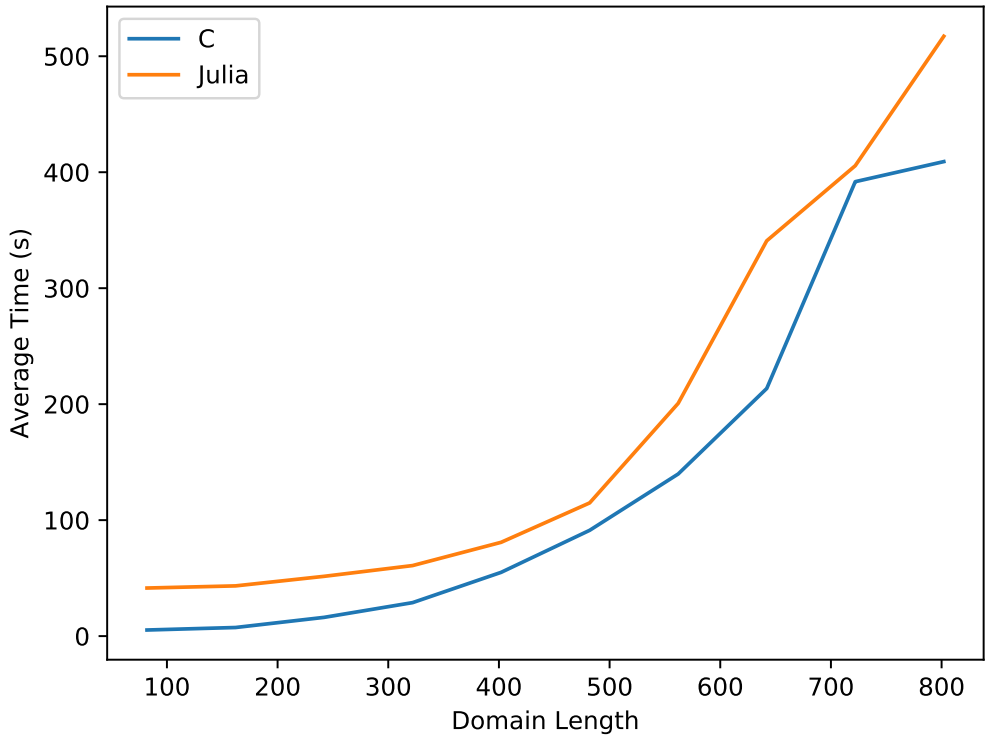

Figure 6.6. The total time spent calculating the Bispectrum versus the length of one grid dimension for 40 processors. It roughly follows the $\mathcal{O}(N^3)$ you would expected given the sum in the algorithm with fixed $N_{\max}$, modulo the overhead dominated small grid sizes. Each grid size was tested 50 times and then averaged. While the Julia version is slightly slower than the C version, the time difference is relatively consistent with around a constant 30 second offset for small grid sizes and is mostly negligible for large grid sizes given the overall length of the computation.

For a more concrete example, the HETDEX survey [123] has $k_F \approx 0.0045\ h/\text{Mpc}$. Measuring the galaxy bispectrum to $k_{\max} = 0.2\ h/\text{Mpc}$ only requires $N_{max} = 45$. With the parallel version of Scoccimarro estimator, we can measure the galaxy bispectrum for HETDEX in ∼40 seconds with 2 GB of memory distributed over 40 processors. Here, we did not run the in-place FFTW, and kept both $I_{k_i}(\boldsymbol{x})$ and $\tilde{I}_{k_i}(\boldsymbol{q})$. Similarly, WFIRST [124] has $k_F \approx 0.0028\ h/\text{Mpc}$ corresponding to $N_{\max} = 75$ for $k_{\max} = 0.2\ h/\text{Mpc}$. For our implementation over 40 processors this corresponds to ∼50 seconds and 11 GB of memory distributed over 40 processors to calculate the galaxy bispectrum for WFIRST.

With the scaling that we have discussed in Sec. 6, we can extend the previous example to find a general relationship. For a cosmological survey with volume V and maximum

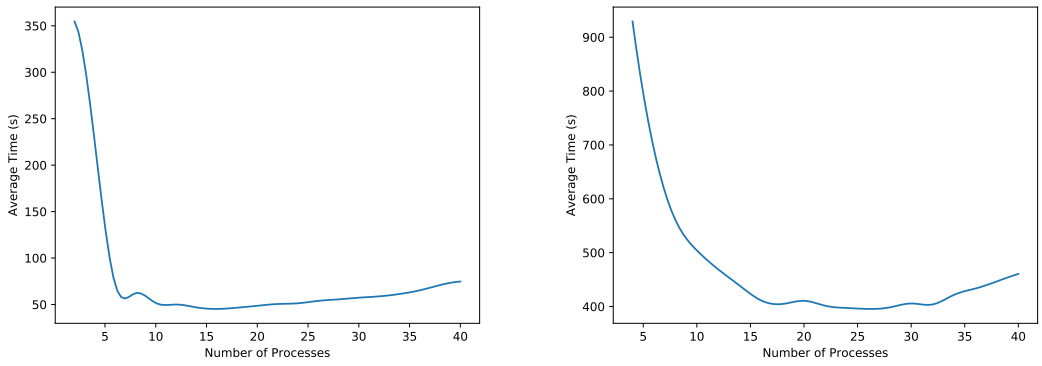

Figure 6.7. Left: The scaling of an N=256 length grid over various numbers of processes. There is clear gains when initially increasing the number of processes but at a certain point overhead begins to dominate causing a slight slowdown. Right: The scaling of an N=512 length grid over various numbers of processes. It takes more processes to reach the top speed, and the relative speedup between the maximum and the $N_{\rm cpu} = 4$ case is only a factor of 2 compared to the factor of 4 for the $N = 256$ case. This is because the overhead scales very poorly with the grid size. Each number of processes was tested 50 times and then averaged.

wavenumber $k_{\rm max}$, we calculate the number of one-dimensional sampling point as

$$N_{\rm max} = \frac{k_{\rm max}}{k_F} = \frac{1}{2\pi} k_{\rm max} V^{1/3} \,. \tag{6.18}$$

Because the performance of the Scoccimarro estimator scales as $\mathcal{O}(N_{\rm max}^6)$, the estimated computing time becomes

$$t_{Bispec} \approx 40 \left(\frac{k_{\rm max}}{0.2h/{\rm Mpc}} \right)^6 \left(\frac{V}{2.7\ {\rm Gpc}^3/h^3} \right)^2 {\rm sec}, \tag{6.19}$$

over 40 processors. For the higher-order polyspectra, we can extend this relationship by

$$t_{Pn} \sim \frac{n^3}{27} \left(\frac{k_{\rm max}}{0.2h/{\rm Mpc}} \right)^{n+3} \left(\frac{V}{2.7\ {\rm Gpc}^3/h^3} \right)^{(n+3)/3} {\rm min}, \tag{6.20}$$

again, over the 40 processors. This relationship matches with the execution time for the polyspectra that we have measured for generating the figures in this paper.

Appendix A
Mathematical Identities

We make use of the following identities throughout the work. Most of these expressions come directly from either [64] App. C or [71] App. A. The Dirac delta expands into plane waves as

$$\delta_D(\boldsymbol{q}) = \int_{\boldsymbol{r}} e^{i\boldsymbol{q}\cdot\boldsymbol{r}}. \tag{A.1}$$

To decompose an exponential into spherical harmonics we use

$$e^{\pm ik\cdot r} = 4\pi \sum_{\ell=0}^{\infty} \sum_{m=-\ell}^{\ell} (\pm i)^{\ell} j_{\ell}(kr) Y_{\ell m}(\hat{\boldsymbol{k}}) Y^*_{\ell m}(\hat{\boldsymbol{r}}). \tag{A.2}$$

To decompose a Legendre polynomial into spherical harmonics we use

$$\mathcal{L}_{\ell}(\hat{\boldsymbol{q}}\cdot\hat{\boldsymbol{k}}) = \frac{4\pi}{2\ell+1} \sum_{m=-\ell}^{\ell} Y_{\ell m}(\hat{\boldsymbol{q}}) Y^*_{\ell m}(\hat{\boldsymbol{k}}). \tag{A.3}$$

The spherical harmonic convention we use is

$$Y^*_{\ell m}(\hat{\boldsymbol{k}}) = (-1)^m Y_{\ell -m}(\hat{\boldsymbol{k}}). \tag{A.4}$$

The Gaunt integral is defined as

$$\begin{aligned} \mathcal{G}^{m_1 m_2 m_3}_{l_1 l_2 l_3} &= \int d\Omega Y_{l_1 m_1}(\hat{\boldsymbol{k}}) Y_{l_2 m_2}(\hat{\boldsymbol{k}}) Y_{l_3 m_3}(\hat{\boldsymbol{k}}) \\ &= \sqrt{\frac{(2l_1+1)(2l_2+1)(2l_3+1)}{4\pi}} \begin{pmatrix} l_1 & l_2 & l_3 \\ 0 & 0 & 0 \end{pmatrix} \begin{pmatrix} l_1 & l_2 & l_3 \\ m_1 & m_2 & m_3 \end{pmatrix}. \end{aligned} \tag{A.5}$$

To combine the product of two spherical harmonics into a single spherical harmonic we use

$$Y_{l_1 m_1}(\hat{\boldsymbol{k}}) Y_{l_2 m_2}(\hat{\boldsymbol{k}}) = \sum_{L=|l_1-l_2|}^{l_1+l_2} (-1)^{m_1+m_2} \mathcal{G}_{l_1 l_2 L}^{m_1, m_2, -m_1-m_2} Y_{L m_1+m_2}(\hat{\boldsymbol{k}}). \tag{A.6}$$

We use the definition of the Wigner-6j symbol from [125, Eq. 35.5.23]

$$\begin{aligned}
&(-1)^{l_1+l_2+l_3} \begin{Bmatrix} \ell_1 & \ell_2 & \ell_3 \\ l_1 & l_2 & l_3 \end{Bmatrix} \begin{pmatrix} \ell_1 & \ell_2 & \ell_3 \\ m_1 & m_2 & m_3 \end{pmatrix} \\
&= \sum_{m_1' m_2' m_3'} (-1)^{m_1'+m_2'+m_3'} \begin{pmatrix} \ell_1 & l_2 & l_3 \\ m_1 & m_2' & -m_3' \end{pmatrix} \\
&\times \begin{pmatrix} l_1 & \ell_2 & l_3 \\ -m_1' & m_2 & m_3' \end{pmatrix} \begin{pmatrix} l_1 & l_2 & \ell_3 \\ m_1' & -m_2' & m_3 \end{pmatrix},
\end{aligned} \tag{A.7}$$

and the orthogonality of the Wigner-3j symbols

$$\sum_{m_1 m_2} (2l+1) \begin{pmatrix} l_1 & l_2 & l \\ m_1 & m_2 & m \end{pmatrix} \begin{pmatrix} l_1 & l_2 & l' \\ m_1 & m_2 & m' \end{pmatrix} = \delta_{ll'} \delta_{mm'} \tag{A.8}$$

Appendix B
$P_{13}^{gg,s}$ Bias Coefficient Matrices: $\boldsymbol{\mathcal{M}}(\mathcal{O})$

Here we merely state the matrices. For a derivation see Ref. [4] App F.

$$\boldsymbol{\mathcal{M}}\left(O_{td}\right) = \frac{1}{7}\begin{bmatrix} 4 & -6 & 2 & 0 & 0 \\ 0 & 0 & 0 & 0 & 0 \\ 0 & 0 & 0 & 0 & 0 \end{bmatrix}$$

$$\boldsymbol{\mathcal{M}}\left(\delta\Pi_{\parallel}^{[2]}\right) = \frac{1}{7}\begin{bmatrix} 0 & 0 & 5 & -5 & 0 \\ 0 & 0 & -15 & 15 & 0 \\ 0 & 0 & 0 & 0 & 0 \end{bmatrix}$$

$$\boldsymbol{\mathcal{M}}\left(f^{-1}\eta\Pi_{\parallel}^{[2]}\right) = \frac{1}{7}\begin{bmatrix} 0 & 0 & -\frac{15}{4} & \frac{15}{2} & -\frac{15}{4} \\ -5 & \frac{15}{2} & 20 & -60 & \frac{75}{2} \\ 5 & -\frac{15}{2} & -\frac{65}{4} & \frac{125}{2} & -\frac{175}{4} \end{bmatrix}$$

$$\boldsymbol{\mathcal{M}}\left((\Pi^{[2]}K)_{\parallel}\right) = \frac{1}{7}\begin{bmatrix} \frac{5}{4} & -\frac{15}{8} & \frac{35}{24} & -\frac{5}{6} & 0 \\ \frac{5}{4} & -\frac{15}{8} & -\frac{15}{8} & \frac{5}{2} & 0 \\ 0 & 0 & 0 & 0 & 0 \end{bmatrix}$$

$$\boldsymbol{\mathcal{M}}\left(f^{-1}u_{\parallel}^{(2)}\partial_{\parallel}\delta\right) = \frac{1}{7}\begin{bmatrix} 0 & 0 & 3 & -3 & 0 \\ 0 & -3 & -6 & 9 & 0 \\ 0 & 0 & 0 & 0 & 0 \end{bmatrix}$$

$$\boldsymbol{\mathcal{M}}\left(f^{-2}u_{\parallel}^{(2)}\partial_{\parallel}\eta\right) = \frac{1}{7}\begin{bmatrix} 0 & 0 & -\frac{9}{4} & \frac{9}{2} & -\frac{9}{4} \\ -\frac{9}{4} & \frac{27}{8} & \frac{63}{8} & -\frac{63}{2} & \frac{45}{2} \\ \frac{15}{4} & -\frac{21}{8} & -\frac{39}{8} & 30 & -\frac{105}{4} \end{bmatrix}$$

$$
\begin{aligned}
\boldsymbol{\mathcal{M}}\left(s^k\partial_k\Pi^{[2]}_{\parallel}\right) &= \frac{1}{7}\begin{bmatrix} \frac{5}{4} & -\frac{15}{8} & \frac{25}{8} & -\frac{5}{2} & 0 \\ -\frac{15}{4} & \frac{45}{8} & -\frac{75}{8} & \frac{15}{2} & 0 \\ 0 & 0 & 0 & 0 & 0 \end{bmatrix} \\
\boldsymbol{\mathcal{M}}\left(f^{-1}u_{\parallel}\partial_{\parallel}\Pi^{[2]}_{\parallel}\right) &= \frac{1}{7}\begin{bmatrix} 0 & 0 & \frac{15}{4} & -\frac{15}{2} & \frac{15}{4} \\ \frac{15}{4} & -\frac{45}{8} & -\frac{225}{8} & \frac{135}{2} & -\frac{75}{2} \\ -\frac{25}{4} & \frac{75}{8} & \frac{225}{8} & -75 & \frac{175}{4} \end{bmatrix} \\
\boldsymbol{\mathcal{M}}\left(\Pi^{[3]_{\parallel}}\right) &= \frac{1}{7}\begin{bmatrix} \frac{13}{8} & -\frac{39}{16} & \frac{65}{16} & -\frac{13}{4} & 0 \\ -\frac{101}{24} & \frac{101}{16} & -\frac{569}{48} & \frac{39}{4} & 0 \\ 0 & 0 & 0 & 0 & 0 \end{bmatrix} \\
\boldsymbol{\mathcal{M}}\left(\delta^{(3)}\right) &= \frac{1}{7}\begin{bmatrix} \frac{2}{3} & \frac{1}{2} & -\frac{7}{6} & 0 & 0 \\ 0 & 0 & 0 & 0 & 0 \\ 0 & 0 & 0 & 0 & 0 \end{bmatrix} \\
\boldsymbol{\mathcal{M}}\left(f^{-1}\eta^{(3)}\right) &= \frac{1}{7}\begin{bmatrix} 0 & 0 & 0 & 0 & 0 \\ -2 & \frac{3}{2} & \frac{1}{2} & 0 & 0 \\ 0 & 0 & 0 & 0 & 0 \end{bmatrix}.
\end{aligned} \tag{B.1}
$$

Note that the above matrix for $f^{-1}\eta^{(3)}$ has had a typo fixed from Ref. [4], replacing 2 and $-\frac{1}{2}$ with -2 and $\frac{1}{2}$ respectively. We also use

$$
\begin{aligned}
\boldsymbol{\mathcal{M}}\left(2KK^{(2)}\right) &= \frac{5}{2}\boldsymbol{\mathcal{M}}\left(O_{td}\right) \\
\boldsymbol{\mathcal{M}}\left(f^{-1}\delta\eta^{(2)}\right) &= -\frac{3}{5}\boldsymbol{\mathcal{M}}\left(\delta\Pi^{[2]}_{\parallel}\right) \\
\boldsymbol{\mathcal{M}}\left(f^{-1}u_{\parallel}\partial_{\parallel}\eta^{(2)}\right) &= -\frac{3}{5}\boldsymbol{\mathcal{M}}\left(u_{\parallel}\partial_{\parallel}\Pi^{[2]}_{\parallel}\right) \\
\boldsymbol{\mathcal{M}}\left(2f^{-2}\eta\eta^{(2)}\right) &= -\frac{6}{5}\boldsymbol{\mathcal{M}}\left(\eta\Pi^{[2]}_{\parallel}\right) \\
\boldsymbol{\mathcal{M}}\left(2(KK^{(2)})_{\parallel}\right) &= 2\boldsymbol{\mathcal{M}}\left((\Pi^{[2]}K)_{\parallel}\right).
\end{aligned} \tag{B.2}
$$

Appendix C
New P_{22} Integrals

Unfortunately the integral forms of $P_{22}^{gg,s}(k,\mu)$ from [4], when converted into radial integrals, lead to combinations of divergent integrals that we assume have some canceling divergences but are numerically problematic. To avoid this issue we need to consider a much earlier version of the form of $P_{22}^{gg,s}$ that looks more like

$$P_{22}^{gg,s}(k,\mu) = 2\int_{\boldsymbol{q}}[Z_2(\boldsymbol{q},\boldsymbol{k}-\boldsymbol{q})]^2 P_L(q)P_L(|\boldsymbol{k}-\boldsymbol{q}|), \tag{C.1}$$

where Z_2 is the bias kernel corresponding to all appropriate parameters, for more discussion of the kernel see Sec. 4.1. When considering this form we get integrals like

$$(2\pi)^3\int_{\boldsymbol{q}}\int_{\boldsymbol{p}} q^{n_1-2}p^{n_2-2}\delta_D(\boldsymbol{p}+\boldsymbol{q}-\boldsymbol{k})P_L(q)P_L(p)\left(\hat{\boldsymbol{n}}\cdot\hat{\boldsymbol{q}}\right)^a\left(\hat{\boldsymbol{n}}\cdot\hat{\boldsymbol{p}}\right)^b\left(\hat{\boldsymbol{p}}\cdot\hat{\boldsymbol{q}}\right)^c, \tag{C.2}$$

which we can write as Legendre polynomials like

$$\mathcal{I}^{n_1n_2}_{a'b'c'} = (2\pi)^3\int_{\boldsymbol{q}}\int_{\boldsymbol{p}} q^{n_1-2}p^{n_2-2}\delta_D(\boldsymbol{p}+\boldsymbol{q}-\boldsymbol{k})P_L(q)P_L(p)\mathcal{L}_{a'}\left(\hat{\boldsymbol{n}}\cdot\hat{\boldsymbol{q}}\right)\mathcal{L}_{b'}\left(\hat{\boldsymbol{n}}\cdot\hat{\boldsymbol{p}}\right)\mathcal{L}_{c'}\left(\hat{\boldsymbol{p}}\cdot\hat{\boldsymbol{q}}\right). \tag{C.3}$$

Then expanding the dirac delta into plane waves, Eq. (A.1), and decomposing into angular and radial components

$$\mathcal{I}^{n_1n_2}_{a'b'c'} = (2\pi)^3\int\frac{dr}{2\pi^2}r^2\int\frac{dq}{2\pi^2}q^2q^{n_1-2}\int\frac{dp}{2\pi^2}p^2p^{n_2-2}P_L(q)P_L(p)I_{a'b'c'}, \tag{C.4}$$

where

$$I_{a'b'c'} = \int\frac{d\Omega_r}{4\pi}\int\frac{d\Omega_q}{4\pi}\int\frac{d\Omega_p}{4\pi}e^{i(\boldsymbol{p}+\boldsymbol{q}-\boldsymbol{k})\cdot\boldsymbol{r}}\mathcal{L}_{a'}(\hat{\boldsymbol{n}}\cdot\hat{\boldsymbol{q}})\mathcal{L}_{b'}(\hat{\boldsymbol{n}}\cdot\hat{\boldsymbol{p}})\mathcal{L}_{c'}(\hat{\boldsymbol{p}}\cdot\hat{\boldsymbol{q}}), \tag{C.5}$$

is the angular part of the integral. We can write this in spherical harmonic form using Eq. (A.3)

$$I_{a'b'c'} = \sum_{m_a=-a'}^{a'} \sum_{m_b} \sum_{m_c} \int \frac{d\Omega_r}{4\pi} \int \frac{d\Omega_q}{4\pi} \int \frac{d\Omega_p}{4\pi} e^{-ik\cdot r} \left(\frac{4\pi}{2a'+1} Y_{a'm_a}(\hat{\boldsymbol{q}}) Y^*_{a'm_a}(\hat{\boldsymbol{n}}) e^{iq\cdot r} \right) \times \left(\frac{4\pi}{2b'+1} Y_{b'm_b}(\hat{\boldsymbol{p}}) Y^*_{b'm_b}(\hat{\boldsymbol{n}}) e^{ip\cdot r} \right) \left(\frac{4\pi}{2c'+1} Y_{c'm_c}(\hat{\boldsymbol{p}}) Y^*_{c'm_c}(\hat{\boldsymbol{q}}) \right). \tag{C.6}$$

Which we denote

$$I_{a'b'c'} = \frac{1}{(2a'+1)(2b'+1)(2c'+1)} \mathcal{A}_{a'b'c'}, \tag{C.7}$$

to simplify future notation. We then expand some of the exponentials in $\mathcal{A}$ in terms of spherical harmonics using Eq. (A.2) and then factor into separate angular parts to get

$$\mathcal{A}_{a'b'c'} = (4\pi)^2 \sum_{m_a m_b m_c} \sum_{\ell_a=0}^{\infty} \sum_{m_{\ell a}=-\ell_a}^{\ell_a} \sum_{\ell_b, m_{\ell b}} \int d\Omega_r \, e^{-ik\cdot r} i^{\ell_a+\ell_b} Y^*_{\ell_a m_{\ell a}}(\hat{\boldsymbol{r}}) Y^*_{\ell_b m_{\ell b}}(\hat{\boldsymbol{r}}) Y^*_{a'm_a}(\hat{\boldsymbol{n}}) Y^*_{b'm_b}(\hat{\boldsymbol{n}}) \times j_{\ell_a}(qr) j_{\ell_b}(pr) \int d\Omega_q \, Y_{a'm_a}(\hat{\boldsymbol{q}}) Y_{\ell_a m_{\ell a}}(\hat{\boldsymbol{q}}) Y^*_{c'm_c}(\hat{\boldsymbol{q}}) \int d\Omega_p \, Y_{b'm_b}(\hat{\boldsymbol{p}}) Y_{\ell_b m_{\ell b}}(\hat{\boldsymbol{p}}) Y_{c'm_c}(\hat{\boldsymbol{p}}). \tag{C.8}$$

Which we can simplify using the Gaunt integral, Eq. (A.5), to get

$$\mathcal{A}_{a'b'c'} = (4\pi)^2 \sum_{m_a m_b m_c \ell_a \ell_b m_{\ell a} m_{\ell b}} \int d\Omega_r \, e^{-ik\cdot r} (-1)^{m_c} i^{\ell_a+\ell_b} Y^*_{\ell_a m_{\ell a}}(\hat{\boldsymbol{r}}) Y^*_{\ell_b m_{\ell b}}(\hat{\boldsymbol{r}}) Y^*_{a'm_a}(\hat{\boldsymbol{n}}) Y^*_{b'm_b}(\hat{\boldsymbol{n}}) \times \mathcal{G}^{m_a, m_{\ell a}, -m_c}_{a'\ell_a c'} \mathcal{G}^{m_b, m_{\ell b}, m_c}_{b'\ell_b c'} j_{\ell_a}(qr) j_{\ell_b}(pr). \tag{C.9}$$

Now we decompose the final exponential to get

$$\mathcal{A}_{a'b'c'} = (4\pi)^3 \sum_{m_a m_b m_c \ell_a \ell_b m_{\ell a} m_{\ell b}} \sum_{\ell_r=0}^{\infty} \sum_{m_r=-\ell_r}^{\ell_r} (-1)^{m_c} i^{\ell_a+\ell_b} j_{\ell_a}(qr) j_{\ell_b}(pr) \mathcal{G}^{m_a, m_{\ell a}, -m_c}_{a'\ell_a c'} \mathcal{G}^{m_b, m_{\ell b}, m_c}_{b'\ell_b c'} \times Y^*_{a'm_a}(\hat{\boldsymbol{n}}) Y^*_{b'm_b}(\hat{\boldsymbol{n}}) i^{-\ell_r} j_{\ell_r}(kr) Y^*_{\ell_r m_r}(\hat{\boldsymbol{k}}) \int d\Omega_r Y_{\ell_r m_r}(\hat{\boldsymbol{r}}) Y^*_{\ell_a m_{\ell a}}(\hat{\boldsymbol{r}}) Y^*_{\ell_b m_{\ell b}}(\hat{\boldsymbol{r}}), \tag{C.10}$$

which simplifies to

$$\mathcal{A}_{a'b'c'} = (4\pi)^3 \sum_{\ell_a \ell_b \ell_r} i^{\ell_a+\ell_b-\ell_r} j_{\ell_a}(qr) j_{\ell_b}(pr) j_{\ell_r}(kr) \sum_{m_a m_b m_r} Y^*_{a'm_a}(\hat{\boldsymbol{n}}) Y^*_{b'm_b}(\hat{\boldsymbol{n}}) Y^*_{\ell_r m_r}(\hat{\boldsymbol{k}}) \times \sum_{m_c m_{\ell a} m_{\ell b}} (-1)^{m_c+m_{\ell a}+m_{\ell b}} \mathcal{G}^{m_a, m_{\ell a}, -m_c}_{a'\ell_a c'} \mathcal{G}^{m_b, m_{\ell b}, m_c}_{b'\ell_b c'} \mathcal{G}^{m_r, -m_{\ell a}, -m_{\ell b}}_{\ell_r \ell_a \ell_b}. \tag{C.11}$$

Now we look specifically at the sum over the product of Gaunt integrals. Using Eq. (A.7)

$$
\begin{aligned}
&\sum_{m_c m_{\ell a} m_{\ell b}} (-1)^{m_c+m_{\ell a}+m_{\ell b}} \mathcal{G}^{m_a,m_{\ell a},-m_c}_{a'\ell_a c'} \mathcal{G}^{m_b,m_{\ell b},m_c}_{b'\ell_b c'} \mathcal{G}^{m_r,-m_{\ell a},-m_{\ell b}}_{\ell_r \ell_a \ell_b} \\
&= \frac{(2\ell_a+1)(2\ell_b+1)(2c'+1)\sqrt{(2\ell_r+1)(2a'+1)(2b'+1)}}{(4\pi)^{3/2}} \begin{pmatrix} a' & \ell_a & c' \\ 0 & 0 & 0 \end{pmatrix} \begin{pmatrix} b' & \ell_b & c' \\ 0 & 0 & 0 \end{pmatrix} \begin{pmatrix} \ell_r & \ell_a & \ell_b \\ 0 & 0 & 0 \end{pmatrix} \\
&\times \sum_{m_c m_{\ell a} m_{\ell b}} (-1)^{m_c+m_{\ell a}+m_{\ell b}} \begin{pmatrix} a' & \ell_a & c' \\ m_a & m_{\ell a} & -m_c \end{pmatrix} \begin{pmatrix} b' & \ell_b & c' \\ m_b & m_{\ell b} & m_c \end{pmatrix} \begin{pmatrix} \ell_r & \ell_a & \ell_b \\ m_r & -m_{\ell a} & -m_{\ell b} \end{pmatrix} \\
&= \frac{(2\ell_a+1)(2\ell_b+1)(2c'+1)\sqrt{(2\ell_r+1)(2a'+1)(2b'+1)}}{(4\pi)^{3/2}} \begin{pmatrix} a' & \ell_a & c' \\ 0 & 0 & 0 \end{pmatrix} \begin{pmatrix} b' & \ell_b & c' \\ 0 & 0 & 0 \end{pmatrix} \begin{pmatrix} \ell_r & \ell_a & \ell_b \\ 0 & 0 & 0 \end{pmatrix} \\
&\times (-1)^{\ell_a+\ell_b+c'} \begin{Bmatrix} a' & b' & \ell_r \\ \ell_b & \ell_a & c' \end{Bmatrix} \begin{pmatrix} a' & b' & \ell_r \\ m_a & m_b & m_r \end{pmatrix}. \qquad \text{(C.12)}
\end{aligned}
$$

This gives us

$$
\begin{aligned}
\mathcal{A}_{a'b'c'} &= (4\pi)^3 \sum_{\ell_a \ell_b \ell_r} i^{\ell_a+\ell_b-\ell_r} j_{\ell_a}(qr) j_{\ell_b}(pr) j_{\ell_r}(kr) \\
&\quad \times \frac{(2\ell_a+1)(2\ell_b+1)(2c'+1)\sqrt{(2\ell_r+1)(2a'+1)(2b'+1)}}{(4\pi)^{3/2}} \\
&\quad \times \begin{pmatrix} a' & \ell_a & c' \\ 0 & 0 & 0 \end{pmatrix} \begin{pmatrix} b' & \ell_b & c' \\ 0 & 0 & 0 \end{pmatrix} \begin{pmatrix} \ell_r & \ell_a & \ell_b \\ 0 & 0 & 0 \end{pmatrix} (-1)^{\ell_a+\ell_b+c'} \begin{Bmatrix} a' & b' & \ell_r \\ \ell_b & \ell_a & c' \end{Bmatrix} \\
&\quad \times \sum_{m_a m_b m_r} Y^*_{a'm_a}(\hat{\boldsymbol{n}}) Y^*_{b'm_b}(\hat{\boldsymbol{n}}) Y^*_{\ell_r m_r}(\hat{\boldsymbol{k}}) \begin{pmatrix} a' & b' & \ell_r \\ m_a & m_b & m_r \end{pmatrix}. \qquad \text{(C.13)}
\end{aligned}
$$

Now we look at the product of spherical harmonics in $\mathcal{A}$, which we rewrite with Eq. (A.6), and the new 3j symbol from the Gaunt integral sum

$$
\begin{aligned}
&\sum_{m_a m_b m_r} Y^*_{a'm_a}(\hat{\boldsymbol{n}}) Y^*_{b'm_b}(\hat{\boldsymbol{n}}) Y^*_{\ell_r m_r}(\hat{\boldsymbol{k}}) \begin{pmatrix} a' & b' & \ell_r \\ m_a & m_b & m_r \end{pmatrix} \\
&= \sum_{m_a m_b m_r} (-1)^{m_a+m_b} Y_{a'-m_a}(\hat{\boldsymbol{n}}) Y_{b'-m_b}(\hat{\boldsymbol{n}}) Y^*_{\ell_r m_r}(\hat{\boldsymbol{k}}) \begin{pmatrix} a' & b' & \ell_r \\ m_a & m_b & m_r \end{pmatrix} \\
&= \sum_{m_a m_b m_r} \sum_{\ell_k m_k} \mathcal{G}^{-m_a-m_b-m_k}_{a'b'\ell_k} Y_{\ell_k m_k}(\hat{\boldsymbol{n}}) Y^*_{\ell_r m_r}(\hat{\boldsymbol{k}}) \begin{pmatrix} a' & b' & \ell_r \\ m_a & m_b & m_r \end{pmatrix} \\
&= \sum_{m_r \ell_k m_k} \sqrt{\frac{(2a'+1)(2b'+1)(2\ell_k+1)}{4\pi}} \begin{pmatrix} a' & b' & \ell_k \\ 0 & 0 & 0 \end{pmatrix} Y_{\ell_k m_k}(\hat{\boldsymbol{n}}) Y^*_{\ell_r m_r}(\hat{\boldsymbol{k}}) (-1)^{a'+b'+\ell_k}
\end{aligned}
$$

$$
\begin{aligned}
&\times \sum_{m_a m_b} \begin{pmatrix} a' & b' & \ell_k \\ m_a & m_b & m_k \end{pmatrix} \begin{pmatrix} a' & b' & \ell_r \\ m_a & m_b & m_r \end{pmatrix} \\
&= \sum_{m_r} \sqrt{\frac{(2a'+1)(2b'+1)(2\ell_k+1)}{4\pi}} \begin{pmatrix} a' & b' & \ell_k \\ 0 & 0 & 0 \end{pmatrix} Y_{\ell_k m_k}(\hat{\boldsymbol{n}}) Y^*_{\ell_r m_r}(\hat{\boldsymbol{k}}) (-1)^{a'+b'+\ell_k} \frac{\delta_{\ell_r \ell_k} \delta_{m_k m_r}}{2\ell_r+1} \\
&= (-1)^{a'+b'+\ell_r} \frac{\sqrt{(2a'+1)(2b'+1)(2\ell_r+1)}}{(4\pi)^{3/2}} \begin{pmatrix} a' & b' & \ell_r \\ 0 & 0 & 0 \end{pmatrix} \sum_{m_r} \frac{4\pi}{2\ell_r+1} Y_{\ell_r m_r}(\hat{\boldsymbol{n}}) Y^*_{\ell_r m_r}(\hat{\boldsymbol{k}}) \\
&= (-1)^{a'+b'+\ell_r} \frac{\sqrt{(2a'+1)(2b'+1)(2\ell_r+1)}}{(4\pi)^{3/2}} \begin{pmatrix} a' & b' & \ell_r \\ 0 & 0 & 0 \end{pmatrix} \mathcal{L}_{\ell_r}(\mu). \qquad \text{(C.14)}
\end{aligned}
$$

We now combine everything to get the final form of $\mathcal{A}$

$$
\begin{aligned}
\mathcal{A}_{a'b'c'} = &\sum_{\ell_a \ell_b \ell_r} i^{\ell_a+\ell_b-\ell_r} j_{\ell_a}(qr) j_{\ell_b}(pr) j_{\ell_r}(kr) (-1)^{\ell_a+\ell_b+c'+a'+b'+\ell_r} \\
&\times (2\ell_a+1)(2\ell_b+1)(2c'+1)(2\ell_r+1)(2a'+1)(2b'+1) \\
&\times \begin{pmatrix} a' & \ell_a & c' \\ 0 & 0 & 0 \end{pmatrix} \begin{pmatrix} b' & \ell_b & c' \\ 0 & 0 & 0 \end{pmatrix} \begin{pmatrix} \ell_r & \ell_a & \ell_b \\ 0 & 0 & 0 \end{pmatrix} \begin{pmatrix} a' & b' & \ell_r \\ 0 & 0 & 0 \end{pmatrix} \begin{Bmatrix} a' & b' & \ell_r \\ \ell_b & \ell_a & c' \end{Bmatrix} \mathcal{L}_{\ell_r}(\mu), \qquad \text{(C.15)}
\end{aligned}
$$

which allows us to write out the final expression for I

$$
\begin{aligned}
I_{a'b'c'} = &\sum_{\ell_a \ell_b \ell_r} i^{\ell_a+\ell_b-\ell_r} j_{\ell_a}(qr) j_{\ell_b}(pr) j_{\ell_r}(kr) (-1)^{\ell_a+\ell_b+c'+a'+b'+\ell_r} (2\ell_a+1)(2\ell_b+1)(2\ell_r+1) \\
&\times \begin{pmatrix} a' & \ell_a & c' \\ 0 & 0 & 0 \end{pmatrix} \begin{pmatrix} b' & \ell_b & c' \\ 0 & 0 & 0 \end{pmatrix} \begin{pmatrix} \ell_r & \ell_a & \ell_b \\ 0 & 0 & 0 \end{pmatrix} \begin{pmatrix} a' & b' & \ell_r \\ 0 & 0 & 0 \end{pmatrix} \begin{Bmatrix} a' & b' & \ell_r \\ \ell_b & \ell_a & c' \end{Bmatrix} \mathcal{L}_{\ell_r}(\mu), \qquad \text{(C.16)}
\end{aligned}
$$

which we can now plug back in to the original integral to arrive at

$$
\begin{aligned}
\mathcal{I}^{n_1 n_2}_{a'b'c'} = &(2\pi)^3 (-1)^{a'+b'+c'} \sum_{\ell_a \ell_b \ell_r} i^{\ell_a+\ell_b-\ell_r} (2\ell_a+1)(2\ell_b+1)(2\ell_r+1) \\
&\times \begin{pmatrix} a' & \ell_a & c' \\ 0 & 0 & 0 \end{pmatrix} \begin{pmatrix} b' & \ell_b & c' \\ 0 & 0 & 0 \end{pmatrix} \begin{pmatrix} \ell_r & \ell_a & \ell_b \\ 0 & 0 & 0 \end{pmatrix} \begin{pmatrix} a' & b' & \ell_r \\ 0 & 0 & 0 \end{pmatrix} \begin{Bmatrix} a' & b' & \ell_r \\ \ell_b & \ell_a & c' \end{Bmatrix} \mathcal{L}_{\ell_r}(\mu) \mathcal{R}^{\ell_a,\ell_b,\ell_r}_{n_1,n_2}, \qquad \text{(C.17)}
\end{aligned}
$$

where

$$
\mathcal{R}^{\ell_a,\ell_b,\ell_r}_{n_1,n_2} = \int \frac{dr}{2\pi^2} r^2 \xi^{\ell_a}_{n_1-2} \xi^{\ell_b}_{n_2-2} j_{\ell_r}(kr). \qquad \text{(C.18)}
$$

Here we have set $(-1)^{\ell_a+\ell_b+c'+a'+b'+\ell_r} = (-1)^{a'+b'+c'}$ because the conditions on a Wigner-3j symbol with all $m = 0$ require that the sum of l's is even. For the same reason the term $i^{\ell_a+\ell_b-\ell_r}$ is always real.

While this formulation is correct, we find that it needs an exceedingly large number of FFTs and is relatively unstable numerically. We instead decide to write the above equation in such a way as to minimize the number of total integrals

$$\mathcal{I}^{n_1 n_2}_{a'b'c} = (2\pi)^3(-1)^{a'+b'+c'} \sum_{\ell_r} \mathcal{L}_{\ell_r}(\mu)(2\ell_r+1) \begin{pmatrix} a' & b' & \ell_r \\ 0 & 0 & 0 \end{pmatrix} \mathfrak{R}^{n_1 n_2}_{a'b'c'\ell_r}, \tag{C.19}$$

where

$$\begin{aligned} \mathfrak{R}^{n_1 n_2}_{a'b'c'\ell_r} = \int \frac{dr}{2\pi^2} r^2 j_{\ell_r}(kr) \sum_{\ell_a \ell_b} i^{\ell_a+\ell_b-\ell_r}(2\ell_a+1)(2\ell_b+1) \\ \times \begin{pmatrix} a' & \ell_a & c' \\ 0 & 0 & 0 \end{pmatrix} \begin{pmatrix} b' & \ell_b & c' \\ 0 & 0 & 0 \end{pmatrix} \begin{pmatrix} \ell_r & \ell_a & \ell_b \\ 0 & 0 & 0 \end{pmatrix} \begin{Bmatrix} a' & b' & \ell_r \\ \ell_b & \ell_a & c' \end{Bmatrix} \xi^{\ell_a}_{n_1-2} \xi^{\ell_b}_{n_2-2}. \end{aligned} \tag{C.20}$$

This newer form requires many fewer FFTs, around half as many, so is greatly preferred. This is still not fully optimized however, as the multipole form requires even fewer FFTs, see Sec. 4.1 for the fully optimized form.

Appendix D
Polyspectrum Estimator in Discrete Fourier Transformation

In the main manuscript, we have presented the polyspectra estimator in an contiguous limit, as an integral form. In the practical implementation, we have converted the estimator into a discrete summation as we present here. For our discrete implementation, following the FFTW convention, we use the unnormalized Discrete Fourier Transform and explicitly pull out all normalization factors. For more details, authors refer to Chapter 7 of [126]. Here, we note the discrete version of variables by square bracket $[\boldsymbol{x}]$.

Let us first summarize the continuous version of the polyspectra estimator. Starting with the integral form of the general estimator Eq. (6.7)

$$\tilde{P}_n(k_1 \cdots, k_n) = \frac{V_f}{V_{\tilde{n}}(2\pi)^3} \int_{k_1} d^3q_1 \cdots \int_{k_n} d^3q_n \delta_D(\mathbf{q}_{1\cdots n}) \prod \delta(\mathbf{q}_i)\,. \tag{D.1}$$

We convert the Dirac-delta operator into its Fourier representation form:

$$\delta_D(x) = \int_{-\infty}^{\infty} \frac{d^3k}{(2\pi)^3} e^{ik\cdot x}\,, \tag{D.2}$$

which, when input back into the estimator, results in

$$\tilde{P}_n(k_1 \cdots, k_n) = \frac{V_f}{V_{\tilde{n}}(2\pi)^3} \int \frac{d^3x}{(2\pi)^3} \prod I_{k_i}(x), \tag{D.3}$$

where

$$I_{k_i}(x) = \int_{k_i} d^3q_i e^{i\boldsymbol{x}\cdot\boldsymbol{q}_i} \delta(\boldsymbol{q}_i) = \int d^3q_i e^{i\boldsymbol{x}\cdot\boldsymbol{q}_i} \tilde{I}_{k_i}(\boldsymbol{q}_i)\,, \tag{D.4}$$

is the Fourier Transform of $I_{k_i}(\boldsymbol{q})$ which is defined to be the same as $\delta(\boldsymbol{q})$ within a

spherical shell with Fourier-space radius $|\boldsymbol{q}| \simeq k_i$, and zero otherwise.

In the FFTW convention of un-normalized DFT, we find

$$I_{k_i}[\boldsymbol{x}] = \frac{(2\pi)^3}{N^3}\mathrm{FFTW}\left(\tilde{I}_{k_i}[\boldsymbol{q}]\right) , \tag{D.5}$$

with which we get a partially discretized estimator

$$\tilde{P}_n(k_1 \cdots, k_n) = \frac{V_f}{V_{\tilde{n}}(2\pi)^3}\left(\frac{(2\pi)^3}{N^3}\right)^n \int \frac{d^3x}{(2\pi)^3}\prod_{i=1}^{n}\mathrm{FFTW}\left(\tilde{I}_{k_i}[\boldsymbol{q}]\right) . \tag{D.6}$$

We then fully discretize the estimator by converting the final integral to a sum:

$$\begin{aligned}\tilde{P}_n(k_1 \cdots, k_n) &= \left(\frac{V_f^{n-1}}{V_{\tilde{n}}}\right)\frac{(2\pi)^{3n}}{V_f^{n-2}N^{3n}}\frac{V}{(2\pi)^6 N^3}\sum_{[\boldsymbol{x}]}\prod_{i=1}^{n}\mathrm{FFTW}\left(\tilde{I}_{k_i}[\boldsymbol{q}]\right) \\ &= \left(\frac{V_f^{n-1}}{V_{\tilde{n}}}\right)\frac{V^{n-1}}{N^{3n}}\frac{1}{N^3}\sum_{[\boldsymbol{x}]}\prod_{i=1}^{n}\mathrm{FFTW}\left(\tilde{I}_{k_i}[\boldsymbol{q}]\right) .\end{aligned} \tag{D.7}$$

Finally, the quantity in parenthesis $\frac{V_f^{n-1}}{V_{\tilde{n}}}$ is the reciprocal of the number of polygons, and we can compute them by applying the same polyspectra estimator to a Fourier grid of unity. Note, however, that the normalization is different here.

$$\frac{V_{\tilde{n}}}{V_f^{n-1}} = \frac{1}{V_f^{n-1}}\int_{k_1} d^3q_1 \cdots \int_{k_n} d^3q_n \delta_D(\mathbf{q}_{1\cdots n}) = \frac{1}{N^3 V_f^{n-1}}\sum_{[\boldsymbol{x}]}\prod_{i=1}^{n}\mathrm{FFTW}\left(\tilde{\iota}_{k_i}[\boldsymbol{q}]\right) . \tag{D.8}$$

where we define $\tilde{\iota}_{k_i}[\boldsymbol{q}]$, analogous to $\tilde{I}_{k_i}[\boldsymbol{q}]$ above, as the Fourier grid which takes unity within the spherical shell bounded by $|k - k_i| < \delta k/2$ and zero elsewhere.

Appendix E
Approximate Analytic Number of Polygons

In the polyspectra estimator, we have the normalization constant $\frac{V_{\tilde{n}}}{V_f^{n-1}}$, which is the number of n-gons that satisfy the closing condition (Dirac-delta) for a given set of side-length wavenumber k_i. In this appendix, we shall present the analytical approximation to this quantity.

Using the Dirac-delta (Eq. (D.2)), we rewrite the $3n$-dimensional volume $V_{\tilde{n}}$ as

$$V_{\tilde{n}} = \int_{k_1} d^3q_1 \cdots \int_{k_n} d^3q_n \delta_D(\mathbf{q}_{1\cdots n}) = \frac{1}{(2\pi)^3} \int dx^3 \int_{k_1} d^3q_1 e^{i\mathbf{x}\cdot\mathbf{q}_1} \cdots \int_{k_n} d^3q_n e^{i\mathbf{x}\cdot\mathbf{q}_n} \,, \quad \text{(E.1)}$$

for which we can compute the each q_i integration as

$$\int_k d^3q e^{i\mathbf{q}\cdot\mathbf{x}} = 4\pi \int_{k-\delta k/2}^{k+\delta k/2} dq q^2 \frac{\sin(qx)}{qx} \approx 4\pi \frac{k\sin(kx)}{x}\delta k + \mathcal{O}(\delta k^3). \quad \text{(E.2)}$$

Combining the two results, we reduce the number of n-gons to one-dimensional integration as

$$V_{\tilde{n}} = 2^{2n-3}\pi^{n-3}\left(\prod_{i=1}^n k_i \delta k\right) \int d^3x \frac{1}{x^n} \prod_{i=1}^n \sin(k_i x) = 2^{2n-1}\pi^{n-2}\left(\prod_{i=1}^n k_i \delta k\right) \int_0^\infty \frac{dx}{x^{n-2}} \prod_{i=1}^n \sin(k_i x) \,. \quad \text{(E.3)}$$

which is an analytically tractable integral, given the assumptions that $k_i \geq k_{i+1}$ (to uniquely define the polygon), and the polygon condition that $(\sum_{i\neq j} k_i) \geq k_j$.

In what follows, we shall show the calculations. First, we show the general strategy of integrating $\mathcal{I}_n$ in App. E.1, which is followed by the explicit result for $n = 3$ (App. E.2) and $n = 4$ (App. E.3) cases. We then present the calculation for the colinear case,

$k_1 = k_2 + \cdot + k_n$, where the approximation in Eq. (E.2) resulting zero for all $n > 4$ polygons. We therefore show the explicit expression without approximation in Eq. (E.2) in App. E.4.

E.1 The analytical calculation: general case

To simplify the notation, let us define following function

$$\mathcal{I}_n\left(k_1, \cdots, k_n\right) \equiv \int_0^\infty dx \frac{\prod \sin(k_i x)}{x^{n-2}} = \frac{1}{2}\int_{-\infty}^{\infty} \frac{dx}{x^{n-2}} \prod_{i=1}^{n} \sin\left(k_i x\right), \tag{E.4}$$

where we use that the integrand is an even function of x. Here, we show the general strategy of solving for the function $\mathcal{I}_n$. First, we use the following identity:

$$\frac{\sin(kx)}{kx} = \int_{-1}^{1} \frac{d\mu}{2}\, e^{ikx\mu}, \tag{E.5}$$

to transform the integration as

$$\mathcal{I}_n(k_1, \cdots, k_n) = k_1 \cdots k_{n-2} \int_{-\infty}^{\infty} \frac{dx}{2} \int_{-1}^{1} \frac{d\mu_1}{2} \cdots \int_{-1}^{1} \frac{d\mu_{n-2}}{2} e^{ix(k_1\mu_1 + \cdots + k_{n-2}\mu_{n-2})} \sin\left(k_{n-1}x\right) \sin\left(k_n x\right) . \tag{E.6}$$

We then use

$$\begin{aligned} \sin\left(k_{n-1}x\right) \sin\left(k_n x\right) =& \frac{1}{(2i)^2} \left[e^{ik_{n-1}x} - e^{-ik_{n-1}x}\right] \left[e^{ik_n x} - e^{-ik_n x}\right] \\ =& \frac{1}{4}\left(e^{i(k_{n-1}-k_n)x} + e^{-i(k_{n-1}-k_n)x} - e^{i(k_{n-1}+k_n)x} - e^{-i(k_{n-1}+k_n)x}\right), \end{aligned} \tag{E.7}$$

to convert the integrations in terms of the Dirac-delta operator:

$$\delta^D(k) = \int_{-\infty}^{\infty} \frac{dx}{2\pi} e^{ikx}. \tag{E.8}$$

That is,

$$\begin{aligned} \mathcal{I}_n(k_1, \cdots, k_n) =& \frac{\pi}{4} k_1 \cdots k_{n-2} \int_{-1}^{1} \frac{d\mu_1}{2} \cdots \int_{-1}^{1} \frac{d\mu_{n-2}}{2} \\ \times & \Bigg[\delta^D\left(k_1\mu_1 + \cdots + k_{n-2}\mu_{n-2} + k_{n-1} - k_n\right) + \delta^D\left(k_1\mu_1 + \cdots + k_{n-2}\mu_{n-2} - k_{n-1} + k_n\right) \end{aligned}$$

$$
\begin{aligned}
&\quad - \delta^D\left(k_1\mu_1 + \cdots + k_{n-2}\mu_{n-2} + k_{n-1} + k_n\right) - \delta^D\left(k_1\mu_1 + \cdots + k_{n-2}\mu_{n-2} - k_{n-1} - k_n\right)\Big] \\
=&\frac{\pi}{2} k_1 \cdots k_{n-2} \int_{-1}^{1} \frac{d\mu_1}{2} \cdots \int_{-1}^{1} \frac{d\mu_{n-2}}{2} \\
&\times \left[\delta^D\left(k_1\mu_1 + \cdots + k_{n-2}\mu_{n-2} + k_{n-1} - k_n\right) - \delta^D\left(k_1\mu_1 + \cdots + k_{n-2}\mu_{n-2} - k_{n-1} - k_n\right)\right] \\
=&\frac{\pi}{2} \int_{-k_1}^{k_1} \frac{d\kappa_1}{2} \cdots \int_{-k_{n-2}}^{k_{n-2}} \frac{d\kappa_{n-2}}{2} \\
&\times \left[\delta^D\left(\kappa_1 + \cdots + \kappa_{n-2} + k_{n-1} - k_n\right) - \delta^D\left(\kappa_1 + \cdots + \kappa_{n-2} - k_{n-1} - k_n\right)\right] . \qquad \text{(E.9)}
\end{aligned}
$$

Going beyond this result requires the conditions to form polygons. For general polygons in 3D there is only one condition, the longest side must be less than or equal to the sum of all the other sides. If we don't want to be bothered by the ordering, we can simply state as following: For any $j \in [1, n]$,

$$
k_j \leq k_1 + \cdots + k_{j-1} + k_{j+1} + \cdots + k_n = \sum_{i=1}^{n} k_i - k_j \,. \qquad \text{(E.10)}
$$

With this condition, we can see that there must be a solution for $\mu_i \in (0, 1)$ satisfying

$$
k_n = k_1\mu_1 + \cdots + k_{n-2}\mu_{n-2} + k_{n-1} \,. \qquad \text{(E.11)}
$$

For later use, we find following identity for the integration of the Dirac delta useful:

$$
\int_{-k}^{k} d\kappa \delta^D(\kappa - a) = \Theta(k - a, k + a). \qquad \text{(E.12)}
$$

Here $\Theta(x_1, x_2, \cdot, x_n)$ is a multi-dimensional Heaviside-Theta function, which is 1 only if none of the x_i are not positive.

E.2 The analytical calculation for triangles ($n = 3$)

For the bispectrum ($n = 3$), Eq. (E.9) reduces to

$$
\begin{aligned}
\mathcal{I}_3 =&\frac{\pi}{2} \int_{-k_1}^{k_1} \frac{d\kappa_1}{2} \left[\delta^D(\kappa_1 + k_2 - k_3) - \delta^D(\kappa_1 - k_2 - k_3)\right] \\
=&\frac{\pi}{4} \left[\Theta(k_1 + k_2 - k_3, k_1 - k_2 + k_3) - \Theta(k_1 - k_2 - k_3, k_1 + k_2 + k_3)\right] . \qquad \text{(E.13)}
\end{aligned}
$$

Without loss of generality, let us order the wavenumbers so that $k_1 \geq k_2 \geq k_3$. Then, from the polygon inequality in Eq. (E.10), the first term becomes

$$\Theta(k_1 + k_2 - k_3, k_1 - k_2 + k_3) = 1\,, \tag{E.14}$$

and the second term is

$$\Theta(k_1 - k_2 - k_3, k_1 + k_2 + k_3) = \begin{cases} 1/2 & ,\ k_1 = k_2 + k_3 \\ 0 & ,\ k_1 < k_2 + k_3 \end{cases}\,. \tag{E.15}$$

Therefore,

$$\mathcal{I}_3 = \begin{cases} \pi/8 & ,\ k_1 = k_2 + k_3 \\ \pi/4 & ,\ k_1 < k_2 + k_3 \end{cases}\,, \tag{E.16}$$

and

$$V_B = \begin{cases} 4\pi^2 k_1 k_2 k_3 \left(\delta k\right)^3 & ,\ k_1 = k_2 + k_3 \\ 8\pi^2 k_1 k_2 k_3 \left(\delta k\right)^3 & ,\ k_1 < k_2 + k_3 \end{cases}\,. \tag{E.17}$$

E.3 The analytical calculation for trispectrum

For the trispectrum ($n = 4$), Eq. (E.9) reduces to

$$\begin{aligned} \mathcal{I}_4 =& \frac{\pi}{2} \int_{-k_1}^{k_1} \frac{d\kappa_1}{2} \int_{-k_2}^{k_2} \frac{d\kappa_2}{2} \left[\delta^D(\kappa_1 + \kappa_2 + k_3 - k_4) - \delta^D(\kappa_1 + \kappa_2 - k_3 - k_4)\right] \\ =& \frac{\pi}{4} \int_{-k_1}^{k_1} \frac{d\kappa_1}{2} \\ & \times \left[\Theta(k_2 + \kappa_1 + k_3 - k_4, k_2 - \kappa_1 - k_3 + k_4) - \Theta(k_2 + \kappa_1 - k_3 - k_4, k_2 - \kappa_1 + k_3 + k_4)\right]\,. \end{aligned} \tag{E.18}$$

Again, without loss of generality, we can order the wavenumbers so that $k_1 \geq k_2 \geq k_3 \geq k_4$.

We first consider the case where $k_1 = k_2 + k_3 + k_4$. The integration then becomes

$$\begin{aligned} \mathcal{I}_4 =& \frac{\pi}{4} \int_{-k_1}^{k_1} \frac{d\kappa_1}{2} \left[\Theta(\kappa_1 + k_1 - 2k_4, -\kappa_1 + k_1 - 2k_3) - \Theta(\kappa_1 + 2k_2 - k_1, k_1 - \kappa_1)\right] \\ =& \frac{\pi}{4} \left[\int_{\max(-k_1, -k_1 + 2k_4)}^{\min(k_1, k_1 - 2k_3)} \frac{d\kappa_1}{2} - \int_{\max(-k_1, k_1 - 2k_2)}^{k_1} \frac{d\kappa_1}{2}\right] \\ =& \frac{\pi}{8} \left[k_1 - 2k_3 - (-k_1 + 2k_4) - (k_1 - (k_1 - 2k_2))\right] = 0\,. \end{aligned} \tag{E.19}$$

That is, the number of trispectrum using Eq. (E.2) vanishes for the colinear quadraliterals.

We present the expression without using the approximation in App. E.4.

For the other cases, $k_1 < k_2 + k_3 + k_4$, we integrate $\mathcal{I}_4$ as following. The first Heaviside-Theta function vanishes unless,

$$-k_2 - k_3 + k_4 \leq \kappa_1 \leq k_2 - k_3 + k_4, \tag{E.20}$$

so that we integrate the first term as

$$\begin{aligned}&\int_{-k_1}^{k_1} \frac{d\kappa_1}{2} \Theta(k_2 + \kappa_1 + k_3 - k_4, k_2 - \kappa_1 - k_3 + k_4) = \int_{\max(-k_1, -k_2 - k_3 + k_4)}^{\min(k_1, k_2 - k_3 + k_4)} \frac{d\kappa_1}{2} \\ =&\frac{1}{2} \left[\min(k_1, k_2 - k_3 + k_4) - \max(-k_1, -k_2 - k_3 + k_4)\right] . \end{aligned} \tag{E.21}$$

From Eq. (E.10), we know that $k_1 > -k_2 - k_3 + k_4$, and $-k_1 < k_2 - k_3 + k_4$, and, of course, $k_2 - k_3 + k_4 > -k_2 - k_3 + k_4$. Therefore,

$$\begin{aligned}&\frac{1}{2} \left[\min(k_1, k_2 - k_3 + k_4) - \max(-k_1, -k_2 - k_3 + k_4)\right] \\ =&\frac{1}{2} \left[2k_2 + (k_1 - k_2 + k_3 - k_4)\, \Theta\left(k_2 - k_3 + k_4 - k_1\right) + (k_1 - k_2 - k_3 + k_4)\, \Theta\left(-k_1 + k_2 + k_3 - k_4\right)\right] . \end{aligned} \tag{E.22}$$

The second Heaviside-Theta function vanishes unless,

$$-k_2 + k_3 + k_4 \leq \kappa_1 \leq k_2 + k_3 + k_4. \tag{E.23}$$

Using that, we find, from Eq. (E.10), $k_1 < k_2 + k_2 + k_4$ and $-k_1 < -k_2 + k_3 + k_4$, and of course, $-k_2 + k_3 + k_4 < k_2 + k_3 + k_4$. Therefore,

$$\begin{aligned}&\int_{-k_1}^{k_1} \frac{d\kappa_1}{2} \Theta(k_2 + \kappa_1 - k_3 - k_4, k_2 - \kappa_1 + k_3 + k_4) = \int_{\max(-k_1, -k_2 + k_3 + k_4)}^{\min(k_1, k_2 + k_3 + k_4)} \frac{d\kappa_1}{2} = \int_{-k_2 + k_3 + k_4}^{k_1} \frac{d\kappa_1}{2} \\ =&\left(\frac{k_1 + k_2 - k_3 - k_4}{2}\right) \Theta(k_1 + k_2 - k_3 - k_4) . \end{aligned} \tag{E.24}$$

Combining all, we find that

$$\begin{aligned} I_4 =&\frac{\pi}{8} \left[2k_2 + (k_1 - k_2 + k_3 - k_4)\, \Theta\left(k_2 - k_3 + k_4 - k_1\right)\right. \\ &\left. + (k_1 - k_2 - k_3 + k_4)\, \Theta\left(-k_1 + k_2 + k_3 - k_4\right) + (k_1 + k_2 - k_3 - k_4)\, \Theta(k_1 + k_2 - k_3 - k_4)\right] . \end{aligned} \tag{E.25}$$

We then calculate the V_T as

$$V_T = 8\pi^3 k_1 k_2 k_3 k_4 \delta k^4 (-k_1 + k_2 + k_3 + 3k_4 - |k_1 - k_2 - k_3 + k_4|)\,. \tag{E.26}$$

E.4 Exact analytic colinear case

For the higher-order polyspectra, the lowest order theory predicts zero polygons for the colinear case $k_1 = \sum_2^n k_i$ but this is clearly not the case through either direct summation tests or estimation through our method. Simply adding a few higher-order terms in the series of Eq. (E.2) causes the integration to diverge so we instead need to solve the exact case directly.

The full calculation for the integration that we approximate in Eq. (E.2) yields

$$\int_{k-\delta k/2}^{k+\delta k/2} dq q^2 \frac{\sin(qx)}{qx} = \frac{-x\delta k \cos(kx)\cos(x\delta k/2) + 2\left[\cos(kx) + kx\sin(kx)\right]\sin(x\delta k/2)}{x^3}\,. \tag{E.27}$$

Restricting to the colinear case, we calculate the Fourier volume integration for the bispectrum:

$$V_B = \frac{32\pi^2}{6144}\delta k^3 \left[104k_3^2\delta k + 5\delta k^3 + 8k_2^2(96k_3 + 13\delta k) + 8k_2k_3(96k_3 + 13\delta k)\right]\,, \tag{E.28}$$

and for the trispectrum

$$V_{\tilde{T}} = \begin{cases} \frac{128\pi^3\delta k^5}{725760}\left[\delta k\left\{468k_4^2\delta k + 17\delta k^3 + 36k_3^2(105k_4 + 13\delta k)\right.\right. & \\ \quad +36k_3k_4(105k_4 + 13\delta k)\} & \\ \quad +36k_2^2\left\{21k_3(28k_4 + 5\delta k) + \delta k(105k_4 + 13\delta k)\right\} & k_4 > \delta k \\ \quad +36k_2\left\{21k_3^2(28k_4 + 5\delta k) + k_4\delta k(105k_4 + 13\delta k)\right. & \\ \quad \left.\left. +k_3(588k_4^2 + 210k_4\delta k + 13\delta k^2)\right\}\right] & \\ \frac{128\pi^3\delta k^6}{725760}\left[24948k_2^2k_3 + 24948k_2k_3^2 + 36(118k_2^2 + 811k_2k_3 + 118k_3^2)\delta k\right. & \\ \quad \left. +4248(k_2 + k_3)\delta k^2 + 485\delta k^3\right] & k_4 = \delta k \\ \frac{128\pi^3\delta k^7}{725760}(29196k_2^2 + 58392k_2\delta k + 8981\delta k^2) & k_3 = \delta k \\ \frac{12364288\pi^3\delta k^9}{725760} & k_2 = \delta k \end{cases}\,, \tag{E.29}$$

by using the Mathematica package.

For the Bispectrum case Eq. (E.28) differs only about 1% from the lowest order estimation. For trispectrum, where the lowest order approximation predicts zero polygons,

Eq. (E.29) dramatically improves the match between the numerical calculation and analytical estimation, as we show in Fig. 6.3.

Bibliography

[1] D.J. Eisenstein and W. Hu, *Baryonic features in the matter transfer function*, *The Astrophysical Journal* **496** (1998) 605–614.

[2] T. Nishimichi, A. Shirata, A. Taruya, K. Yahata, S. Saito, Y. Suto et al., *Modeling nonlinear evolution of baryon acoustic oscillations: Convergence regime of n-body simulations and analytic models*, *Publications of the Astronomical Society of Japan* **61** (2009) 321–332.

[3] V. Desjacques, D. Jeong and F. Schmidt, *Large-scale galaxy bias*, *PhR* **733** (2018) 1 [1611.09787].

[4] V. Desjacques, D. Jeong and F. Schmidt, *The Galaxy Power Spectrum and Bispectrum in Redshift Space*, *JCAP* **1812** (2018) 035 [1806.04015].

[5] E.V. Linder, *Cosmic growth history and expansion history*, *Phys. Rev. D* **72** (2005) 043529 [astro-ph/0507263].

[6] Planck Collaboration, N. Aghanim, Y. Akrami, M. Ashdown, J. Aumont, C. Baccigalupi et al., *Planck 2018 results. VI. Cosmological parameters*, *arXiv e-prints* (2018) [1807.06209].

[7] O. Doré, J. Bock, M. Ashby, P. Capak, A. Cooray, R. de Putter et al., *Cosmology with the spherex all-sky spectral survey*, 2015.

[8] G.J. Hill, K. Gebhardt, E. Komatsu, N. Drory, P.J. MacQueen, J. Adams et al., *The hobby-eberly telescope dark energy experiment (hetdex): Description and early pilot survey results*, 2008.

[9] R. Laureijs, J. Amiaux, S. Arduini, J.L. Augueres, J. Brinchmann, R. Cole et al., *Euclid Definition Study Report*, *arXiv e-prints* (2011) arXiv:1110.3193 [1110.3193].

[10] M. Levi, C. Bebek, T. Beers, R. Blum, R. Cahn, D. Eisenstein et al., *The desi experiment, a whitepaper for snowmass 2013*, 2013.

[11] L.D.E.S. Collaboration, *Large synoptic survey telescope: Dark energy science collaboration*, 2012.

[12] R. Maartens, F.B. Abdalla, M. Jarvis and M.G. Santos, *Cosmology with the ska – overview*, 2015.

[13] D. Spergel, N. Gehrels, C. Baltay, D. Bennett, J. Breckinridge, M. Donahue et al., *Wide-field infrarred survey telescope-astrophysics focused telescope assets wfirst-afta 2015 report*, 2015.

[14] M. Takada, R.S. Ellis, M. Chiba, J.E. Greene, H. Aihara, N. Arimoto et al., *Extragalactic science, cosmology, and galactic archaeology with the subaru prime focus spectrograph*, *Publications of the Astronomical Society of Japan* **66** (2014) R1.

[15] M. Schmittfull, Z. Vlah and P. McDonald, *Fast large scale structure perturbation theory using one-dimensional fast fourier transforms*, *Physical Review D* **93** (2016) .

[16] J.E. McEwen, X. Fang, C.M. Hirata and J.A. Blazek, *Fast-pt: a novel algorithm to calculate convolution integrals in cosmological perturbation theory*, *Journal of Cosmology and Astroparticle Physics* **2016** (2016) 015–015.

[17] Z. Slepian, *On decoupling the integrals of cosmological perturbation theory*, 2018.

[18] M. Schmittfull and Z. Vlah, *Reducing the two-loop large-scale structure power spectrum to low-dimensional, radial integrals*, *Physical Review D* **94** (2016) .

[19] M. Simonović, T. Baldauf, M. Zaldarriaga, J.J. Carrasco and J.A. Kollmeier, *Cosmological perturbation theory using the fftlog: formalism and connection to qft loop integrals*, *Journal of Cosmology and Astroparticle Physics* **2018** (2018) 030–030.

[20] R. Scoccimarro, *Redshift-space distortions, pairwise velocities, and nonlinearities*, *Physical Review D* **70** (2004) .

[21] A. Taruya, T. Nishimichi and S. Saito, *Baryon acoustic oscillations in 2d: Modeling redshift-space power spectrum from perturbation theory*, *Physical Review D* **82** (2010) .

[22] Z. Zheng, R. Cen, H. Trac and J. Miralda-Escudé, *Radiative transfer modeling of lyα emitters. ii. new effects on galaxy clustering*, *The Astrophysical Journal* **726** (2010) 38.

[23] C.M. Hirata, *Tidal alignments as a contaminant of redshift space distortions*, *Monthly Notices of the Royal Astronomical Society* **399** (2009) 1074–1087.

[24] J. Blazek, Z. Vlah and U. Seljak, *Tidal alignment of galaxies*, *Journal of Cosmology and Astroparticle Physics* **2015** (2015) 015–015.

[25] A. Eggemeier, R. Scoccimarro and R.E. Smith, *Bias loop corrections to the galaxy bispectrum*, *Physical Review D* **99** (2019) .

[26] J.E. Bautista et al., *The SDSS-IV extended Baryon Oscillation Spectroscopic Survey: Baryon Acoustic Oscillations at redshift of 0.72 with the DR14 Luminous Red Galaxy Sample*, *Astrophys. J.* **863** (2018) 110 [1712.08064].

[27] V. de Sainte Agathe et al., *Baryon acoustic oscillations at $z = 2.34$ from the correlations of Lyα absorption in eBOSS DR14*, *Astron. Astrophys.* **629** (2019) A85 [1904.03400].

[28] H. Gil-Marín et al., *The clustering of galaxies in the SDSS-III Baryon Oscillation Spectroscopic Survey: RSD measurement from the LOS-dependent power spectrum of DR12 BOSS galaxies*, *Mon. Not. Roy. Astron. Soc.* **460** (2016) 4188 [1509.06386].

[29] BOSS collaboration, *The clustering of galaxies in the completed SDSS-III Baryon Oscillation Spectroscopic Survey: Anisotropic galaxy clustering in Fourier-space*, *Mon. Not. Roy. Astron. Soc.* **466** (2017) 2242 [1607.03150].

[30] M.M. Ivanov, M. Simonović and M. Zaldarriaga, *Cosmological Parameters from the BOSS Galaxy Power Spectrum*, 1909.05277.

[31] G.-B. Zhao et al., *The clustering of the SDSS-IV extended Baryon Oscillation Spectroscopic Survey DR14 quasar sample: a tomographic measurement of cosmic structure growth and expansion rate based on optimal redshift weights*, *Mon. Not. Roy. Astron. Soc.* **482** (2019) 3497 [1801.03043].

[32] T. Colas, G. D'amico, L. Senatore, P. Zhang and F. Beutler, *Efficient Cosmological Analysis of the SDSS/BOSS data from the Effective Field Theory of Large-Scale Structure*, 1909.07951.

[33] G.-B. Zhao et al., *The extended Baryon Oscillation Spectroscopic Survey: a cosmological forecast*, *Mon. Not. Roy. Astron. Soc.* **457** (2016) 2377 [1510.08216].

[34] G. D'Amico, L. Senatore and P. Zhang, *Limits on wCDM from the EFTofLSS with the PyBird code*, 2003.07956.

[35] BOSS collaboration, *The clustering of galaxies in the completed SDSS-III Baryon Oscillation Spectroscopic Survey: towards a computationally efficient analysis without informative priors*, *Mon. Not. Roy. Astron. Soc.* **468** (2017) 4116 [1607.03152].

[36] F. Bernardeau, S. Colombi, E. Gaztañaga and R. Scoccimarro, *Large-scale structure of the Universe and cosmological perturbation theory*, *PhR* **367** (2002) 1 [astro-ph/0112551].

[37] D. Jeong and E. Komatsu, *Perturbation Theory Reloaded: Analytical Calculation of Nonlinearity in Baryonic Oscillations in the Real-Space Matter Power Spectrum*, *ApJ* **651** (2006) 619 [astro-ph/0604075].

[38] D. Jeong and E. Komatsu, *Perturbation Theory Reloaded. II. Nonlinear Bias, Baryon Acoustic Oscillations, and Millennium Simulation in Real Space*, *ApJ* **691** (2009) 569 [0805.2632].

[39] G. D'Amico, J. Gleyzes, N. Kokron, D. Markovic, L. Senatore, P. Zhang et al., *The Cosmological Analysis of the SDSS/BOSS data from the Effective Field Theory of Large-Scale Structure*, 1909.05271.

[40] D. Jeong and E. Komatsu, *Perturbation theory reloaded: Analytical calculation of nonlinearity in baryonic oscillations in the real-space matter power spectrum*, *The Astrophysical Journal* **651** (2006) 619–626.

[41] A. Taruya, T. Nishimichi, S. Saito and T. Hiramatsu, *Nonlinear evolution of baryon acoustic oscillations from improved perturbation theory in real and redshift spaces*, *Physical Review D* **80** (2009) .

[42] K. Osato, T. Nishimichi, F. Bernardeau and A. Taruya, *Perturbation theory challenge for cosmological parameters estimation: Matter power spectrum in real space*, *Physical Review D* **99** (2019) .

[43] A. Lazanu, T. Giannantonio, M. Schmittfull and E. Shellard, *Matter bispectrum of large-scale structure: Three-dimensional comparison between theoretical models and numerical simulations*, *Physical Review D* **93** (2016) .

[44] T. Steele and T. Baldauf, *Precise calibration of the one-loop bispectrum in the effective field theory of large scale structure*, *Physical Review D* **103** (2021) .

[45] A. Lazanu and M. Liguori, *The two and three-loop matter bispectrum in perturbation theories*, *Journal of Cosmology and Astroparticle Physics* **2018** (2018) 055.

[46] T. Baldauf, M. Garny, P. Taule and T. Steele, *Two-loop bispectrum of large-scale structure*, *Physical Review D* **104** (2021) .

[47] F. Villaescusa-Navarro, C. Hahn, E. Massara, A. Banerjee, A.M. Delgado, D.K. Ramanah et al., *The quijote simulations*, *The Astrophysical Journal Supplement Series* **250** (2020) 2.

[48] N. Kaiser, *On the spatial correlations of Abell clusters.*, *Astrophys. J. Lett* **284** (1984) L9.

[49] J.M. Bardeen, J.R. Bond, N. Kaiser and A.S. Szalay, *The Statistics of Peaks of Gaussian Random Fields*, *ApJ* **304** (1986) 15.

[50] J.N. Fry and E. Gaztanaga, *Biasing and hierarchical statistics in large scale structure*, *Astrophys. J.* **413** (1993) 447 [astro-ph/9302009].

[51] N. Kaiser, *Clustering in real space and in redshift space*, *MNRAS* **227** (1987) 1.

[52] A.F. Heavens, S. Matarrese and L. Verde, *The non-linear redshift-space power spectrum of galaxies*, *MNRAS* **301** (1998) 797 [astro-ph/9808016].

[53] R. Scoccimarro, *Redshift-space distortions, pairwise velocities, and nonlinearities*, *Phys. Rev. D* **70** (2004) 083007 [astro-ph/0407214].

[54] A. Taruya, T. Nishimichi and S. Saito, *Baryon acoustic oscillations in 2D: Modeling redshift-space power spectrum from perturbation theory*, *Phys. Rev. D* **82** (2010) 063522 [1006.0699].

[55] Z. Zheng, R. Cen, H. Trac and J. Miralda-Escudé, *Radiative Transfer Modeling of Lyα Emitters. II. New Effects on Galaxy Clustering*, *ApJ* **726** (2011) 38 [1003.4990].

[56] C.M. Hirata, *Tidal alignments as a contaminant of redshift space distortions*, *MNRAS* **399** (2009) 1074 [0903.4929].

[57] P. Catelan, M. Kamionkowski and R.D. Blandford, *Intrinsic and extrinsic galaxy alignment*, *Mon. Not. Roy. Astron. Soc.* **320** (2001) L7 [astro-ph/0005470].

[58] C.M. Hirata and U. Seljak, *Intrinsic alignment-lensing interference as a contaminant of cosmic shear*, *Phys. Rev.* **D70** (2004) 063526 [astro-ph/0406275].

[59] M.L. Brown, A.N. Taylor, N.C. Hambly and S. Dye, *Measurement of intrinsic alignments in galaxy ellipticities*, *Mon. Not. Roy. Astron. Soc.* **333** (2002) 501 [astro-ph/0009499].

[60] J. Blazek, M. McQuinn and U. Seljak, *Testing the tidal alignment model of galaxy intrinsic alignment*, *JCAP* **2011** (2011) 010 [1101.4017].

[61] B. Joachimi, R. Mandelbaum, F.B. Abdalla and S.L. Bridle, *Constraints on intrinsic alignment contamination of weak lensing surveys using the MegaZ-LRG sample*, *Astron. Astrophys.* **527** (2011) A26 [1008.3491].

[62] D. Martens, C.M. Hirata, A.J. Ross and X. Fang, *A Radial Measurement of the Galaxy Tidal Alignment Magnitude with BOSS Data*, *Mon. Not. Roy. Astron. Soc.* **478** (2018) 711 [1802.07708].

[63] J. Blazek, Z. Vlah and U. Seljak, *Tidal alignment of galaxies*, *JCAP* **1508** (2015) 015 [1504.02510].

[64] M. Schmittfull, Z. Vlah and P. McDonald, *Fast large scale structure perturbation theory using one-dimensional fast Fourier transforms*, *Phys. Rev.* **D93** (2016) 103528 [1603.04405].

[65] J.E. McEwen, X. Fang, C.M. Hirata and J.A. Blazek, *FAST-PT: a novel algorithm to calculate convolution integrals in cosmological perturbation theory*, *JCAP* **1609** (2016) 015 [1603.04826].

[66] A.E. Siegman, *Quasi fast hankel transform*, *Opt. Lett.* **1** (1977) 13.

[67] J.D. Talman, *Numerical fourier and bessel transforms in logarithmic variables*, *Journal of Computational Physics* **29** (1978) 35 .

[68] A.J.S. Hamilton, *Uncorrelated modes of the nonlinear power spectrum*, *Mon. Not. Roy. Astron. Soc.* **312** (2000) 257 [astro-ph/9905191].

[69] H.S. Grasshorn Gebhardt and D. Jeong, *Fast and accurate computation of projected two-point functions*, *Phys. Rev.* **D97** (2018) 023504 [1709.02401].

[70] M. Schmittfull and Z. Vlah, *FFT-PT: Reducing the two-loop large-scale structure power spectrum to low-dimensional radial integrals*, *Phys. Rev.* **D94** (2016) 103530 [1609.00349].

[71] Z. Slepian, *On Decoupling the Integrals of Cosmological Perturbation Theory*, 1812.02728.

[72] X. Fang, J.A. Blazek, J.E. McEwen and C.M. Hirata, *FAST-PT II: an algorithm to calculate convolution integrals of general tensor quantities in cosmological perturbation theory*, *JCAP* **1702** (2017) 030 [1609.05978].

[73] M. Simonović, T. Baldauf, M. Zaldarriaga, J.J. Carrasco and J.A. Kollmeier, *Cosmological perturbation theory using the FFTLog: formalism and connection to QFT loop integrals*, *JCAP* **1804** (2018) 030 [1708.08130].

[74] R.E. Smith, R.K. Sheth and R. Scoccimarro, *Analytic model for the bispectrum of galaxies in redshift space*, *Physical Review D* **78** (2008) .

[75] C. Rampf and Y.Y. Wong, *Lagrangian perturbations and the matter bispectrum ii: the resummed one-loop correction to the matter bispectrum*, *Journal of Cosmology and Astroparticle Physics* **2012** (2012) 018–018.

[76] V. Assassi, D. Baumann, D. Green and M. Zaldarriaga, *Renormalized halo bias*, *Journal of Cosmology and Astroparticle Physics* **2014** (2014) 056–056.

[77] F. Bernardeau, M. Crocce and R. Scoccimarro, *Constructing regularized cosmic propagators*, *Physical Review D* **85** (2012) .

[78] R.E. Angulo, S. Foreman, M. Schmittfull and L. Senatore, *The one-loop matter bispectrum in the effective field theory of large scale structures*, *Journal of Cosmology and Astroparticle Physics* **2015** (2015) 039–039.

[79] A. Eggemeier, R. Scoccimarro, R.E. Smith, M. Crocce, A. Pezzotta and A.G. Sánchez, *Testing one-loop galaxy bias: joint analysis of power spectrum and bispectrum*, 2021.

[80] N. McCullagh, D. Jeong and A.S. Szalay, *Toward accurate modelling of the non-linear matter bispectrum: standard perturbation theory and transients from initial conditions*, *Monthly Notices of the Royal Astronomical Society* **455** (2015) 2945–2958.

[81] E. Sefusatti, M. Crocce, S. Pueblas and R. Scoccimarro, *Cosmology and the bispectrum*, *Physical Review D* **74** (2006) .

[82] Y.-S. Song, A. Taruya and A. Oka, *Cosmology with anisotropic galaxy clustering from the combination of power spectrum and bispectrum*, *Journal of Cosmology and Astroparticle Physics* **2015** (2015) 007–007.

[83] J. Byun, A. Eggemeier, D. Regan, D. Seery and R.E. Smith, *Towards optimal cosmological parameter recovery from compressed bispectrum statistics*, *Monthly Notices of the Royal Astronomical Society* **471** (2017) 1581–1618.

[84] E. Sefusatti, M. Crocce and V. Desjacques, *The halo bispectrum in n-body simulations with non-gaussian initial conditions*, *Monthly Notices of the Royal Astronomical Society* **425** (2012) 2903–2930.

[85] M. Tellarini, A.J. Ross, G. Tasinato and D. Wands, *Galaxy bispectrum, primordial non-gaussianity and redshift space distortions*, *Journal of Cosmology and Astroparticle Physics* **2016** (2016) 014–014.

[86] D. Karagiannis, J. Fonseca, R. Maartens and S. Camera, *Probing primordial non-gaussianity with the bispectrum of future 21cm intensity maps*, 2020.

[87] A.M. Dizgah, M. Biagetti, E. Sefusatti, V. Desjacques and J. Noreña, *Primordial non-gaussianity from biased tracers: Likelihood analysis of real-space power spectrum and bispectrum*, 2020.

[88] A. Chudaykin and M.M. Ivanov, *Measuring neutrino masses with large-scale structure: Euclid forecast with controlled theoretical error*, *Journal of Cosmology and Astroparticle Physics* **2019** (2019) 034–034.

[89] C. Hahn, F. Villaescusa-Navarro, E. Castorina and R. Scoccimarro, *Constraining $m\nu$ with the bispectrum. part i. breaking parameter degeneracies*, *Journal of Cosmology and Astroparticle Physics* **2020** (2020) 040–040.

[90] C. Hahn and F. Villaescusa-Navarro, *Constraining m_ν with the bispectrum ii: The total information content of the galaxy bispectrum*, 2020.

[91] F. Kamalinejad and Z. Slepian, *A non-degenerate neutrino mass signature in the galaxy bispectrum*, 2020.

[92] R. Scoccimarro, *The Bispectrum: From Theory to Observations*, *ApJ* **544** (2000) 597 [astro-ph/0004086].

[93] F. Bernardeau, S. Colombi, E. Gaztañaga and R. Scoccimarro, *Large-scale structure of the universe and cosmological perturbation theory*, *Physics Reports* **367** (2002) 1–248.

[94] C.L. Bennett, D. Larson, J.L. Weiland, N. Jarosik, G. Hinshaw, N. Odegard et al., *Nine-year Wilkinson Microwave Anisotropy Probe (WMAP) Observations: Final Maps and Results*, *ApJS* **208** (2013) 20 [1212.5225].

[95] Planck Collaboration, Y. Akrami, F. Arroja, M. Ashdown, J. Aumont, C. Baccigalupi et al., *Planck 2018 results. IX. Constraints on primordial non-Gaussianity*, *A&A* **641** (2020) A9 [1905.05697].

[96] A. Lewis, A. Challinor and A. Lasenby, *Efficient computation of cosmic microwave background anisotropies in closed friedmann-robertson-walker models*, *The Astrophysical Journal* **538** (2000) 473–476.

[97] Planck Collaboration, N. Aghanim, Y. Akrami, M. Ashdown, J. Aumont, C. Baccigalupi et al., *Planck 2018 results. VI. Cosmological parameters*, *A&A* **641** (2020) A6 [1807.06209].

[98] N. Hand, Y. Feng, F. Beutler, Y. Li, C. Modi, U. Seljak et al., *nbodykit: An open-source, massively parallel toolkit for large-scale structure*, *The Astronomical Journal* **156** (2018) 160.

[99] E. Sefusatti, M. Crocce, R. Scoccimarro and H.M.P. Couchman, *Accurate estimators of correlation functions in fourier space*, *Monthly Notices of the Royal Astronomical Society* **460** (2016) 3624–3636.

[100] R. Scoccimarro, *Fast estimators for redshift-space clustering*, *Physical Review D* **92** (2015) .

[101] J. Tomlinson, D. Jeong and J. Kim, *Efficient parallel algorithm for estimating higher-order polyspectra*, *The Astronomical Journal* **158** (2019) 116.

[102] A. Taruya, T. Nishimichi and D. Jeong, *Grid-based calculation for perturbation theory of large-scale structure*, *Physical Review D* **98** (2018) .

[103] A. Slosar, C. Hirata, U. Seljak, S. Ho and N. Padmanabhan, *Constraints on local primordial non-gaussianity from large scale structure*, *Journal of Cosmology and Astroparticle Physics* **2008** (2008) 031.

[104] N. Hamaus, U. Seljak and V. Desjacques, *Optimal constraints on local primordial non-Gaussianity from the two-point statistics of large-scale structure*, *Phys. Rev. D* **84** (2011) 083509 [1104.2321].

[105] T. Giannantonio, A.J. Ross, W.J. Percival, R. Crittenden, D. Bacher, M. Kilbinger et al., *Improved primordial non-gaussianity constraints from measurements of galaxy clustering and the integrated sachs-wolfe effect*, *Phys. Rev. D* **89** (2014) 023511.

[106] N. Agarwal, S. Ho and S. Shandera, *Constraining the initial conditions of the universe using large scale structure*, *Journal of Cosmology and Astroparticle Physics* **2014** (2014) 038.

[107] A. Barreira, G. Cabass, F. Schmidt, A. Pillepich and D. Nelson, *Galaxy bias and primordial non-Gaussianity: insights from galaxy formation simulations with IllustrisTNG*, *J. Cosmology Astropart. Phys.* **2020** (2020) 013 [2006.09368].

[108] A. Moradinezhad Dizgah, M. Biagetti, E. Sefusatti, V. Desjacques and J. Noreña, *Primordial non-Gaussianity from biased tracers: likelihood analysis of real-space power spectrum and bispectrum*, *J. Cosmology Astropart. Phys.* **2021** (2021) 015 [2010.14523].

[109] M. Rezaie, A.J. Ross, H.-J. Seo, E.-M. Mueller, W.J. Percival, G. Merz et al., *Primordial non-gaussianity from the completed SDSS-IV extended baryon oscillation spectroscopic survey – i: Catalogue preparation and systematic mitigation*, *Monthly Notices of the Royal Astronomical Society* **506** (2021) 3439.

[110] E. Sefusatti, M. Crocce and V. Desjacques, *The matter bispectrum in n-body simulations with non-gaussian initial conditions*, *Monthly Notices of the Royal Astronomical Society* (2010) no–no.

[111] V. Yankelevich and C. Porciani, *Cosmological information in the redshift-space bispectrum*, *Monthly Notices of the Royal Astronomical Society* **483** (2018) 2078–2099.

[112] A. Oddo, E. Sefusatti, C. Porciani, P. Monaco and A.G. Sánchez, *Toward a robust inference method for the galaxy bispectrum: likelihood function and model selection*, *Journal of Cosmology and Astroparticle Physics* **2020** (2020) 056–056.

[113] D. Jeong and E. Komatsu, *Primordial Non-Gaussianity, Scale-dependent Bias, and the Bispectrum of Galaxies*, *ApJ* **703** (2009) 1230 [0904.0497].

[114] V. Desjacques, D. Jeong and F. Schmidt, *Large-scale galaxy bias*, *Physics Reports* **733** (2018) 1–193.

[115] D.N. Spergel, R. Bean, O. Doré, M.R. Nolta, C.L. Bennett, J. Dunkley et al., *Three-Year Wilkinson Microwave Anisotropy Probe (WMAP) Observations: Implications for Cosmology*, *ApJS* **170** (2007) 377 [astro-ph/0603449].

[116] D.A. Varshalovich, A.N. Moskalev and V.K. Khersonskii, *Quantum Theory of Angular Momentum* (1988), 10.1142/0270.

[117] J. Tomlinson, H.S.G. Gebhardt and D. Jeong, *Fast calculation of the nonlinear redshift-space galaxy power spectrum including selection bias*, *Physical Review D* **101** (2020) .

[118] P. McDonald, *Clustering of dark matter tracers: Renormalizing the bias parameters*, *Phys. Rev. D* **74** (2006) 103512 [astro-ph/0609413].

[119] H.S. Grasshorn Gebhardt, D. Jeong, H. Awan, J.S. Bridge, R. Ciardullo, D. Farrow et al., *Unbiased Cosmological Parameter Estimation from Emission-line Surveys with Interlopers*, *ApJ* **876** (2019) 32 [1811.06982].

[120] R. Scoccimarro, *Fast estimators for redshift-space clustering*, *Phys. Rev. D* **92** (2015) 083532 [1506.02729].

[121] E. Sefusatti, *Probing fundamental physics with large-scale structure: From galaxy formation to inflation*, Ph.D. thesis, New York University, New York, USA, Dec., 2005.

[122] M. Frigo and S.G. Johnson, *The design and implementation of FFTW3*, *Proceedings of the IEEE* **93** (2005) 216.

[123] G.J. Hill, K. Gebhardt, E. Komatsu, N. Drory, P.J. MacQueen, J. Adams et al., *The Hobby-Eberly Telescope Dark Energy Experiment (HETDEX): Description and Early Pilot Survey Results*, in *Panoramic Views of Galaxy Formation and Evolution*, T. Kodama, T. Yamada and K. Aoki, eds., vol. 399 of *Astronomical Society of the Pacific Conference Series*, p. 115, Oct., 2008 [0806.0183].

[124] D. Spergel, N. Gehrels, C. Baltay, D. Bennett, J. Breckinridge, M. Donahue et al., *Wide-Field InfrarRed Survey Telescope-Astrophysics Focused Telescope Assets WFIRST-AFTA 2015 Report*, *arXiv e-prints* (2015) [1503.03757].

[125] "*NIST Digital Library of Mathematical Functions*." http://dlmf.nist.gov/, Release 1.0.21 of 2018-12-15.

[126] D. Jeong, *Cosmology with high (z>1) redshift galaxy surveys*, Ph.D. thesis, University of Texas at Austin <EMAIL>djeong@astro.as.utexas.edu</EMAIL>, Aug, 2010.

Vita

Joseph Tomlinson

Education

- Ph.D., Astronomy & Astrophysics - Pennsylvania State University - 2024
- M.S., Astronomy & Astrophysics - Pennsylvania State University - 2020
- B.S., Physics - Drexel University - Summa Cum Laude - 2018

First Author Publications

- Tomlinson, J., Jeong, D., Kim, J. Efficient Parallel Algorithm for Estimating Higher-order Polyspectra. 2019 AJ **158** 116
- Tomlinson, J., Grasshorn Gebhardt, H., Jeong, D. Fast Calculation of Nonlinear Redshift-space Galaxy Power Spectrum. 2020 Phys. Rev. D, 93, 103528 (Editor's Suggestion)
- Tomlinson, J., Jeong, D. Spherical bispectrum: a novel visualization scheme for facilitating comparisons. 2023 JCAP 08, 040

Graduate Awards

- NASA FINESST, 2022
- NSF GRFP Honorable Mention, 2020
- University Graduate Fellowship, 2018